Rochester Institute of Technology
RIT Scholar Works

Theses | Thesis/Dissertation Collections

8-22-2007

Improvement of retrieved reflectance in the presence of clouds

Brent Bartlett

Follow this and additional works at: http://scholarworks.rit.edu/theses

Recommended Citation
Bartlett, Brent, "Improvement of retrieved reflectance in the presence of clouds" (2007). Thesis. Rochester Institute of Technology. Accessed from

This Dissertation is brought to you for free and open access by the Thesis/Dissertation Collections at RIT Scholar Works. It has been accepted for inclusion in Theses by an authorized administrator of RIT Scholar Works. For more information, please contact ritscholarworks@rit.edu.

Improvement of Retrieved Reflectance in the Presence of Clouds

by

Brent Bartlett

B.S. Physics, SUNY Geneseo, 2003
B.A. Computer Science, SUNY Geneseo, 2003

A dissertation submitted in partial fulfillment of the
requirements for the degree of Doctor of Philosophy
in the Chester F. Carlson Center for Imaging Science
Rochester Institute of Technology

August 22, 2007

Signature of the Author _____

Accepted by _____
Coordinator, Ph.D. Degree Program Date

CHESTER F. CARLSON CENTER FOR IMAGING SCIENCE

ROCHESTER INSTITUTE OF TECHNOLOGY

ROCHESTER, NEW YORK

CERTIFICATE OF APPROVAL

Ph.D. DEGREE DISSERTATION

The Ph.D. Degree Dissertation of Brent Bartlett
has been examined and approved by the
dissertation committee as satisfactory for the
dissertation required for the
Ph.D. degree in Imaging Science

_____
Dr. John Schott, dissertation Advisor

_____
Dr. Carl Salvaggio

_____
Dr. Tony Vodacek

_____
Dr. John Waud

_____
Date

DISSERTATION RELEASE PERMISSION

ROCHESTER INSTITUTE OF TECHNOLOGY

CHESTER F. CARLSON CENTER FOR IMAGING SCIENCE

Title of Dissertation:

Improvement of Retrieved Reflectance in the Presence of Clouds

I, Brent Bartlett, hereby grant permission to Wallace Memorial Library of R.I.T. to reproduce my thesis in whole or in part. Any reproduction will not be for commercial use or profit.

Signature _____

Date

Improvement of Retrieved Reflectance in the Presence of Clouds

by

Brent Bartlett

Submitted to the
Chester F. Carlson Center for Imaging Science
in partial fulfillment of the requirements
for the Doctor of Philosophy Degree
at the Rochester Institute of Technology

Abstract

Many algorithms exist to invert airborne imagery from units of either radiance or sensor specific digital counts to units of reflectance. These compensation algorithms remove unwanted atmospheric variability allowing objects on the ground to be analyzed. Low error levels in homogenous atmospheric conditions have been demonstrated. In many cases however, clouds are present in the atmosphere which introduce error into the inversion at unacceptable levels. For example, the relationship that is defined between sensor reaching radiance and ground reflectance in direct sunlight will not be the same as in a cloud shadow.

A novel method has been developed which utilizes ground based measurements to modify the empirical line method (ELM) approach on a per-pixel basis. A physics based model of the atmosphere is used to generate a spatial correction for the ELM. Creation of this model is accomplished by analyzing whole-sky imagery to produce a cloud mask which drives input parameters to the radiative transfer (RT) code MODTRAN. The RT code is run for several different azimuth and zenith orientations to create a three-dimensional representation of the hemisphere. The model is then used to achieve a per-pixel correction by adjusting the ELM slope spatially. This method is applied to real data acquired over the atmospheric radiation measurement (ARM) site in Lamount, OK. Performance of the method is evaluated with the Hyperspectral Digital Imagery Collection Experiment (HYDICE) instrument as well as a simulated multi-spectral system.

Contents

List of Figures

Acknowledgements

I would like to acknowledge my advisor Dr. Schott who was always willing to discuss and help me in this thesis work. My committee helped me through many different problems and road blocks. Rolando Raqueño was also crucial to the success of this research in providing countless hints and fixes for the use of the CONDOR computer management system. What acknowledgment section is complete without mentioning the support and encouragement of family and friends? Thanks to everyone!

Chapter 1

Introduction

Remote sensing offers an unique opportunity to use science to gain an understanding of the world that has only recently been possible. With the advent of multi and hyperspectral sensing systems, algorithms have been developed to utilize the information provided by many spectral bands. Due to the nature of electro-optical systems, data is usually collected in the form of a digital number (DN). Many of these algorithms rely on having the acquired imagery converted from DN into specific, material dependent units. This is important for several applications since DN is dependent on many sensor and atmospheric factors. While sensor specific factors tend to be relatively stable, atmospheric factors can change from day to day, or even from minute to minute. Many applications need to compare these airborne measurements to measurements made in the lab. The path length over which light travels in the lab has virtually no atmosphere between the object of interest and the sensor. The usefulness of the airborne image can therefore be increased if it is converted into units that do not depend on the atmosphere. One such unit that is widely used to alleviate these influences is called the surface reflectance factor ($r_{s\lambda}$)[Anderson et al., 2003]. Two methods for retrieving a reflectance from imagery will be discussed. The first consists of deriving a relationship between DN and reflectance. This is done by physically measuring the reflectance of the ground and pairing that measurement with the corresponding image pixel. This is generally referred to as the empirical line method (ELM). The next approach relies on the ability to model the atmosphere correctly and predict the observed radiance at the sensor. These models predict how energy is transfered through the atmosphere and are therefore called radiative transfer models (RT). It is important to note that the accurate retrieval of ($r_{s\lambda}$) in both cases is highly dependent on the quality of the input data. In the case of ELM, this takes the form of high quality reflectance measurements while RT codes require accurate atmospheric constituent measurements such as water

vapor and aerosol distributions. Achieving a high quality inversion has been demonstrated by using a combination of both RT and ELM models for instruments such as the Airborne Visible and Infra-Red Imaging Spectrometer (AVIRIS). However, it has been suggested that this technique can take as much as 1 to 2 person months per site to perform an accurately characterization [Clark et al., 2002]. Once a characterization is finished, environmental effects can change the site within just a few days. For sites that are routinely imaged, an automated system to perform measurements would clearly be benificial. Another issue facing these inversion algorithms is the dependence on atmospheric variability. For instance, the linear relationship derived for a calibration site within the scene may not be valid across an entire scene if cloud cover is present. This effect increases as imagery becomes larger spatially. Clearly there is a need for more extensive, automated ground truth. This is a driving factor behind the development of the Integrated Sensing Systems Initiative (ISSI) which this research is in part in support of. This research fits within the framework established by ISSI by exploring the improvement in retrieved reflectance factor that can be obtained by using auxiliary measurements.

In order for atmospheric correction to benefit from ground measurement the conditions in which reflectance retrieval exhibits large errors must be explored. In most atmospheric removal algorithms the assumption is made that the atmosphere is spatially homogenous. Since this assumption is violated when cloud cover exists in the scene, the benefits of using ground measurement in the presence of clouds will be explored. The ability of ELM to compensate for spatially changing illumination conditions is poor so a novel approach to inject information from ground measurements into the ELM process is shown. Since the new algorithm will essentially adjust the empirically derived relationship spatially throughout the scene it is termed Adaptive ELM (AELM). This process relies on acquiring the location of all significant cloud cover present in the scene. This information is used to create a three-dimensional radiometric model of the sky which allows for the prediction of the total radiance field. The model can then be used to generate the variability of the spatial illumination which is compensated for on a per-pixel basis. Model performance is also compared to direct ground measurement of the radiance field using a spectrometer to assess the relative performance of each approach. Finally, a method to use the spectrometer data to improve model output is explored.

The AELM algorithm is validated by using data collected over the atmospheric radiation measurement (ARM) site in Lamount, OK. The Hyperspectral Digital Imagery Collection Experiment (HYDICE) sensor was used to collect several different flight lines. The time difference between flight lines is used to generate a shift in cloud cloud configuration. This is essentially the same as moving spatially in the scene, but with

the added benefit of being able to group the validation tarps within a small spatial location. This data was taken in conjunction with several types of ground truth. The ground truth was used in the AELM algorithm to decrease the error present in the retrieved reflectance. The performance is validated using imagery from the hyper-spectral sensing system HYDICE. The spectral resolution is also degraded using the spectral response of WASP Lite which is a multi-spectral system. In both cases the algorithm shows improvement over a traditional ELM

Several different variables exist when generating the 3-dimensional model which are discussed. The sensitivity to cloud location in the hemisphere, the spatial resolution of the hemispherical sampling, and the locations of the sample centers are all issues that are addressed. While the validation is performed using a temporal lapse to generate variability in the radiance field, there are several issues to consider if the AELM is implemented over a wide spatial range. The application of a network of sky radiance measurements with differing spectral responses is discussed. As a final operational issue, the possibility of obtaining the necessary cloud location input for the AELM from space based sources is also considered.

Chapter 2

Background

2.1 Reflectance Factor Retrieval

In order to understand the mechanisms used to retrieve the reflectance factor from electro-optical (EO) sensors, it is first important to understand where the energy has come from. The region of the electromagnetic spectrum for this study will be limited to the VIS-NIR and SWIR as defined in Figure 2.1. The following mathematical treatment will use the conventions laid out in [Schott, 1997].

As long as the study is restricted to the 300 to 2500 nm portion of the spectrum, it can be assumed that thermally emitted photons are not added to the overall signal. With this in mind there are many paths that photons can take which end up at the sensor and which are shown in Figure 2.2. One can play the part of the accountant and add up each path's contribution to the overall signal observed. Since the goal of this research is to account for the variability present in many of the paths, a good understanding of each is needed.

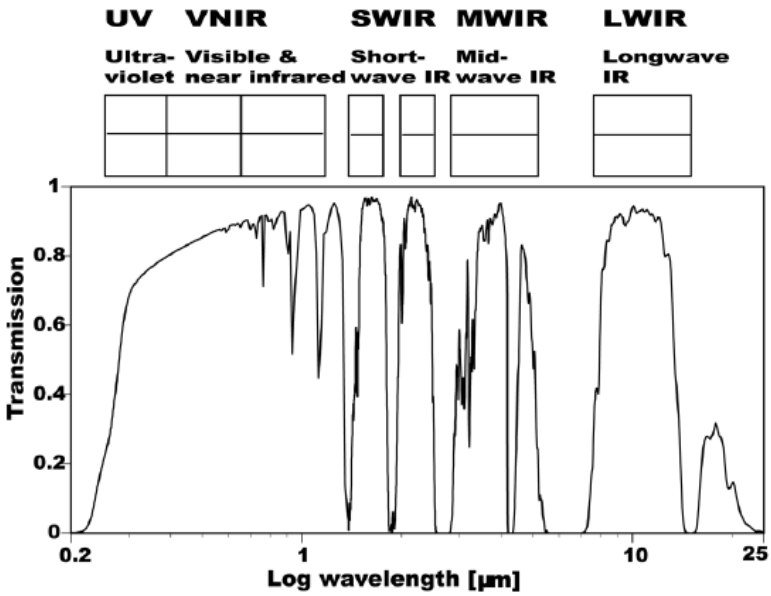

Figure 2.1: Atmospheric transmission spectra showing windows available for earth observations. [Schott, 1997]

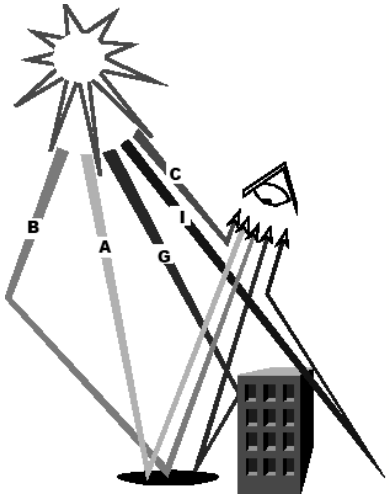

Figure 2.2: Diagram showing the various ways for solar energy to reach the sensor. [Schott, 1997]

Almost all energy in the reflective region originates from the sun. As this radiation travels through the vacuum of space, very little attenuation occurs. This energy is in units of irradiance $\left(\frac{W}{m^2 nm}\right)$, which will be denoted as $E'_s(\lambda)$ and is called the exoatmospheric irradiance. It can be assumed that this value is known quite accurately. As the radiation travels through the atmosphere, it will be changed in many ways. Some of the energy will avoid all scattering and will therefore be incident onto the surface of the earth. This energy will interact with the surface materials which will reflect some of the energy back up to the sensor, shown as path A in Figure 2.2. This is the energy that carries information about the surface and is of greatest interest for most remote sensing applications. Even if no scattering occurred in this path, the energy will still suffer two transmission losses. The first path is from the top of the atmosphere to the ground and the second path is from the ground to the sensor. These transmissions are dependent on the optical depth of the atmosphere as seen in equations 2.1 and 2.2.

$$\tau_1(\lambda) = e^{-\delta_1(\lambda)} \tag{2.1}$$

$$\tau_2(\lambda) = e^{-\delta_2(\lambda)} \tag{2.2}$$

where δ_1 and δ_2 represent the optical depth along both paths.

The energy from the sun which arrives at the ground after undergoing a transmission loss in Path A is shown in equation 2.3.

$$E_{direct\lambda} = E'_{s\lambda}\tau_1 cos\sigma \tag{2.3}$$

where $cos\sigma$ represents the solar zentih angle.

If scattering never occurred in the reflective region, then all energy recorded by a sensor would be due to path A. However, scattering does occur abundantly in the atmosphere and must be accounted for. Solar energy that is scattered towards the sensor can be grouped into two categories. The first is called L_d, or downwelled radiance and is defined as solar illumination that has undergone a scattering event before being reflected by the surface. This is illustrated by path B in Figure 2.2. It is possible to derive an analytical equation for the radiance incident on the surface as shown in equation 2.4.

$$L_{d\lambda}(\sigma, \phi) = E'_{s\lambda} \int \tau_{L1}(\lambda)\tau_{L2}(\lambda)\beta_{sca}(\lambda, \theta_v)dr \tag{2.4}$$

The use of this equation will now require the definition of several geometric parameters to describe the sun / sensor relationship. Figure 2.3(a) labels the coordinate axes as well as the angles that relate sensor to sun. Figure 2.3(b) shows the terms in

the above equation graphically where $E'_{s\lambda}$ is the exoatmospheric irradiance, τ_{L1} and τ_{L2} are the transmissions along the incident path (L_1) and the path to the target (L_2), $\beta_{sca}(\lambda, \theta_v)$ is the spectrally dependent angular scattering coefficient, and θ_v is the angle between L_1 and L_2. The total downwelling irradiance can now be found by integrating over all the azimuth and zenith angles as shown in equation 2.5. This quantity can be measured directly with instrumentation which will be discussed later.

$$E_{d\lambda} = \int_{\phi=0}^{2\pi} \int_{\sigma=0}^{\frac{\pi}{2}} L_{d\lambda}(\sigma, \phi) cos\sigma sin\sigma d\sigma d\phi \tag{2.5}$$

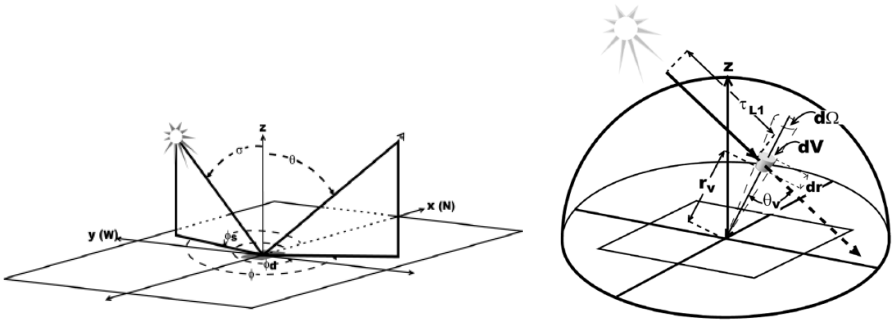

(a) World Coordinate System. (b) Terms in Equation 2.4

Figure 2.3: Coordinate system in use for radiometric terms.[Schott, 1997]

At this point it is necessary to change the direction of the incident radiation by including the effect of the surface reflectance. This can be done by simply multiplying equations 2.3 and 2.4 by the surface reflectance factor. The correct measurement for this factor will depend on several components, including the sun/sensor orientation which will be discussed in the Field Measurement section.

The second category of scattered sensor reaching solar energy is called upwelled radiance. This follows path C of Figure 2.2. This radiation is directed by scattering towards the sensor before it is able to interact with the surface and therefore carries no information about the target. This is very similar to downwelled radiance in formulation and is described in equation 2.6 and Figure 2.4.

$$L_{u\lambda}(\theta, \phi) = E'_{s\lambda} \int \tau_{L1}(\lambda) \tau_{L2}(\lambda) \beta_{sca}(\lambda, \theta_v) dr \tag{2.6}$$

The above pathways can be combined into a single formulation which will describe the total radiance that will reach the sensor. This equation is simply a combination of

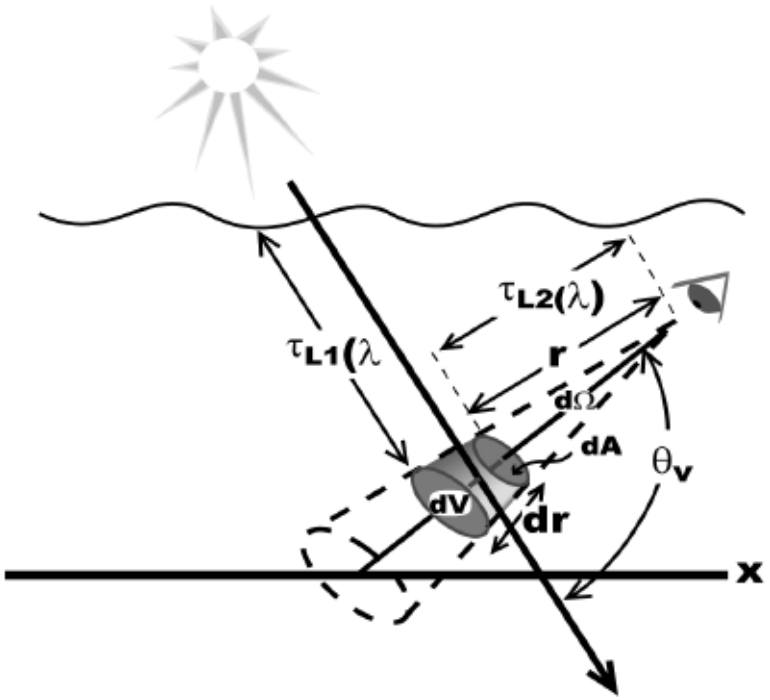

Figure 2.4: Geometry for describing upwelling radiance.[Schott, 1997]

equations 2.3, 2.5, and 2.6 which accounts for the ground reflectance and is referred to as a governing equation and is shown below:

$$\begin{aligned} L_{s\lambda} &= \left[E'_{s\lambda} cos\sigma \frac{\tau_{1\lambda} r(\lambda)}{\pi} + E_{d\lambda} \frac{r_d(\lambda)}{\pi}\right] \tau_{2\lambda} + L_{u\lambda} \\ &= \left[L_{sun\lambda} \tau_{1\lambda} r(\lambda) + L_{d\lambda} r_d(\lambda)\right] \tau_{2\lambda} + L_{u\lambda} \end{aligned} \tag{2.7}$$

where $r_d(\lambda)$ is the diffuse surface reflectance factor.

This formulation is important because it will allow for a useful linear relationship to be derived between the reflectance factor and the observed sensor reaching radiance which will be discussed in the next section. While this governing equation is usefull, it is important to realize that several other factors affect the solar radiation as well. For example, Figure 2.2 shows paths G and I which include background influences. While these effects can modify the observed signal, it will be shown that the above form of the governing equation can produce quite accurate results under the correct conditions.

2.1.1 Empirical Line Method

Now that the various pathways describing radiation propagation have been enumerated, a method to retrieve the reflectance from equation 2.7 can be devised. This section will explore how and when ELM works, as well as when its assumptions fail. ELM takes the governing equation for the sensor reaching radiance and simplifies it by assuming that the reflectance of the target in both the direct and diffuse paths are the same. Equation 2.8 shows this relationship for two image pixels, note that the wavelength dependence has been dropped for notational convenience.

$$\begin{aligned} L_1 &= \left(\frac{E_s' cos\theta \tau_1}{\pi} + L_d\right) \tau_2 r_1 + L_u \\ L_2 &= \left(\frac{E_s' cos\theta \tau_1}{\pi} + L_d\right) \tau_2 r_2 + L_u \end{aligned} \tag{2.8}$$

The above relationship can be expressed in simple linear terms, and the slope and intercept may be expressed as a function of the radiance and reflectance for two known pixels.

Let $m = \left(\frac{E_s' cos\theta \tau_1}{\pi} + L_d\right) \tau_2$ and $b = L_u$
For two pixels with known reflectance:

$$\begin{aligned} &\text{Pixel 1: } L_1 = mr_1 + b \rightarrow b = L_1 - mr_1 \\ &\text{Pixel 2: } L_2 = mr_2 + b \rightarrow L_2 = mr_2 + L_1 - mr_1 \\ &\qquad\qquad L_2 - L_1 = m(r_2 - r_1) \\ &\qquad\qquad m = \frac{L_2 - L_1}{r_2 - r_1} \end{aligned}$$

Once values for m and b are determined, a reflectance value for each pixel in the image can be found using equation 2.9.

$$r_\lambda = \frac{L_{pixel} - b}{m} \tag{2.9}$$

Since reflectance can be linearly related to sensor reaching radiance the recorded digital number can also be related as such. This can be seen in equation 2.10, where m now contains a factor which will convert radiance to digital number (DN) and b is now a sensor bias.

$$DN_\lambda = mr_\lambda + b \tag{2.10}$$

By taking multiple ground measurements of reflectance the linear function that will serve as a look up table (LUT) can be found with greater confidence than if just two points are used. An example of a LUT is shown in Figure 2.5 which was produced by the RT code MODTRAN 4. While this procedure seems straight forward, there are many subtle effects that must be considered to obtain a quality inversion to reflectance. The first effect to account for is the non-zero intercept in Figure 2.5. This is due to path C radiance, or upwelled radiance, and must be accounted for. This means that estimating a zero percent reflector as having zero radiance is not usually a good assumption, thus requiring the measurement of a low reflectance pixel. The retrieved reflectance also tends to be of lower accuracy in the 'blue' end of the spectrum (around 400nm). This is due to increased scattering which can be compensated for by using more than two points. This effect will be discussed in detail later.

The upwelling path certainly plays an important role in adjustment of imagery taken with spaceborne sensors. While the magnitude of the upwelling radiance is smaller for lower altitude collections it is still important even for sensors flying at 1000m. For example, if just a high value of reflectance is used and the atmospheric radiance is guessed incorrectly, errors as high as 15-20%, or 4 reflectance units for a 20% reflector, can be produced.

A major goal of this research is to improve the error in reflectance retrieval that is currently being reported in the literature. The error reported for using two points tends to produce a better estimate of the atmospheric radiance and performs generally within 11%, or 2.2 reflectance units[SMITH and MILTON, 1999]. This error has been driven down to the 1 reflectance unit error level if 3 or 4 reflectance values are used to derive the prediction equation [Price et al., 1995]. These error levels have been obtained with several assumptions about both the materials on the ground and the atmosphere. First the spatial extent of the calibration targets must be much larger than a pixel size for a

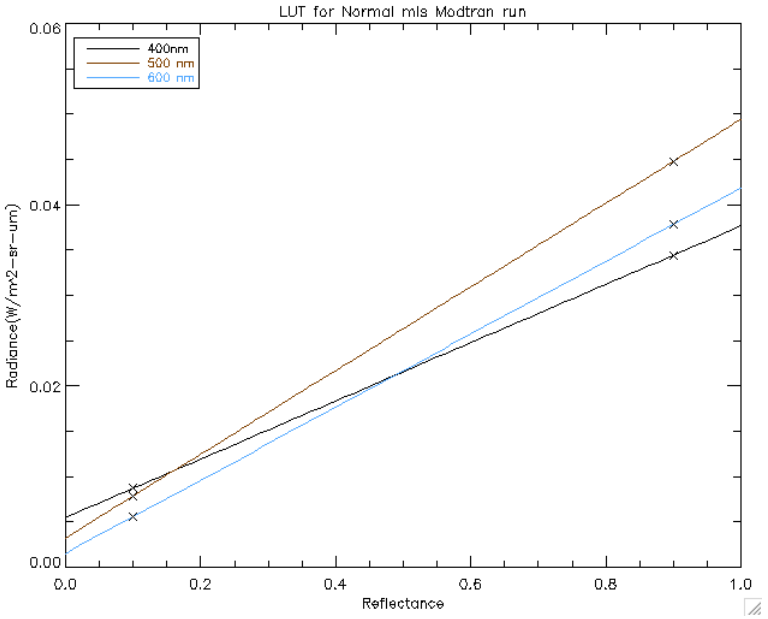

Figure 2.5: Linear relationship for 3 bands, based on the two points marked with X.

given sensor. This requirement is important to minimize the effects of the surroundings on the calibration site. This will also allow for the averaging of several pixels to decrease the noise present. Next, the targets should be Lambertion if the ground reflectance measurement is not made with the same geometry as the aircraft image. A more in depth discussion of reflectance effects will be dealt with in section 2.2.2.

While the main purpose of this research is concerned with improving airborne retrievals, space borne inversion is also important to consider. Due to the nature of satellite orbital paths, similar spatial regions are imaged on a regular basis as shown in Figure 2.6.

Setting up automated ground truth is therefore attractive under a satellite and the literature shows successful use of ELM with satellite systems. For example, a modified ELM has been developed for use with the Landsat-5 TM and Landsat-7 ETM+ satellite systems that require the use of only one measured reflectance panel, and relaxes the requirements on the target's Lambertion properties [Moran et al., 2001]. This is important for a system like Landsat since the ground instantaneous field of view (GIFOV) is 30m [Schott, 1997], which makes it difficult to obtain large enough target sites. Other satellites system have been developed that have a GIFOV on the order of 1 to 5m, such as IKONOS and QUICKBIRD. ELM approaches to reflectance retrieval that have been applied to such systems report error's of ± 3 reflectance units [Karpouzli and Malthus,

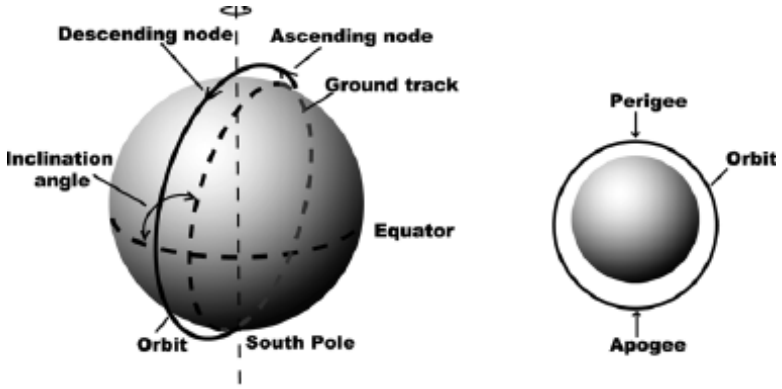

Figure 2.6: Example of low earth orbit, similar to the orbit used by lansat.[Schott, 1997]

2003].

If suitable calibration targets can be found, the assumption that is routinely violated is the homogeneous sky assumption. The above error levels have all been reported on days which are very clear with no clouds, thus producing a very homogenous atmosphere. These days rarely exist, especially in the climate where this research takes place.This research will therefore focus on reflectance retrieval in the presence of clouds, where the illumination will vary greatly throughout a scene. Producing similar error metrics to those sited above with a cloudy atmosphere will clearly advance the current state of the art.

2.1.2 Radiative Transfer

While using an empirically derived relationship between radiance and reflectance has its advantages, another approach can be taken. If the physics of the media that the radiance interacts with can be modeled then the different effects present can be characterized. This is the approach taken by radiative transfer models which can be used to derive the surface reflectance factor. In general the different paths discussed in section 2.1 are combined to generate a governing equation. This equation is modified to include constants which depend on atmospheric conditions. While many variations are present in the literature, an example equation used in the Fast Line-of-Sight Atmospheric Analysis of Spectral Hypercubes (FLAASH) is shown in equation 2.11.

$$L_{sensor} = \frac{A\rho + B\rho_a}{1 - \rho_a S} + L_b \tag{2.11}$$

where: ρ is the surface reflectance, ρ_a is surface reflectance averaged over the pixel and a surrounding region, S is the spherical albedo of the atmosphere, L_b is the radiance backscattered by the atmosphere, and A and B are coefficients that depend on atmospheric and geometric conditions but not on the surface [Matthew et al., 2002]. All terms in the above equation are spectrally dependent and must be determined separately for each spectral channel.

Three examples of RT codes that have been and are being developed include the Canadian Advanced Modified 5S (CAM5S)[O'Neill et al., 1996], the Second Simulation of the Satellite Signal in the Solar Spectrum (6S) [Vermote, 1997], and the Moderate Atmospheric Radiance and Transmittance model (MODTRAN4)[Berk et al., 1998a]. These radiative transfer (RT) codes are used in many atmospheric correction routines. These routines each use the RT codes with various approaches to perform the inversion process. Many exist such as the Atmospheric Removal Program (ATREM)[Gao et al., 1993] which used 6S, the High Accuracy Atmospheric Correction for Hyperspectral Data (HATCH) [Qu et al., 2003] which is an updated version of ATREM, Atmospheric Correction Now (ACORN)[Imaging and version 3.12, 2001] which uses MODTRAN4, and FLAASH. While the radiative transfer codes differ in which approximations are used, it is helpful to be able to visualize which paths are accounted for. Figure 2.7 shows the paths of radiance that are calculated in the radiative transfer code MODTRAN.

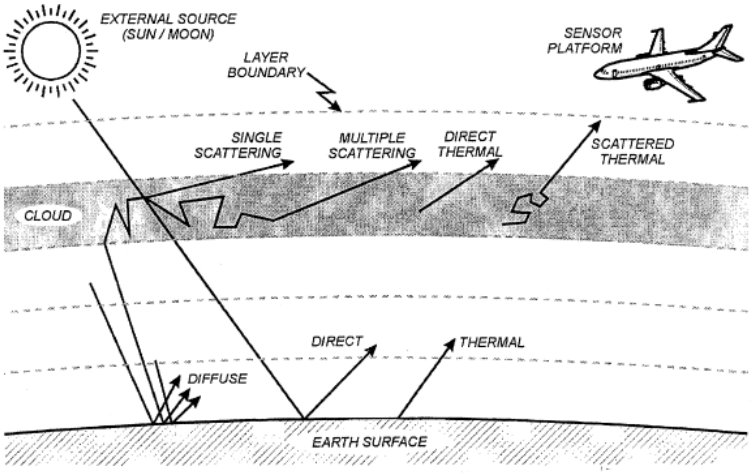

Figure 2.7: Diagram showing the various pathways accounted for by MODTRAN. [Berk et al., 1998b].

While there are various assumptions made for each of the correction algorithms, the quality of the output can only be as good as the inputs for the model. The best

performance for such models occurs when atmospheric parameters such as water vapor profiles and aerosol distribution are known. These quantities can be measured, but are often estimated from the hyperspectral data products themselves.

As was done in the review of the ELM method, it is important to get a handle on how well these correction routines can perform. This will set a goal in terms of error limits for this research to achieve. The two radiative transfer codes CAM5S and MODTRAN 4 were used to perform atmospheric correction as well as the inversion code ATREM. The inversion process used in-scene derived atmospheric parameters and achieved an overall performance of 4.2% using CAM5S, 3.6% for ATREM , and 2.3% using MODTRAN4 [Staenz et al., 2002]. This percentage is based on a 45% reflector, which puts the best case performance using MODTRAN 4 at the 1 reflectance unit error level in bands free of strong absorption lines. It should be noted that the performance is based on a comparison made with ground measurements. This was performed with a GER3700 spectrometer which operates at the 3.6% error level. FLAASH and HATCH have made improvements to assumptions made by older algorithms such as ATREM such as improved aerosol and water vapor retrieval. Preliminary results show that they both perform at approximately the 5% level of error [Kruse, 2004].

The next question to be addressed is the level of error that can be expected when cloud cover is present. Atmospheric correction routines that make use of radiative transfer codes currently do not account for cloud cover effects. The errors reported above all depend on having an atmosphere that does not violate assumptions like plane parallel layers as seen previously in Figure 2.7. This occurs once again on clear days where atmospheric variability is at a minimum. While some RT codes do have a limited cloud cover capacity, such as MODTRAN 4, they have issues with producing cloud radiance in conditions that are not complete over-cast. This will be discussed in further detail in the approach section. Since the methods do not account for cloud effects, it can be assumed that they will produce much greater error than reported for clear days when even partial cloudy conditions appear.

Since a goal of the ISSI initiative is to produce near-real time results, the runtime for these algorithms must be assessed. The best performance was reported using MODTRAN 4 LUT based-approach, which took 183 minutes on a Sun ULTRASPARC 1 workstation[Staenz et al., 2002]. The FLAASH and HATCH algorithms both ran in approximately 15 minutes [Kruse, 2004] but performed at a lower level of accuracy. In ordered to perform inversions in a closer to real time environment with an accuracy of around 1 reflectance unit, a more empirical approach will be considered.

2.1.3 Comparison and Combination

Yet another approach used to obtain the reflectance factor is a combination of model and empirical based methods. Many of the errors that are present in radiative transfer based retrieval algorithms such as ATREM occur from assumptions made within the model. Errors in the definition of solar irradiance, source illumination, and magnitudes of atmospheric constituents (such as water vapor) lead to residual errors in the retrieved reflectance. This can be accounted for by comparing the model output to ground-based measurements and deriving multiplicative correction factors on a per-wavelength basis[Clark et al., 2002]. This method has also performed well in a modeling environment using synthetic data [Ben-Dor et al., 2004]. While combining methods will produce very high quality retrievals, it should be noted that this combination will still not account for cloud influences. Figure 2.8 illustrates the steps to this approach.

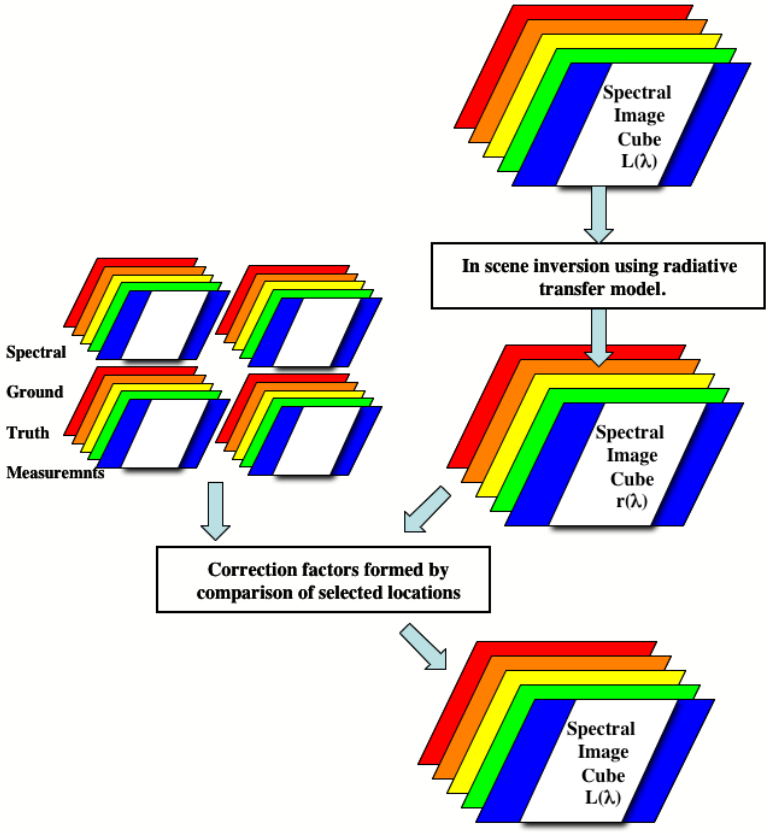

Figure 2.8: Diagram of the steps used to combine both types of inversion processes.

It is also interesting to compare the results of inversion using a model based approach as compared to an empirical based approach. One way to judge the utility of the data produced using different inversion techniques is to assess the performance of particular algorithms when using the data. One such application is spectral linear unmixing. Linear unmixing relies on the assumption that the reflectance of a pixel that contains several different materials can be produced by combining the spectra of each individual material in a linear fashion. In most cases the spectra combined to produce a mixed pixel comes from laboratory reflectance measurements. In a comparison between empirical and model based inversion techniques, the empirical line method produced reflectance values that worked best with the unmixing algorithm. While the overall quality of both inversion techniques was similar, ELM tended to enhance spectral features, thus allowing for better distinction between endmember mineral classes [Dwyer et al., 1995]. This example illustrates how it is important to consider the application that the reflectance data will support when choosing an inversion technique.

Another important consideration when comparing empirical vs. model based reflectance retrieval is the sensitivity to random noise (sensor). Most hyperspectral sensors have issues producing data with high signal to noise ratio's and thus exhibit high random noise. This noise effect will be more of an issue in model based inversions that rely on extracting atmospheric parameters from the imagery. This sensitivity can lead to errors that are twice as high in model retrieval than that of empirical [Kerekes, 1998].

When using a model based approach, it is necessary to convert the sensor digital number values to units of radiance since radiance is what the models predict. This requires a sensor that has undergone a rigorous radiometric calibration. While many of todays sensors do have some level of absolute calibration, even the best calibration will have some residual error associated with it. For this reason, it can be an advantage to use an empirical based approach, simply since it does not require such a calibration.

The substance in the above comparison is that for noisy, cloudy data the empirical approach should provide the best results for reflectance factor retrieval. The empirical approach is not only computationally fast, ideal for rapidly changing illumination conditions, but more robust in the presence of noise. With this said, it will be seen later on that there will still be a role for radiative transfer codes to play when attempting the inversion problem in partial cloud cover.

2.2 Field Measurement

While remote sensing shows its true utility when products can be produced directly from air or spaced based platforms, the accuracy of such outputs can be improved with additional information gathered from ground level. This is where the class of measurements sometimes referred to as 'ground truth' is used. The idea being that measurements on the ground will provide the possibility to achieve a higher accuracy when determining either radiance or reflectance. They can also be used to directly determine parameters with greater accuracy than primary imaging platforms such as atmospheric parameters. In the following sections, different methods that have been used to produce information to enhance remotely sensed data will be explored.

2.2.1 Measurement of Irradiance or Radiance

Radiometric measurement from the ground can aid in determining the magnitude of certain paths from Figure 2.2. For instance, a spectrometer can be fitted with a flat diffuse receptor as shown in Figure 2.9, called a cosine receptor. If the direct component (path A) is blocked, then the signal produced is proportional to the downwelling irradiance (path B) plus any background irradiance.

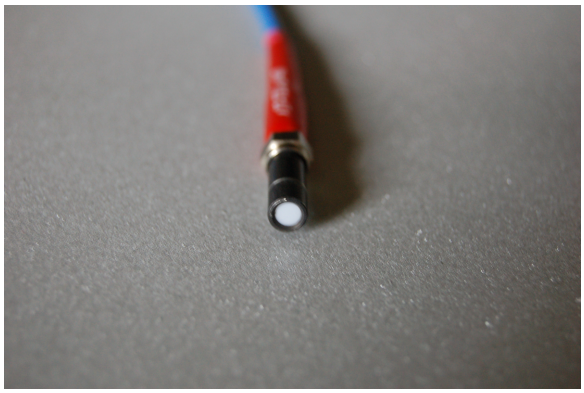

Figure 2.9: Cosine fiber adapter which measures diffuse irradiance.

The field of view can be limited using the aperture shown in Figure 2.10 which will change the measured signal to be proportional to radiance. This particular radiometer allows for different size entrance apertures to be used. A smaller hole will give a smaller FOV which will allow for path A to be measured directly. A FOV of about 3° will give the radiometer a FOV which just encompasses the energy coming from the

sun. It should be noted that just the first half of the path is measured by the instruments since the transmission from the ground to the sensor is not accounted for (τ_2).

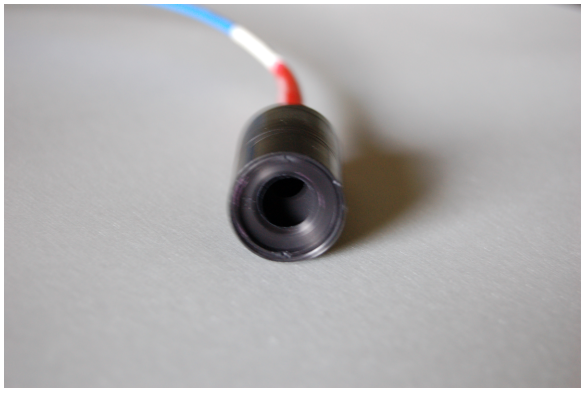

Figure 2.10: Directional fiber adapter with 15° FOV.

The information obtained from spectrometers is initially in the same form as the values obtained from an airborne E/O system. This is in the form of digital number which is in itself not very useful. Since measurements on the ground are most useful when compared to those made in the atmosphere, they must be converted into absolute units of radiance. This process is called radiometric calibration, while the process of assigning each pixel a wavelength value is called spectral calibration. It is important to understand how spectrometers are calibrated in ordered to assess the error associated with measurements made by them.

In order to spectrally calibrate a spectrometer, each pixel in its detector array must be associated with a wavelength. While it is possible to predict how the diffraction grating will disperse the incoming light, imperfections in both the fabrication as well as the installation of the grating can lead to errors in the spatial location of each spectral wavelength. In order to calibrate each pixel to a wavelength value, a lamp filled with a gas can be used. For example if an Argon lamp is used, it will produce emission lines at very specific and known wavelengths. The spectral value for each observed emission line is obtained from a source such as the CRC Handbook of Chemistry and Physics. After the corresponding pixel value for each line is found for each spectral value, a relationship between pixel value and spectral value can be found. Both 2nd and 3rd order polynomial relationships can be found, both of which yield slightly different results. An example of how spectral calibration can lead to error is shown below. An ocean optics SD2000 spectrometer was aimed at an Argon lamp with known emission spectra. Figure 2.11 shows how the spectral calibration can produce slightly different results depending on the mathematical relationship used.

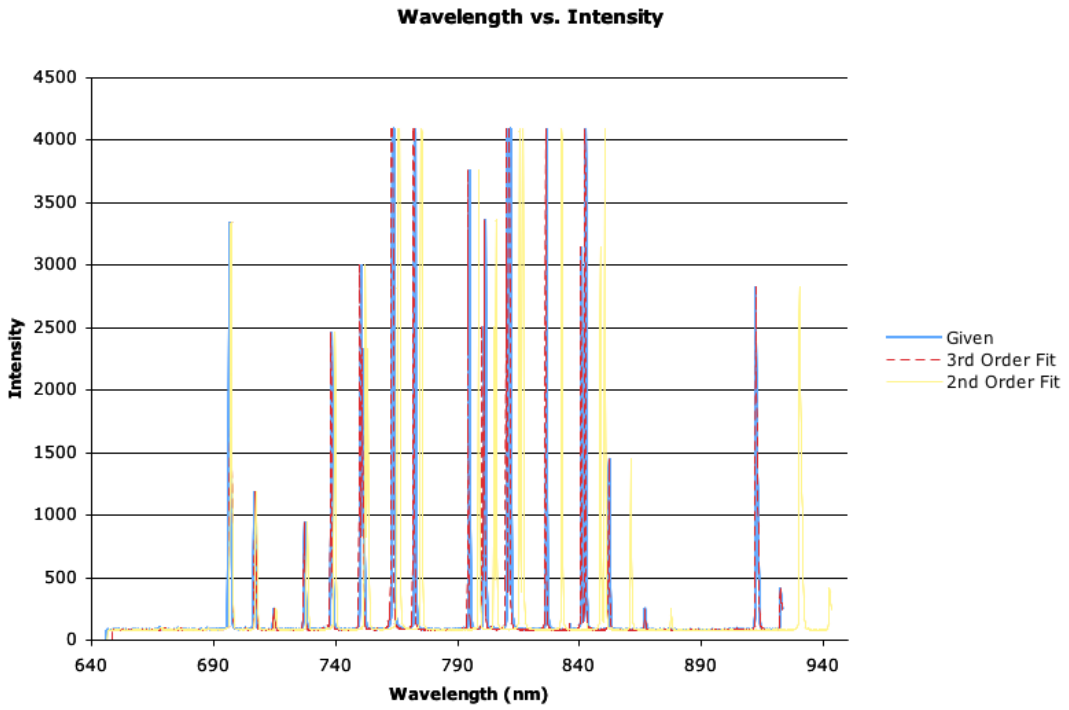

Figure 2.11: Plot showing the calibration performed using 2nd and 3rd order fits compared to the factory given calibration with ocean optics spectrometer.

Spectrometers give valuable spectral information about many materials. While the location of the spectral features is important to know, sometimes it is also necessary to know the magnitude of the observed spectra in an absolute sense. This usually takes the form of either spectral radiance $\left(\frac{W}{cm^2 srnm}\right)$, or spectral irradiance $\left(\frac{W}{m^2 nm}\right)$ depending on the input to the system. This calibration is performed by obtaining a source that has both a continuous spectrum as well as a known energy output for each wavelength. The National Institute for Standards and Technology (NIST) performs calibrations of several different types of sources for this purpose. As explained earlier, if the input to the system is a cosine receptor, the instrument will measure irradiance. The source used to calibrate this spectrometer is therefore a simple light bulb that has been characterized by NIST. The light bulb is attached to a known resistance, and a stable power supply. The voltage is monitored and set at a value such that the current flowing through the light bulb is as close to what NIST reports as possible. Once the system has had time to stabilize, one can use a table of values for irradiance at a set distance to predict the irradiance incident onto the cosine receptor. If the input to the system is a directional

attachment, the system will perform a measure of radiance, and therefore a different calibration source is used. In this case, a NIST traceable integrating sphere is used to produce a known radiance. The sphere is adjusted to a precise voltage in the same way that the light bulb is, and the directional attachment is positioned towards the sphere with the use of a laser pointer.

The reason for doing this is so the observed radiation can now be known. The values produced by the spectrometer can now be adjusted with simple coefficients to match the known values. Before this can be done, the integration time used must be accounted for. For example, if the calibration source was observed with an integration time of 10 ms and again with 50ms, the coefficients calculated would be different for each integration time. It is important to adjust the source radiation to a level which will give high signal levels without saturation occurring. This will ensure for the best signal to noise ratio. The coefficient can now be calculated using equation 2.12.

$$\alpha_{intTime}(\lambda) = \frac{L_{cal}(\lambda)}{DC(\lambda)} \left(\frac{radiance}{counts} \right) \tag{2.12}$$

where it is assumed that the digital count (DC) of each pixel on the array is already calibrated to a wavelength value. Now when subsequent measurements are made at an integration time, the corresponding α can be chosen and applied to the data to produce radiance via equation 2.13.

$$L_{cal}(\lambda) = DC_{obs}(\lambda) \cdot \alpha(\lambda) \left(\frac{W}{cm^2 srnm} \right) \tag{2.13}$$

The selection of integration time is important to the accuracy of the radiance produced by equation 2.13. The integration time should be selected the same way as during calibration such that the maximum DC is obtained without saturation. As mentioned before, this increases the signal to noise ratio (SNR), but it also decreases error due to detector non-linearity. This non-linearity is due to the fact that the pixel responds slowly at first to incident light, increases quickly in mid-range, and slows down again when saturation is approached. As long as the observed DC is in the same signal range as was present during calibration, linearity should not be an issue. If the DC observed is significantly different in magnitude to that present in calibration, then another approach outlined in [HOB, 2002] can be used.

It is important to note that the spectral response of the sensor was not accounted for. This will lead to an insignificant error if the bandpass is small enough so that the response function will effectively approach a square response. If the sensor has a gaussian response over the bandpass of the sensor, then the response can be used to adjust the known radiance before the coefficients are calculated. Another effect to

consider is that of an integration time offset to account for errors in the integration time. For example, if the spectrometer is set to integrate for 20ms it might actually integrate for 21ms. This error in the ocean optics spectrometer used above is in the range from -1 to 11 ms and is spectrometer specific. Having a spectrometer that is radiometrically calibrated is important for measuring quantities such as downwelling irradiance. While it is important to perform calibrations correctly, some measurements do not need to be radiometrically calibrated. One such measurement is reflectance, which will be discussed in section 2.2.2.

2.2.2 Ground Reflectance

The measurement of reflectance in a field setting is fairly straight forward from a theoretical standpoint. The basic idea being to measure the energy incident onto the surface in question compared to the energy exiting the surface. The following review can be found also in [Smith, 2004]. Equation 2.14 shows how the reflectance factor (ρ) can be found.

$$\rho(\lambda) = \frac{L_{reflected}(\lambda)}{L_{incident}(\lambda)} \tag{2.14}$$

As discussed in section 2.1, there are many components to the radiance reaching the sensor. The governing equation for sensor reaching radiance, equation 2.7, can be modified to account for background effects. This modification will use all the paths in Figure 2.2 and is shown below in equation 2.15.

$$\begin{aligned} L_s(\lambda) &= \left[L_{direct}(\lambda)\rho(\lambda) + L_d(\lambda)\rho(\lambda) + L_{BG}(\lambda)\rho(\lambda) + L_{albedo}(\lambda)\right]\tau_2(\lambda) + L_u(\lambda) \\ &= L_{pathA} + L_{pathB} + L_{pathG} + L_{pathI} + L_{pathC} \end{aligned} \tag{2.15}$$

where path A is the radiance reflected off the target directly from the sun, path B is the downwelled radiance reflected off the target, path G is the background radiance reflected off the target, path I is the background radiance that reaches the sensor without interacting with the target, and path C is the upwelling radiance. Since we are dealing with a sensor at ground level, it is usually reasonable to assume that the path from the target to the sensor is short enough such that path I and path C are negligible. Since the path is short, it is also true that τ_2 is very close to unity. Using these assumptions, equation 2.15 reduces to equation 2.16.

$$L_s(\lambda) = [L_{direct}(\lambda) + L_d(\lambda) + L_{BG}(\lambda)]\rho(\lambda) \tag{2.16}$$

One way to determine the reflectance using equation 2.16 would be to measure the direct, downwelled, and background radiance separately along with the sensor radiance. This is not very practical so usually two measurements are made to calculate the reflectance. One measurement is of the ground in question, while the other is of a highly reflective material just above the ground (like spectralon). In this way a ratio of the measurements can be formed which will yield the sample reflectance. Equation 2.17 shows a way to express the measured radiance in terms of sensor digital count.

$$DC_s(\lambda) = (m)(c)\rho(\lambda) \tag{2.17}$$

where $m = [L_{direct}(\lambda) + L_d(\lambda) + L_{BG}(\lambda)]$ and c is a sensor calibration constant.

Equation 2.18 shows how the ratio of the two measurements will cause a cancellation of the incident radiation and yield the reflectance factor of the ground. This will happen assuming that the m terms are equal, which is true with an atmosphere that does not vary during the time that the two measurement take place. It is also important that both measurements have the same sensor response and zero bias. Figure 2.12 shows how the three sources of energy in equation 2.16 interact with the environment.

$$\rho(\lambda)_{sample} = \frac{DC(\lambda)_{sample}}{DC(\lambda)_{reference}}\rho(\lambda)_{reference} \tag{2.18}$$

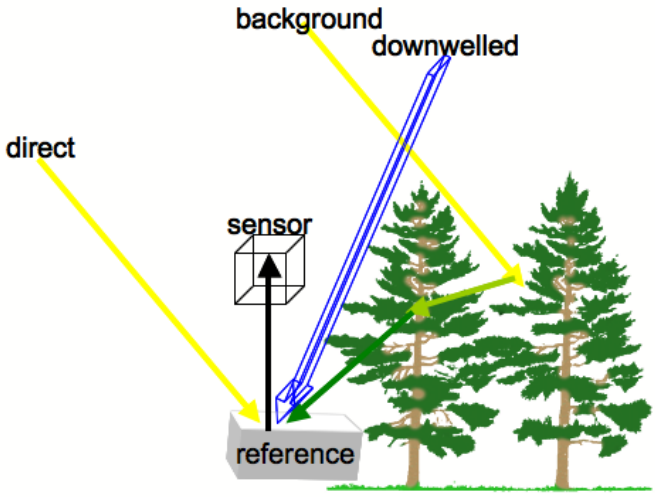

(a) Measurement of reference panel.

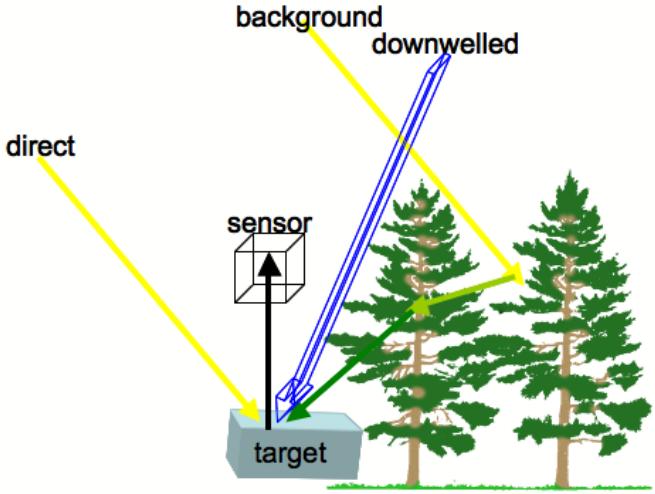

(b) Measurement of target.

Figure 2.12: Measurement of target reflectance by first measuring the radiation field off of a reference panel with known reflectance (assumed here to be one). The measurement of the target can then be divided by the reference measurement to obtain the target reflectance.

A cosine receptor can also be used to capture the incident radiation which drops the requirement of using a reference standard during reflectance measurement. However, the two spectrometers must be calibrated to each other, which does require a reference. The spectrometer with an aperture, or spectrometer A, is directed towards the reference while the spectrometer with a cosine receptor, or spectrometer B, records the hemispherical irradiance. For a Lambertion target, radiance leaving an object can be related to irradiance incident onto the object by equation 2.19.

$$L(\lambda)_{exitant} = \frac{E(\lambda)_{incident}\rho(\lambda)}{\pi} \tag{2.19}$$

Measurement B can then be divided by measurement A which will produce a correction factor. This correction factor, $C_r(\lambda)$, will be used to cross-calibrate the spectrometers. The development of this correction factor is shown, with the use of equation 2.19, in equation 2.20.

$$\begin{aligned} C_r(\lambda) &= \frac{Measurement_B}{Measurement_A} \\ &= \frac{E(\lambda)_s b(\lambda)_B}{L(\lambda)_r b(\lambda)_A} \\ &= \frac{E(\lambda)_s b(\lambda)_{ratio}}{L(\lambda)_r} \\ &= \frac{E(\lambda)_s b(\lambda)_{ratio}\pi}{E(\lambda)_s \rho(\lambda)_r} \\ &= \frac{b(\lambda)_{ratio}\pi}{\rho(\lambda)_r} \end{aligned} \tag{2.20}$$

where:

Variable	Description
$E(\lambda)_s$	Spectral Irradiance from Sky
$L(\lambda)_r$	Spectral Radiance from Reference
$b(\lambda)_A$	Spectrometer Response Bias for Spectrometer A
$b(\lambda)_B$	Spectrometer Response Bias for Spectrometer B
$b(\lambda)_{ratio}$	$b(\lambda)_B$ divided by $b(\lambda)_A$
$\rho(\lambda)_r$	Reflectance Factor for Reference

The reflectance factor can be defined as the irradiance leaving an object divided by the irradiance incident onto the object from the sun and sky. Equation 2.21 shows how

this definition can be modified to use the measurements from the two spectrometers to produce the reflectance factor. The assumption here is that the irradiance recorded by the cosine detector is the same as the irradiance falling onto the sample.

$$\begin{aligned}
\rho(\lambda)_{sample} &= \frac{E(\lambda)_{sample}}{E(\lambda)_s} \\
&= \frac{E(\lambda)_{sample}}{E(\lambda)_s} \cdot \frac{b(\lambda)_{ratio}\pi}{b(\lambda)_{ratio}\pi} \cdot \frac{\rho(\lambda)_r}{\rho(\lambda)_r} \\
&= \frac{L(\lambda)_{sample} b(\lambda)_A}{E(\lambda)_s b(\lambda)_B} \cdot C_r(\lambda) \cdot \rho(\lambda)_r \\
&= \frac{Measurement_{[A,sample]}}{Measurement_B} \cdot C_r(\lambda) \cdot \rho(\lambda)_r
\end{aligned} \tag{2.21}$$

Figure 2.13 shows the up-looking and down-looking radiometers. If the geometry of both radiometers is considered, it is clear that the assumption fails. However, studies indicate [Duggin and Cunia, 1983] that under clear conditions the efficiency ratio of the variance for the sequential to the simultaneous method yields values very close to 1.0. This means that the two methods will produce similar results in clear conditions. However, if cloud presence is considered, the ratio becomes high due to the fact that the sequential method adds more variance to the measurement. While both methods can produce excellent reflectance spectra, each approach has its own considerations and peculiarities.

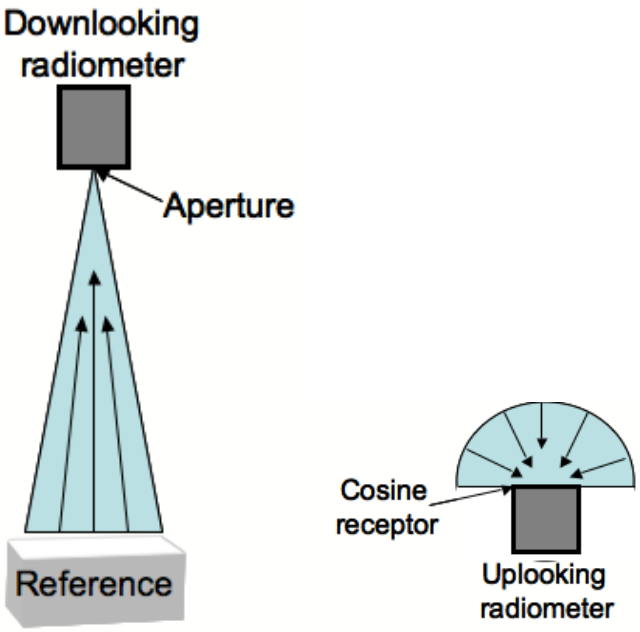

(a) Measurement of reflected illumination using downlooking radiometer with apeture.

(b) Measurement of illumination using uplooking radiometer with cosine adapter.

Figure 2.13: Two spectrometers which can be used to measure the incident illumination field as well as the reflected illumination simultaneously.

Another way to obtain a ratio-type measurement of reflectance which requires one spectrometer and no reference sample is to use an integrating sphere. The opening of the sphere in one case is faced up and covered with a cosine receptor to measure irradiance. The opening can also be faced down and covered with an aperture to measure sample radiance. While only one spectrometer is used, one still needs to calibrate the two measurements. This is because the overall system is changed between the two measurements. For example, different portions of the integration sphere will be illuminated during the two measurements. A calibration factor to account for this change can be generated using equation 2.20, where measurement B is shown in Figure 2.14(a) and measurement A is shown in Figure 2.14(b). The reflectance factor is found by revisiting equation 2.21.

The approach is easily automated with the use of step motors. The time between measurements is only limited by the amount of time it takes to spin the sphere from up-looking to down-looking. There is also no need for calibration. Figure 2.14 shows one possible set-up for this type of instrument. It should also be mentioned that if the sample is uniform and lambertian in nature, the sample measurement need not be radiance. In this case the irradiance emitted from the sample would be equal in all illumination conditions and view angles. Irradiance could therefore be directly measured in the same way as the hemispherical irradiance. This would allow for the instrument to have only one axis of movement.

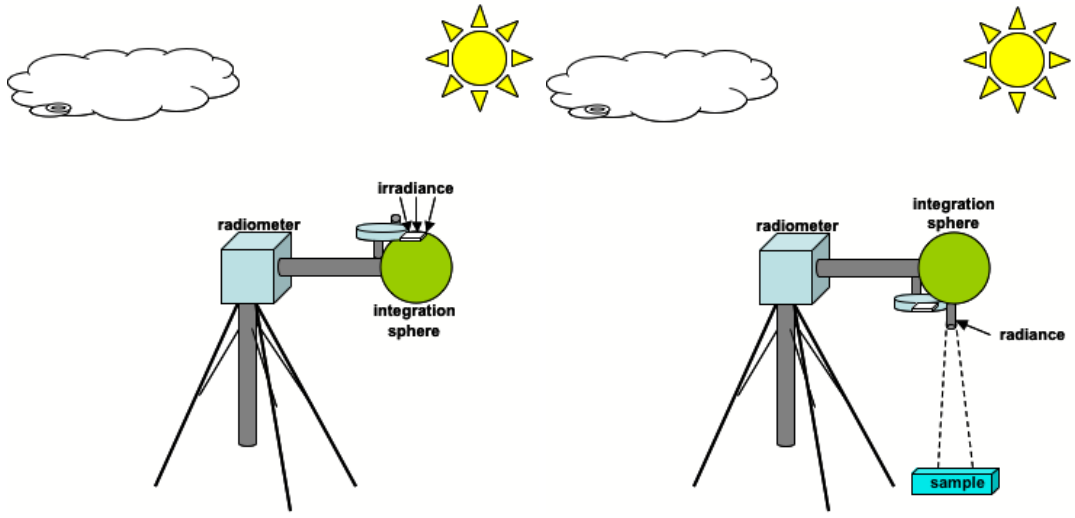

(a) Measurement of hemispherical irradiance. (b) Measurement of radiance from sample.

Figure 2.14: Measurement of reflectance using an integrating sphere.

Knowing the strengths and weaknesses of each approach will help in deciding which method will produce the best results for this research. Using a substance of known reflectance, placed just above the ground being characterized will allow for the best retrieval of the incident light field onto the surface. However, it will take time to physically switch the spectralon panel over and out of the ground scene. This means that the illumination conditions have time to change, thus causing the radiance term in equation 2.18 to not cancel perfectly. This will therefore lead to an error in the calculated reflectance. This problem can be minimized if the atmosphere is stable temporally, and if the measurements are taken close to noon where the sun is close to its solar maxima and is not changing illumination rapidly. However, in cloudy conditions this technique can produce significant errors[Duggin and Cunia, 1983].

The smaller the time between measurement of the illumination field and of the ground sample, the smaller the error due to changing irradiance in a variable atmosphere. This will provide for a much more accurate cancellation in the ratio. However, this method will have trouble accurately capturing the illumination seen by the ground sample. This is due to the fact that the cosine receptor can not be positioned in the same exact position as the ground in question. In fact, any slight change in orientation of the cosine receptor drastically changes the recorded signal. This method also requires the use of two spectrometers to allow the simultaneous capture of the ground radiance and the hemispherical illumination. This means that the two spectrometers must have the same relative response to each other in order for the cancellation to occur accurately. The use of an integration sphere should be the best balance between cost and delay in measurement. Automation is also a good option with this system since the number of moving parts is minimized. A final reason for making two measurements is that as long as the radiometric response of each measurement is the same, the measurements need not be radiometrically calibrated. If this approach is used with an ELM based reflectance retrieval algorithm, no calibration need be performed except spectral and the cross-calibration between spectrometers. This will become important in the development of the adaptive ELM algorithm.

2.2.3 Atmospheric Parameters

While measuring radiometric or reflectance values on the ground can help with an ELM based approach to reflectance factor retrieval, this does not necessarily help improve the output of radiative transfer models. Many radiative transfer based inversion approaches extract parameter input from within scene methods. However, in many cases an improvement could be achieved by measurement of these parameters directly. There are two main inputs that most RT based inversions are sensitive to, the water

vapor profile and aerosol content of the atmosphere.

The main approach used to determine the water vapor profile for RT inversion is a band-ratio of spectral channels sensitive to water dominated absorption in hyperspectral data. This approach can lead to errors in the retrieval when the reflectance is not linear with respect to wavelength [Qu et al., 2003]. If the shoulders of the absorption bands are slightly in error the retrieval will be significantly off, which means a high sensitivity to noise. Finally, if the sensor used does not have enough spectral resolution then this technique can not be used. One way to obtain a water vapor profile is to derive the information from a radiosonde. A radiosonde is simply a device that consists of a balloon and a small meteorological payload that measures temperature, pressure, and relative humidity as a function of height. An example of a radiosonde is shown in Figure 2.15.

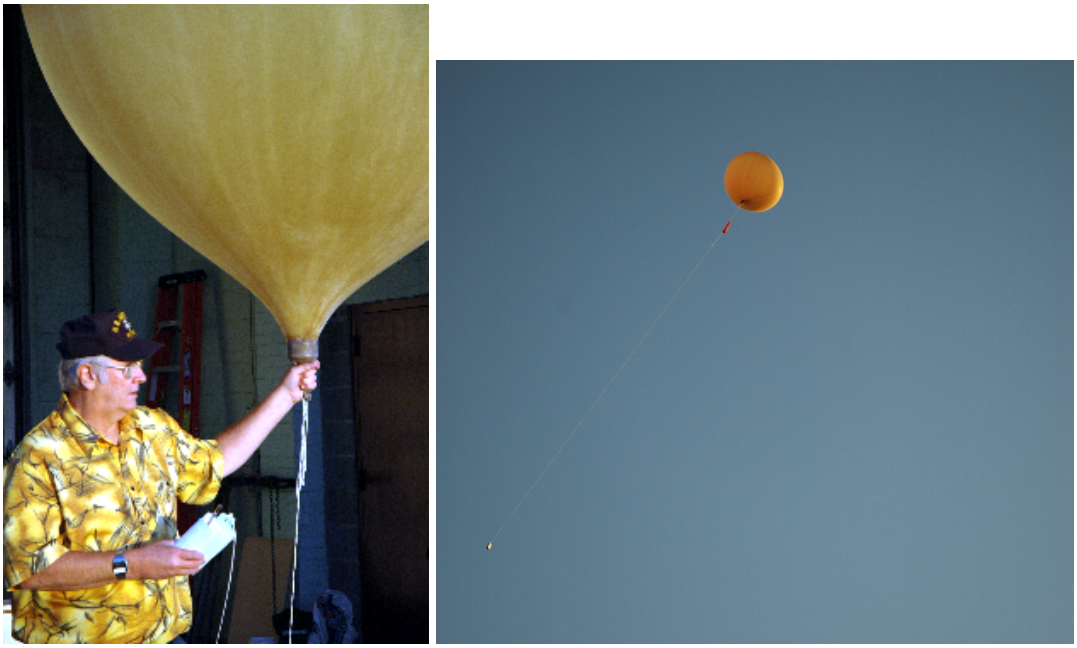

(a) The radiosonde just before launch. (b) The radiosonde during its ascent.

Figure 2.15: Radiosonde which consists of a balloon and small instrument package. A ground system is used to track the data which is transmitted from the payload.

Other methods have been developed that use both active (raman lidar) and passive (radiometer downwell measurement, and sun photometry) techniques to obtain water vapor profiles[Lazarevich et al., 2004],[Plana-Fattori et al., 1998]. While these methods can provide accurate measurement of water vapor, in cloudy conditions the water

vapor content of the atmosphere changes very quickly spatially. This means that the measurements obtained with ground truth methods will be valid for only a small spatial subset of the image.

The other major input for RT based models that is hard to predict is the aerosol optical depth. This is also hard to determine from within scene spectral information. The major method to obtain the optical depth of the atmosphere is by means of sun photometry [Schmid et al., 1997]. This method is attractive since it lends itself easily to automation. In fact, currently an automated system called AERONET (AErosol RObotic NETwork) is in operation and provides world-wide coverage of spectral optical depths [Dubovik et al., 2000]. This system makes use of sun-photometers manufactured by *CIMEL* which is shown in Figure 2.16.

Figure 2.16: The CE 318 by CIMEL used for automated measurement of the sun and sky. Currently in use by the AERONET project.

In general knowing atmospheric parameters will allow for a lower error in atmospheric inversion, at least with regards to modeling inputs. The drawback to measuring these parameters with equipment like radiosonde and sun photometers is one of expense. Most techniques either require personal to be present or are expensive. Both of these facts limit the number of measurements that can be made both in a temporal and spatial sense. The measurements made in this approach will therefore attempt to be both automated as well as inexpensive.

2.3 Cloud Cover and Remote Sensing

Since a major part of this research involves cloud cover, it is important to characterize the effects that clouds have on radiance. Two approaches will be made to explore these

effects, by making field measurements as well as using modeling software. MODTRAN4 includes a cloud model which has seen steady improvement. Figure 2.7 shows how MODTRAN positions a cloud layer in its model of the atmosphere. This positioning is an all or nothing sort of placement which does not allow for partial cloudy conditions. It can been seen in Figure 2.17 that the MODTRAN cloud model compares well with measured cloud spectra. It should be noted that MODTRAN5 also includes a cloud model which has a greatly improved multiple scatter algorithm [Berk et al., 2005].

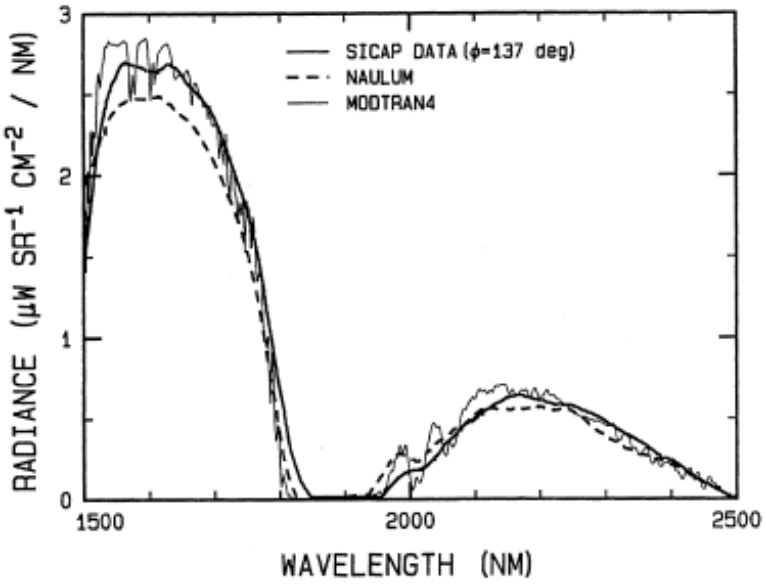

Figure 2.17: Graph showing a comparison between a cumulus cloud viewed by the SICAP circular variable filter cryogenic spectrometer and generated by MODTRAN [Berk et al., 1998b].

There are two main effects that clouds have on remotely sensed images. The first effect is to increase the multiple scattered photons directed towards the sensor. While this will pose problems for the retrieval of the reflectance factor, there have been successful attempts to invert to reflectance in the presence of this effect [McArdle et al., 1992]. The next effect seen by cloud cover is spatial / temporal variability of illumination. This effect will require the use of spatially distributed ground truth for accurate reflectance retrieval.

One conceptual tool that can be used to describe and evaluate the idea of spatially distributed ground truth is that of the sensor web. A sensor web is different from a distributed network of sensors in that its information is shared and used by other nodes

in the web [Delin and Jackson, 2001]. This is important in the context of automated ground truth since in order for each node to be truly automated it must make decisions about when to collect data by itself. For example, if the effects of cloud cover are being measured, a node may need to adjust its sample frequency up on days with lots of clouds as opposed to clear days. A sensor web is also more suited to perform automated sensor calibration. Such webs have demonstrated utility in several application areas including remote sensing of soil moisture [Teillet et al., 2003].

2.4 Background Summary

This background has reviewed the basic mathematical form, in terms of a governing equation, for energy reaching a sensor from the earth. Different types of atmospheric compensation routines were discussed which transform airborne measurements into units of ground reflectance. Different types of measurements that can be made from the ground were then illustrated. These included measurement of irradiance, radiance, reflectance, and several atmospheric parameters. The steps used to calibrate such measurements were also discussed. This background will give a good basis for understanding what tools are available when attempting atmospheric compensation. The approach used to improve upon current compensation algorithms will draw on many of the ideas presented in the background. This will lead to a relatively inexpensive, automated network of ground based measurements which are used in a novel algorithm to improve reflectance retrieval in the presence of clouds.

Chapter 3

Approach

3.1 Overview of Approach

The primary goal of this research is to develop an adaptive algorithm that can use auxiliary information to improve the calibration from sensor values to ground reflectance values. This adjustment will be spatially dynamic because the calibration will be modified on a pixel by pixel basis. An improvement over methods which apply the same calibration to the entire image should be evident in all atmospheric cases since the atmosphere is never completely homogeneous. This statement becomes all the more consequential when cloud formations are present over the scene. Just how consequential depends on the particular atmospheric conditions in which the imagery is taken.

In order to assess the need to modify the ELM to account for non-homogeneity in the atmosphere, the effects produced by clouds will be considered. This is done by first examining measurements of radiance from clouds and blue sky. The overall effect on the retrieved reflectance is then shown using data collected during the Multi-Modal Collect (MMC) performed at RIT in the summer of 2006.

The results from the MMC indicate that there is a need to modify the ELM approach when clouds exist in the scene. The theory behind modifying the ELM is developed and it is shown that improvement using auxiliary measurements should be possible. This is followed by a complete example of the new algorithm which has been implemented with simulated data using the radiative transfer code MODTRAN. The steps that will be required to implement the algorithm using real data will also be discussed.

Finally the requirements in terms of equipment and personnel needed to acquire the auxiliary data during a collection is discussed. This also includes a discussion of the computation requirements to run the algorithm.

3.2 Cloud effects

Since accurate reflectance retrieval with partial cloud cover is the goal, the spatial and spectral nature of clouds must be considered. The background review shows that while there are many reports of inversion techniques, all present results for atmospheric conditions that are very clear and homogeneous. A preliminary study was therefore performed to assess the impact of clouds on both observed radiance and retrieved reflectance.

3.2.1 Sky Radiance Measurement

In order to study the spectral effects, an up-looking radiometer with an apertured fiber lead was attached to an equatorial mount which could be positioned accurately with stepping motors. This provided the sensor with the ability to capture the sky radiance at different angles, which allowed for greater ease in locating clouds as well as the sun. The aperture was fitted with a 3° field of view and samples of the hemisphere were collected every 10°. Figure 3.1 shows how the mount could move to capture the radiance from two sets of clouds.

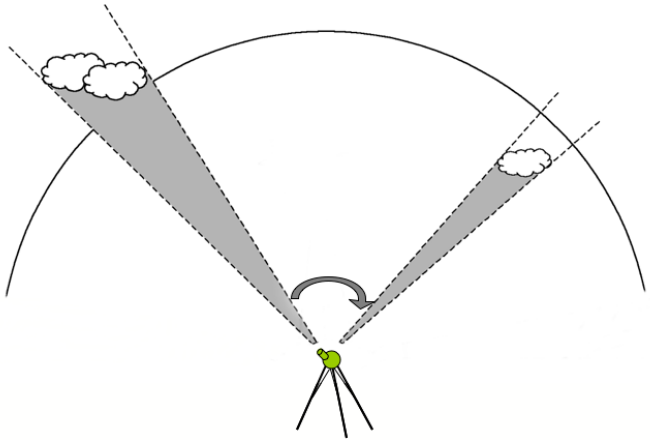

Figure 3.1: Diagram showing how radiometer was used to collect cloud radiance.

Figure 3.2 shows a grouping of data from an arc aligned with the sun, but using zenith angles which did not include the sun. The direct sun intensity is also plotted as a reference of the brightest intensity possible. It can be seen that while there is some difference in the downwelling radiance due to angle, the difference is quite small in magnitude compared to the sun intensity. At two of the samples, clouds were present

which show an increase of the sky radiance of around 5 times. This shows that even in areas that are not directly in cloud shadow, there will still be significant difference in the downwelling radiance in near-by areas.

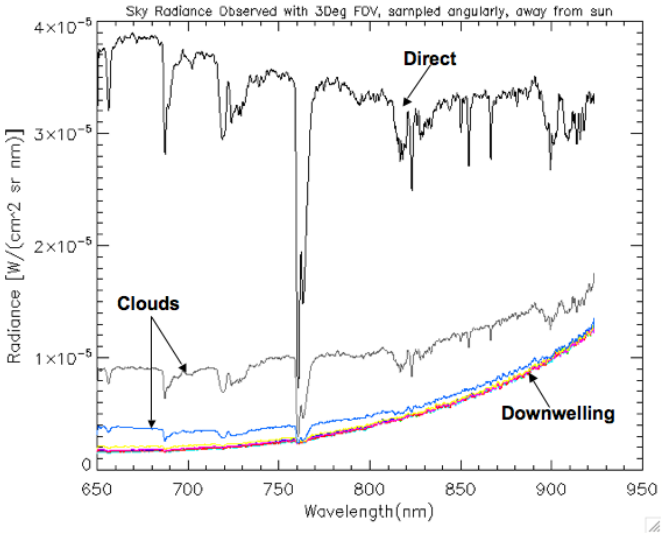

Figure 3.2: Plot showing sun compared with downwelling radiance in 10° increments, stepping away from sun on sun-arc. Clouds present in two samples, showing deviation from downwelling radiation.

The change of the direct solar term due to a cumulus cloud can be seen in Figure 3.3. The black curve is the spectra of the sun without cloud cover. The colored curves show the radiance observed when a cloud drifts in front of the sun. All curves were taken within a two minute time frame with a 400ms integration time using a 3° FOV. The data illustrates that there is significant variability within the cloud, thus stressing the importance of accounting for temporal variability when making measurements in the presence of clouds.

The observed radiance has not only a change in magnitude, but also has a significant change in spectral structure. In order to better observe the spectral effect that this particular cloud had on the direct solar term each curve was Euclidean Normalized using equation 3.1.

$$\boldsymbol{L}_{norm} = \frac{\boldsymbol{L}}{\|\boldsymbol{L}\|} \tag{3.1}$$

Figure 3.4 shows that there is spectral modulation in the curves measured through the cloud compared to the unobstructed sun radiance (black curve). While this effect

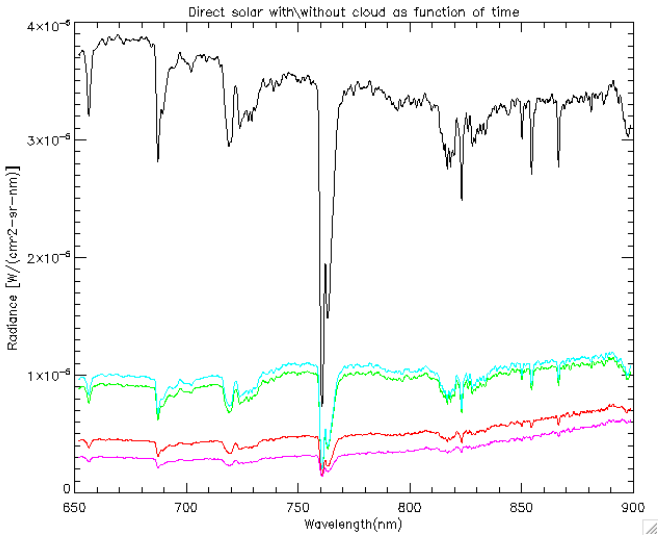

Figure 3.3: Plot showing radiance from sun as cloud travels by. Each curve is a temporal sample, with samples spaced over a two minute time period.

needs further analysis, it can be concluded that any adjustment performed must be done on a band by band basis.

This data gives us an understanding about how clouds affect the radiance coming from a particular portion of the hemisphere. However, it does not tell the story of how an ELM reflectance retrieval would be changed. The next section presents the results from a data collect which will address this story.

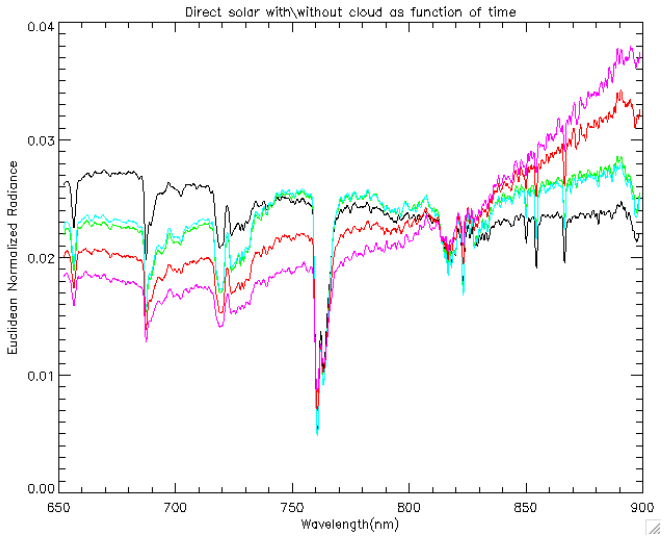

Figure 3.4: Plot showing radiance from sun as cloud travels by, with each curve being euclidean normalized.

3.2.2 Multi-Modal Collect Results

The MMC was a data collection that took place on May 10th in 2006 at RIT. Data was collected using several different pieces of equipment. For this study the data collected by the Modular Imaging Spectrometer Instrument (MISI), an Analytical Spectral Devices spectrometer, and an Ocean Optics USB-4000 VIS/NIR spectrometer were used. The location of different points of interest in the MMC is shown in Figure 3.5.

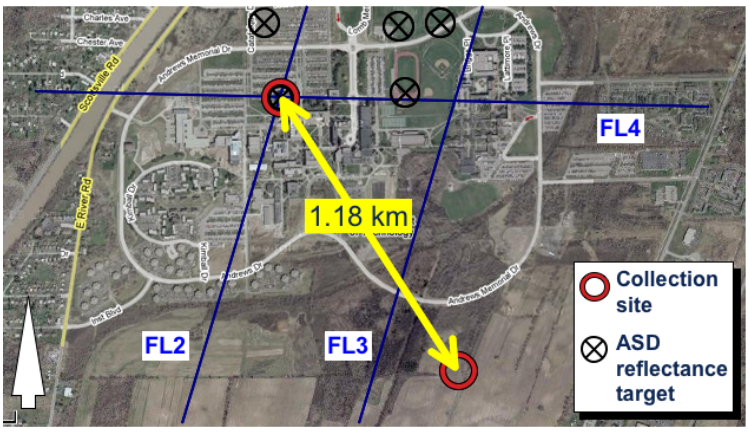

Figure 3.5: The physical layout of the MMC over RIT campus.

The atmospheric conditions started out to be visibly clear, with increasing cloud cover throughout the day. This trend is shown in figure 3.6 which shows three selected flight lines out of the 23 total passes during the collect. The cloud conditions can also be observed with respect to the location of the aircraft in Figure 3.7.

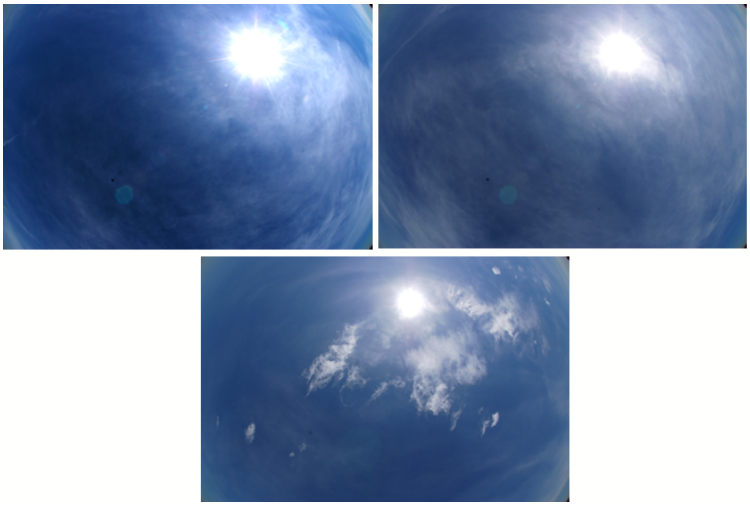

Figure 3.6: The cloud conditions during flight lines one, nine, and fifteen which occurred at 11:10, 11:44, and 12:10 respectively.

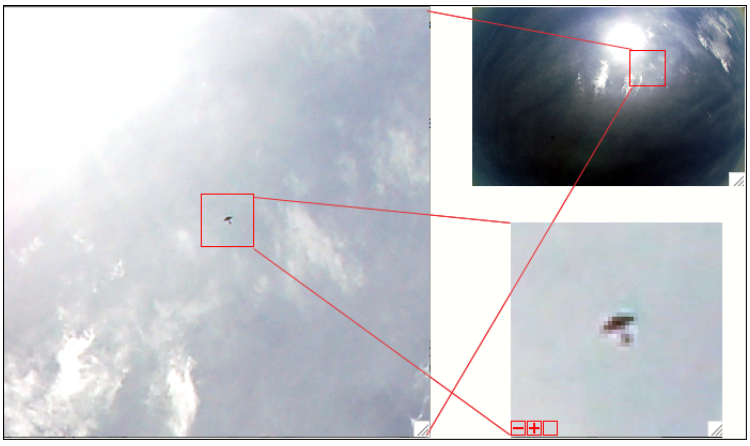

Figure 3.7: The location of MISI during flight line nine of the MMC.

Earlier it was shown that temporal variability exists as clouds move through a scene. It is also important to know if there is variability spatially across the scene. The total radiance incident onto a cosine collector, which will be referred to as a full SKY measurement, was therefore measured at both collection sites. The time between measurements was minimized by using a walky-talky system between the two sites. A countdown was performed so that each operator could make the measurement as close to the same time as possible. As shown in Figure 3.8 there is a large difference between the two collection sites in total radiance which must be taken into account.

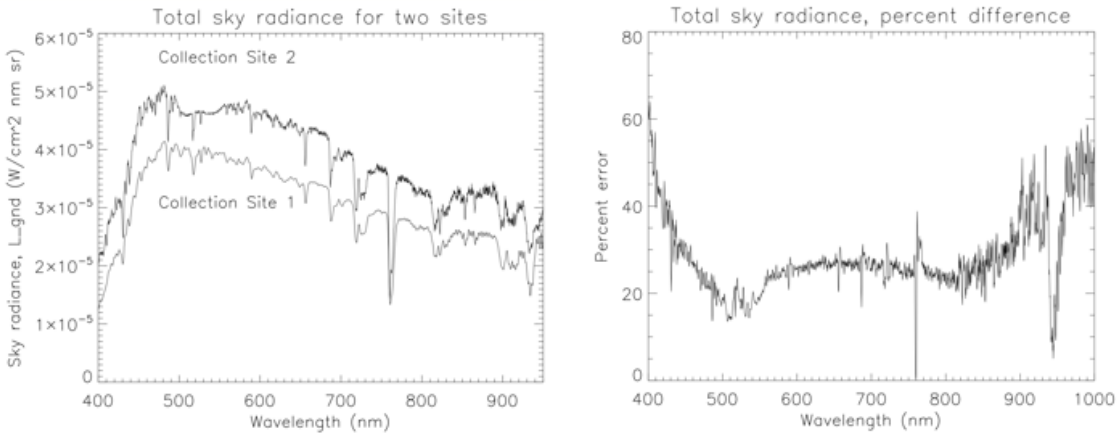

Figure 3.8: The spatial variability between the two collections sites in terms of radiance and percent change.

Considering the effect that clouds have on the illumination of a scene over a relatively short distance, any attempt to remove their influence from a scene using ground truth must be well coordinated temporally. This is due to cloud movement which will produce the same type of illumination change as observed between sites. Any measurements must therefore be made at the same time as when the image is acquired from the aircraft to minimize temporal variability. This suggests the use of a sensor web in which each sensor node is aware of the aircraft and can autonomously act to synchronize data acquisition. Assuming this is the case, the temporal variation is removed, and an algorithm can be developed which uses information from the sensor web to remove spatial variability. The next section will outline an approach to incorporate data from a sensor web and insert it into a reflectance retrieval which is based on the simple linear empirical line method.

3.3 Adaptive ELM (AELM)

3.3.1 Theory

As explained in the previous section, one major issue facing the ELM is that of variability created by clouds. It has been suggested that the question in remote sensing is not 'how clear is the sky', but 'how thick are the clouds that I'm looking through?' [Shanks and Shetler, 2000]. A cloudy atmosphere will violate the assumption made in ELM that the atmosphere is spatially uniform. This will change the linear fit spatially across the scene in equation 2.8 by causing at least τ_1 and L_d to vary. It should be noted that both τ_2 and L_u can also be modulated in this situation. This effect will be assumed to be negligible since the path from the ground to the sensor for an aircraft is much smaller compared with the path from the ground to space. It has also been assumed that there is a clear line of site between the sensor and the ground which will further reduce the likelihood that the two parameters would vary. The spatial change in L_u will be neglected as well since there are effectively only three situations in which a cloud will effect L_u. If the cloud is far away, scattered light will have a low probability of reaching the sensor. If the cloud is in the path, then the scene will be blocked. The only situations where a noticeable effect can be detected is if the cloud is physically close to the ground-sensor path, or if the target is sun-lit but the path is shaded. However, the primary contamination from clouds is due to light reflected off the surface [Fairbanks, 1999] so the change in upwelling radiance for now is ignored.

Before attempting to adjust the slope for spatial variation, a linear fit must be performed at a reference site between observed digital count and reflectance using the method outlined in section 2.1.1. This should take place at a calibration site where the assumptions for a standard ELM hold. As long as the site consists of two regions, with high and low reflectance, that are spatially close to each other the ELM can take place in cloudy conditions. This configuration can be seen in Figure 3.9.

The slope and intercept can be produced by use of equation 2.8. This means that we will have a value for the upwelled radiance and the 'total' sky radiance, or $\left(\frac{E'_s cos\theta \tau_1}{\pi} + L_d\right)\tau_2$. In Figure 3.9, a near-by pixel will be under the influence of a cloud, and in worst case, a cloud shadow. As mentioned before the cloud producing the shadow is not spatially close to the ground-sensor path, therefore τ_1 and L_d will be modulated, but not τ_2 or L_u. In other words, it will produce a dim region in the image, but the cloud itself will not be seen. It should be noted that even if the remote pixel is not in a cloud shadow, the illumination will still be modified by the cloud. As shown in the previous section, this modification not only changes the magnitude, but also the spectral nature of the signal. This case is the primary thrust of the effort. This

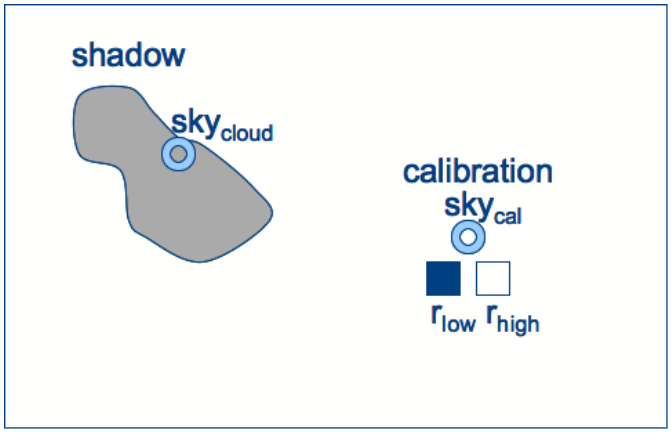

Figure 3.9: Scene where calibration site is under direct sun, but remote site is under cloud shadow.

change must be accounted for in order to achieve accurate reflectance retrieval. This can be done by adjusting the slope term found at the test site by a measurement made at the remote region. This measurement must be very fast and simultaneous since in cloudy conditions the illumination field changes very rapidly for reasons discussed above as well as [Anderson et al., 2003]. One measurement that can be made quickly is: $E_s' cos\theta\tau_1 + E_d = SKY$. This term is simply the energy from the entire hemisphere and can be measured with a simple diffuse cosine receptor. We can express the governing equation used in ELM for the sensor reaching radiance in terms of the SKY quantity, shown in equation 3.2.

$$\begin{aligned} L_{sensor} &= \frac{SKY\tau_2}{\pi} r + L_u \\ &= mr + b \end{aligned} \tag{3.2}$$

This formulation assumes the measurement of Lambertian surfaces since we are simply dividing by π to convert from irradiance to radiance. After measuring the SKY, it is possible to solve for τ_2. Now for each location away from the calibration site that has a SKY measurement, the slope can be adjusted as shown in equation 3.3.

$$\begin{aligned} \tau_2 &= \frac{m_{calSite}\pi}{SKY_{calSite}} \\ m_{remote} &= \frac{SKY_{remote}\tau_2}{\pi} = \frac{SKY_{remote}}{SKY_{calSite}} m_{calSite} \end{aligned} \tag{3.3}$$

This theory can also be extended to use imagery that is not in absolute radiometric units. Equation 3.2 can be re-written as equation 3.4 which shows how the governing equation for sensor reaching radiance can be written in terms of digital count (DC).

$$\begin{aligned} DC &= \frac{SKY\tau_2 c}{\pi} r + b \\ &= mr + b \end{aligned} \tag{3.4}$$

where c is a calibration constant and b is a sensor bias. As long as the SKY measurement is still calibrated, the above process is simply repeated as shown in equation 3.5 where $k = c\tau_2$.

$$\begin{aligned} k &= \frac{m_{calSite}\pi}{SKY_{calSite}} \\ m_{remote} &= \frac{SKY_{remote}k}{\pi} = \frac{SKY_{remote}}{SKY_{calSite}} m_{calSite} \end{aligned} \tag{3.5}$$

The final extension discussed here is to assume that the only calibration performed is that of a cross-calibration between the SKY measurements. The SKY measurement can be thought of as the actual energy emitted by the sky which is then modified by the sensor by some factor (c), shown in equation 3.6.

$$SKY_{measured} = \left[E_s' cos\theta + L_d\right] c \tag{3.6}$$

The equipment at the remote site can be calibrated to respond to irradiance in the same way as at the cal site. If this is the case, then the response of the remote site spectrometer has been adjusted to equal that of the cal site. Equation 3.7 shows this relationship between responses.

$$c_{calSite} = c_{remoteSite} \cdot c_{adjustment} \tag{3.7}$$

If the SKY measurements from equation 3.6 are substituted into equation 3.5 then the c-terms cancel in the ratio. Equation 3.8 shows this cancellation.

$$
\begin{aligned}
k &= \frac{m_{calSite}\pi}{SKY_{calSite} \cdot c} \\
m_{remote} &= \frac{SKY_{remote} \cdot c_{remote} \cdot c_{adjustment} \cdot k}{\pi} \\
&= \frac{SKY_{remote} \cdot c}{SKY_{calSite} \cdot c} m_{calSite} \\
&= \frac{SKY_{remote}}{SKY_{calSite}} m_{calSite}
\end{aligned} \tag{3.8}
$$

This theory will allow for the correction of the linear fit found using ELM by making a simple and fast measurement on the ground. No calibration other than a cross-calibration between SKY measurements needs to be made. It should be noted that this approach will work only for areas within a scene that have a SKY measurement. This means that a method to model the SKY term will need to be devised as well. The next section will explain how this theory has been implemented in a simulation.

3.3.2 Simulation Overview

In order to simulate the downwelling radiance produced during a partial cloudy day, the sky can be broken up into many discrete parts. These parts will be called quads and are shown in Figure 3.10.

The radiance produced from each quad can then be found using a radiative transfer model. One model that already has an advanced capability to incorporate many atmospheric as well as geometric parameters is the radiative transfer code MODTRAN. The radiance present in a quad can be calculated by 'pointing' the line-of-sight of MODTRAN at the center of each quad. Each of these values for a clear atmosphere is shown overlaid onto each quad in Figure 3.11.

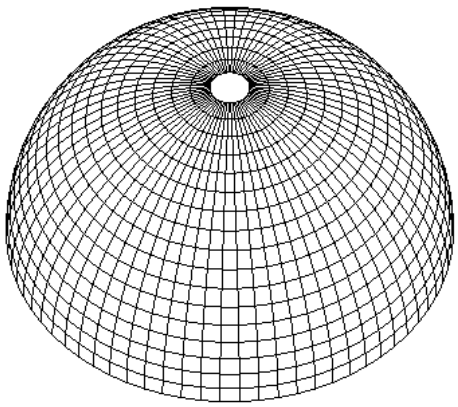

Figure 3.10: The hemisphere is broken up into discrete parts, called quads. In this case, there are 17 quads in the zenith and 72 in the azimuth.

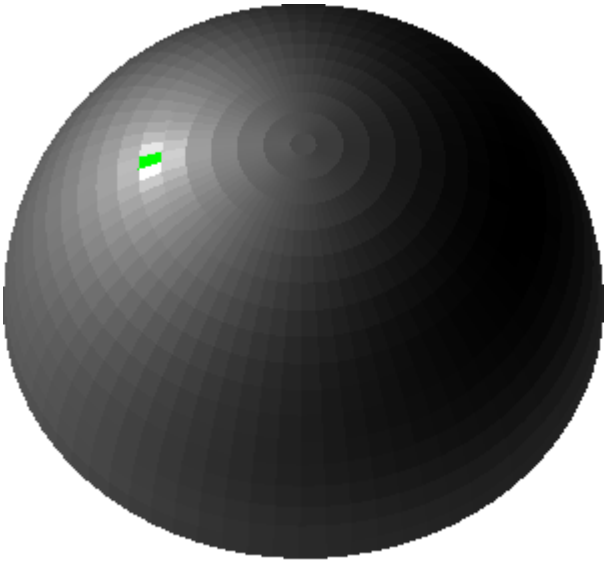

(a) Scaled with high cutoff value, detail in low radiance regions minimal.

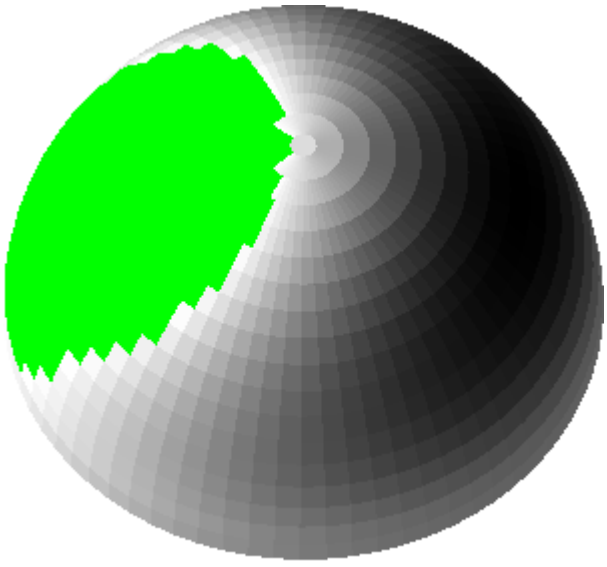

(b) Scaled with lower cutoff, detail in low radiance regions enhanced.

Figure 3.11: Two images depicting the radiance field in a clear hemisphere. Each image contains the same field with different scaling.White represents a higher magnitude of radiance and green represents quads that have been blocked.

Now that a database of quads can be created, it is possible to use the cloud model in MODTRAN to create a database of cloudy quads. This database can be used as input into the simulation to help create the sensor reaching radiance. Two databases, one for a clear sky and one for a cloudy sky are input into the ”Mark Quads” algorithm. A cloud mask is also input into the algorithm which contains one for pixels that are clouds and 0 for pixels that are clear sky. The ”Mark Quads” algorithm outputs a database which contains both clear and cloudy quads in the configuration indicated by the cloud mask. Figure 3.12 shows this process.

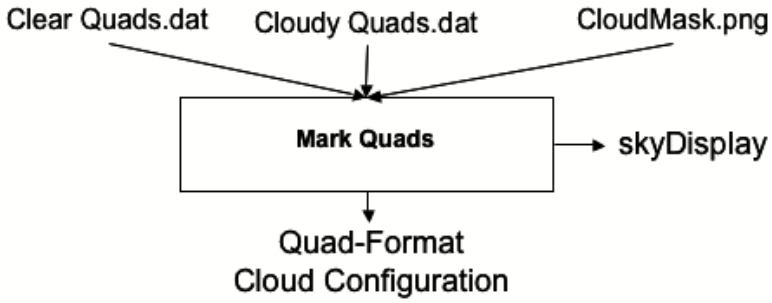

Figure 3.12: Input / output flow for mark quads algorithm.

This configuration is used to create the SKY radiance term in the generate SKY radiance algorithm. This algorithm makes a database which has the correct mix of cloud and clear pixels based on the output of the ”Mark Quads” algorithm. The database is then integrated using equation 2.5 to produce downwelling irradiance. The irradiance is divided by π to produce the L_d term in equation 2.7. Figure 3.13 shows this process.

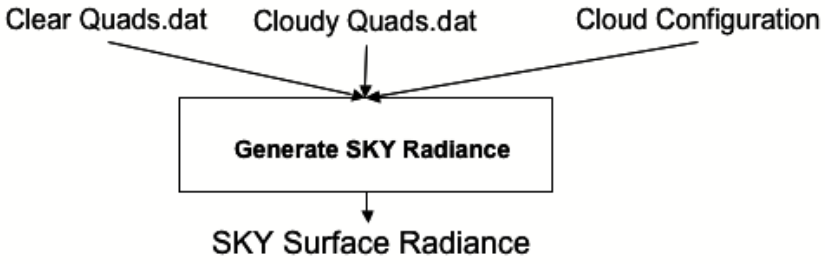

Figure 3.13: Input / output flow for generating SKY algorithm.

The cloud mask is then changed by a simple linear shift and a new SKY_{shift} term for this changed cloud configuration is produced. It should be noted that in a real world situation a more complicated method which is geometrically correct must be used to

shift the cloud locations, as outlined in appendix C. Another database which contains a slightly thinner cloud layer is finally used to produce the SKY_{thin} term.

The next step is to generate sensor reaching radiance for the SKY and SKY_{shift} terms using the "Generate Sensor Radiance" algorithm shown in Figure 3.14. This algorithm uses the governing equation to produce sensor reaching radiance as defined in equation 3.2.

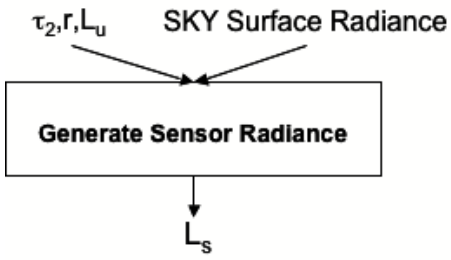

Figure 3.14: Input / output flow for generate sensor algorithm.

The "Generate Sensor Radiance" algorithm is run three times by choosing values for τ_2, r, and L_u. The first two runs use the SKY term with r equal to 0.05 and 0.9. These values will be called $L_{[1,low]}$ and $L_{[1,high]}$, indicating the radiance for cloud configuration one with low and high reflectance values. The third time the algorithm is given SKY_{shift} and r is set to 0.25. This value is called $L_{[2,medium]}$ which indicates the shifted cloud configuration with a medium reflectance.

A linear fit is then performed using the L_1 values. The fit is used to produce reflectance from $L_{[2,medium]}$ which will show how much error a traditional ELM will produce. The fit is then adjusted using the SKY_{thin} radiance in the adaptive ELM algorithm. Finally the adjusted fit is used to invert the $L_{[2,medium]}$ radiance. This gives a sense of how sensitive the algorithm is to an incorrect estimate of cloud thickness. Figure 3.15 shows how this entire process is implemented.

This simulation relies on several inputs such as the quad databases and the cloud mask. The generation of each input will now be clarified.

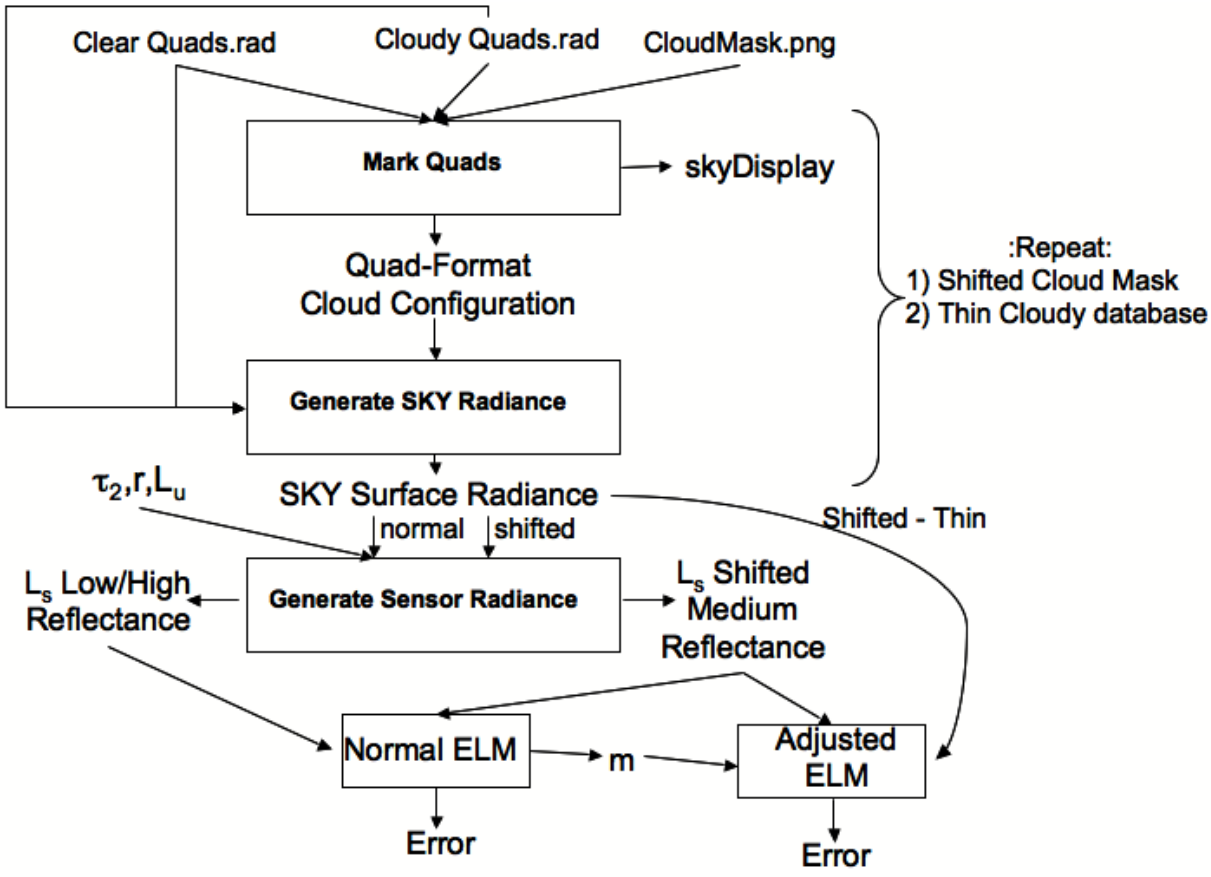

Figure 3.15: Process used in adaptive ELM simulation.

3.3.3 Quad Database Generation

The process of running MODTRAN for each quad has been automated and incorporated into a graphical user interface (GUI). A flowchart of how the interface operates is shown in Figure 3.16 and a snapshot of the user interface is shown in Figure 3.17.

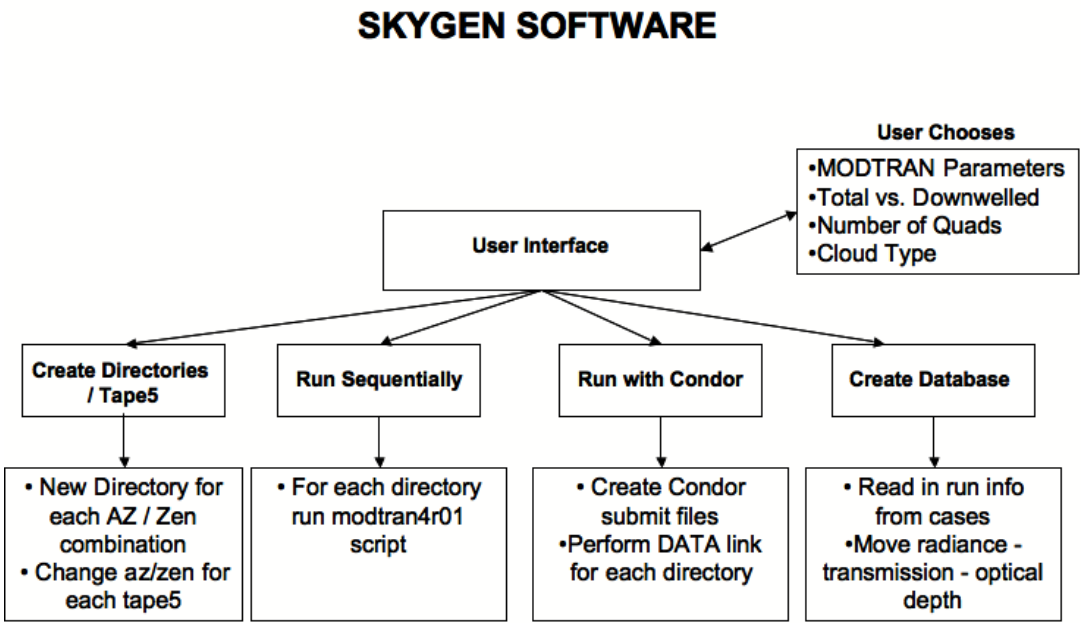

Figure 3.16: How the skygen GUI interfaces with user.

Once the radiance for each quad is found, a numerical integration of equation 2.5 can be performed to find the total irradiance of the sky. Two tools have been developed to do this. The first visualizes the quad database by projecting it into rectangular coordinates and then performing a scaling of the radiance. A plot is also generated of the total illumination, which is the result of numerical integration of equation 2.5. The plot has been scaled by π into units of radiance. The GUI will also read in a .adb file created for the software DIRSIG. Figure 3.18 shows the interface.

The skygen interface will allow users to create databases using the MODTRAN cloud database. The clouds present in an image can be grouped into two general categories. The first category is 'bright', which refers to clouds that are under direct illumination from the sun. The second is 'dark', which are clouds that are not being illuminated directly, both of which are shown in Figure 3.19.

MODTRAN, as discussed in Chapter 2, by default creates a solid layer of clouds. This eliminates the possibility of getting light that has been scattered from the side of

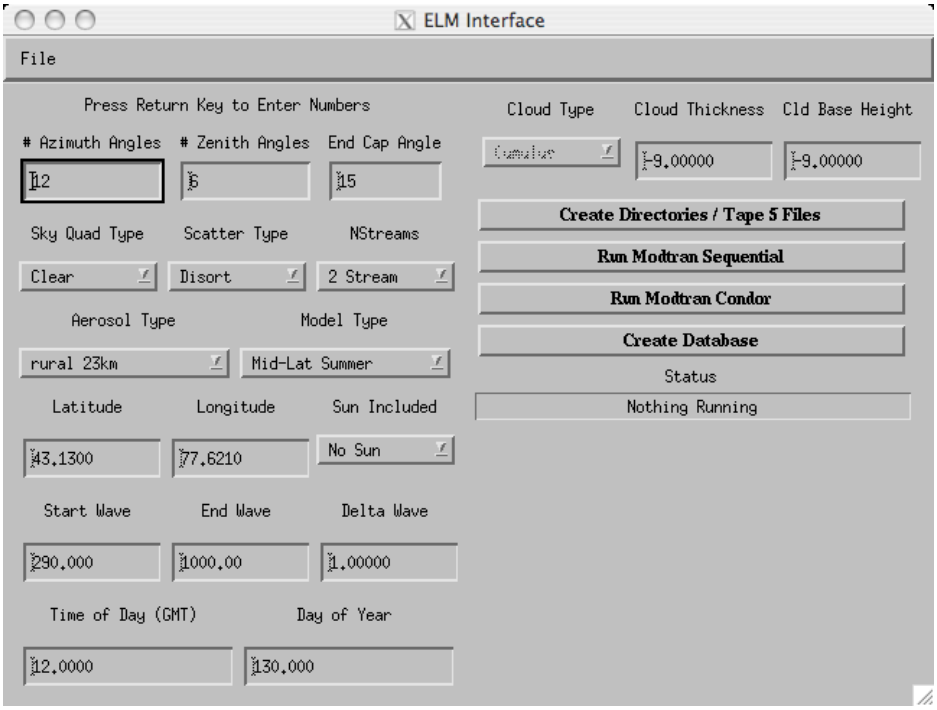

Figure 3.17: A snapshot of the skygen interface.

a cloud. In order to get the 'bright' variety of clouds out of modtran, it must be run with a different geometry. Both varieties are shown in Figure 3.20.

A problem arises, however, when trying to model the bright clouds in the way shown in Figure 3.20. The dark / bright paths do not travel through the same atmosphere. The correct path, or the path that an observer on the ground would see, is taken by the dark cloud geometry. In order to get the correct geometry for the bright cloud runs, a single run was done with MODTRAN looking down at the cloud from just above the cloud deck. This radiance was then modified using the transmission and path radiance present along a path from the ground to the bottom of the cloud deck, as shown in equation 3.9.

$$L_{bright} = L_{cloud}\tau_{path} + L_{path} \tag{3.9}$$

The transmission and path radiance were obtained by running MODTRAN with the cloud model turned off since we are trying to model a partial cloudy day where the path will be sunlit. Figure 3.21 shows how a bright cloud quad is produced using this method.

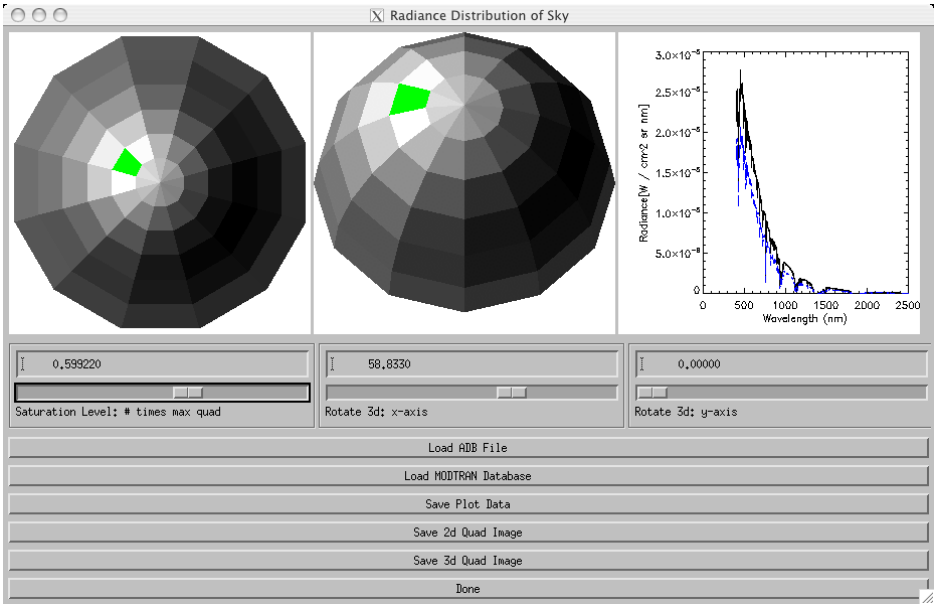

Figure 3.18: Visualization of a clear sky with 72 quads. Green indicates quads that have been purposely saturated to allow for re-scaling. Gray-scale value summed radiance across wavelengths. Plot shows integrated irradiance divided by π to convert in units of radiance where blue is all quads that are not green and black is total.

These programs provide one half of the required input for the simulation. The other half of required data takes the form of a cloud mask which is discussed in the next section.

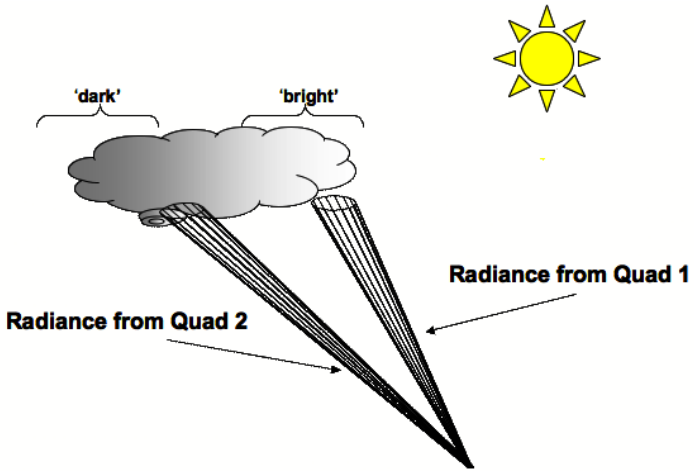

Figure 3.19: Image showing how one cloud can have different levels of radiance due to scattering effects.

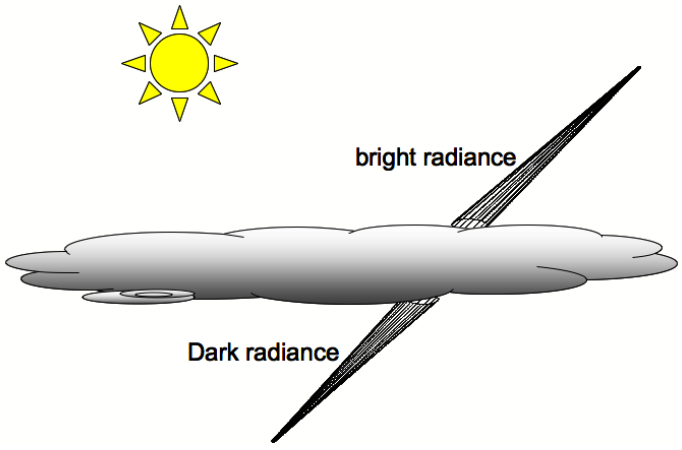

Figure 3.20: Two types of cloud radiance obtained by simply moving the observer location in MODTRAN.

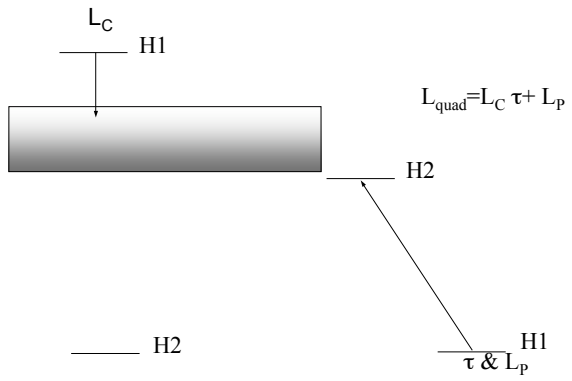

Figure 3.21: Two runs used to produce a bright cloud quad. H1 and H2 are the positions of the observer and target in MODTRAN.

3.3.4 Cloud Mask Algorithm

In order to use the adaptive ELM, it must be decided which quads in the sky database to turn into clouds. This is done in the simulation by taking a fisheye image of the sky and performing several image processing steps. Figure 3.22 shows a flow chart for the fisheye algorithm that was used to create a cloud mask from a fisheye image of the sky taken with a Nikon D50 digital SLR.

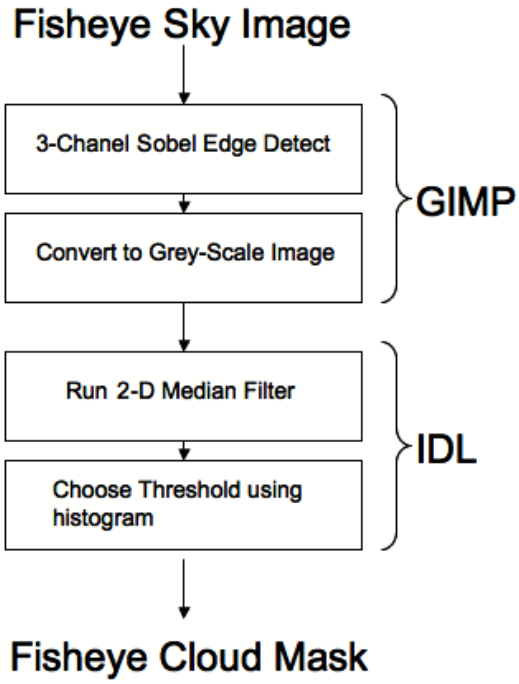

Figure 3.22: Flowchart of cloud mask generation algorithm.

The results of the cloud mask generation for an image taken during the Multi-Modal Collect (MMC) are shown in Figure 3.23.

Next the cloud mask needs to be used to decide which quads in the sky database should be a cloud. The decision to make a quad cloudy is made if the number of cloud pixels in a quad is greater than a certain percentage, in this case 15 percent. The results of quantizing the sky in this way is shown in Figure 3.24. It can clearly be seen that the higher the number of quads, the better the representation of the cloud configuration.

The above method extracts bright cumulus type clouds from the fisheye images taken during the MMC. While this method was used for simulation purposes to keep the cloud type simplified it will be necessary to develop an algorithm that can obtain

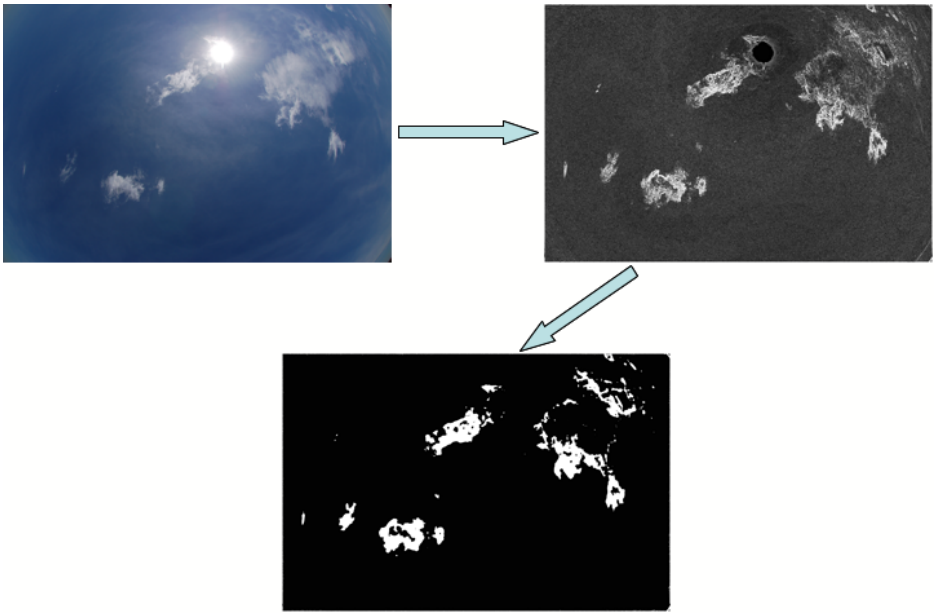

Figure 3.23: Output from cloud mask algorithm.

both bright and dark cloud types when applying the AELM to real data. This process will be outlined in section 3.3.6.

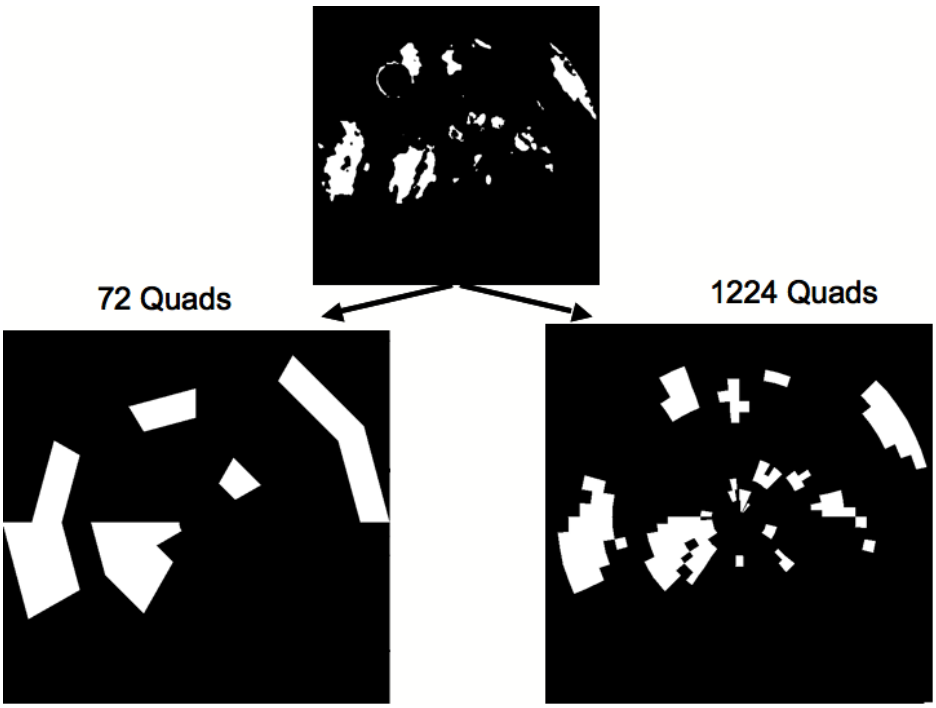

Figure 3.24: Turning a cloud mask into a quad database.

3.3.5 Simulation Results

Developing the inputs for the simulation which take the form of SKY radiance databases and cloud masks have been discussed. This section presents the results of running the algorithm with an example cloud configuration. The input cloud mask is based on a MMC collect flightline which has been chosen for adequate cumulus cloud cover. The cloud mask is shown in Figure 3.25

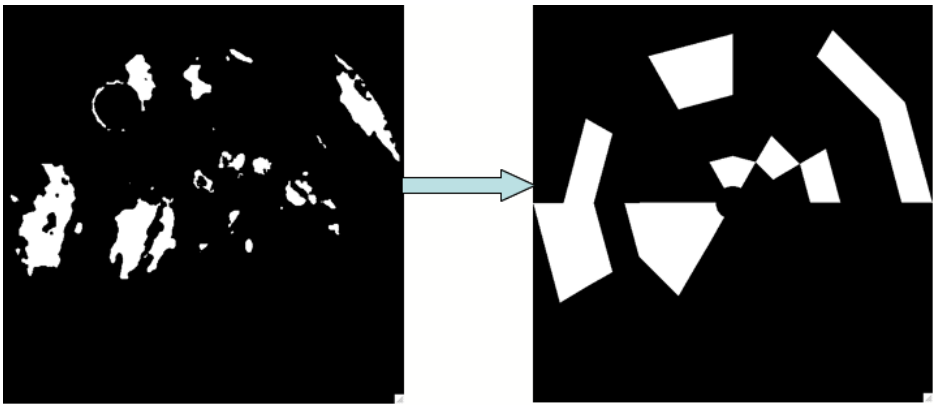

Figure 3.25: The cloud mask used in simulation, both original and quantized into 72 quads.

The cloud mask was then shifted down and to the right by 150 pixels to simulate the cloud configuration at a different ground location. This configuration is shown in Figure 3.26.

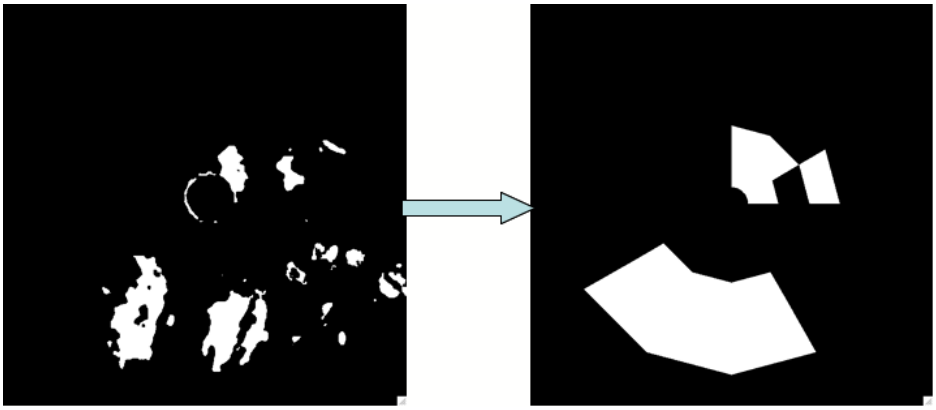

Figure 3.26: The results of shifting the original cloud mask.

The simulation was run twice, once using the dark cloud database and once using the bright cloud database. This produced the SKY configurations shown in Figures 3.27 and 3.28.

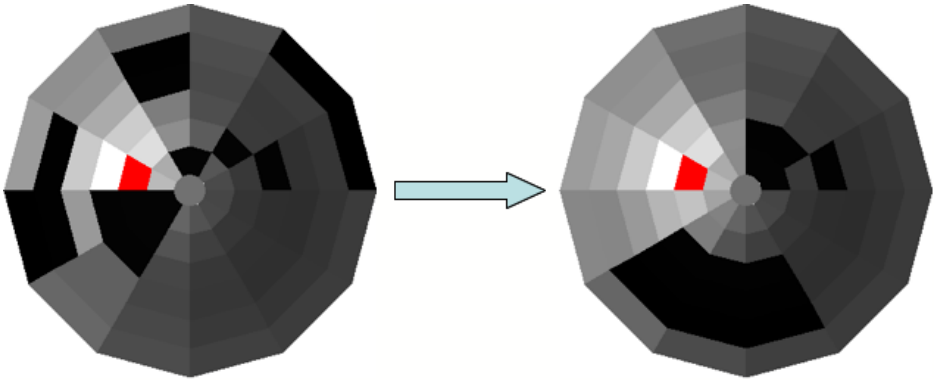

Figure 3.27: Dark clouds used in SKY database, red quad indicates sun location.

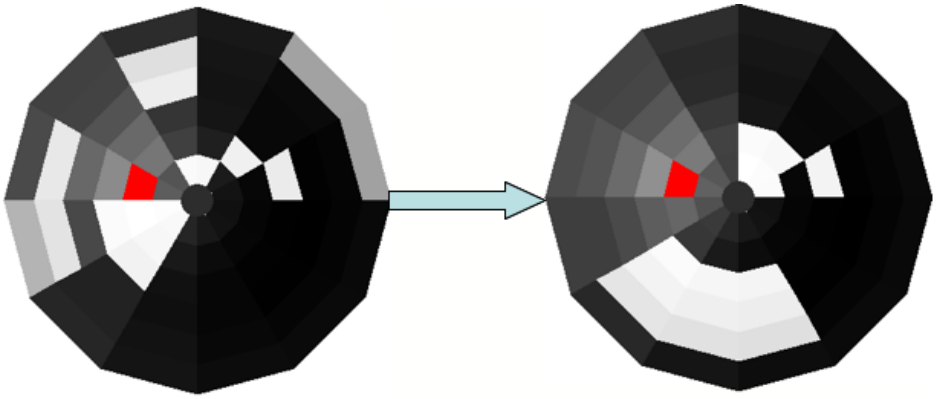

Figure 3.28: Bright clouds used in SKY database, red quad indicates sun location.

In both the dark and bright cloud case, the first cloud configuration places a cloud very near the quad which contains the sun irradiance as seen in Figures 3.27 and 3.28. Configuration two removes cloud cover from the area surrounding the sun, so it should produce a larger value for the SKY term. This is confirmed in Figure 3.29 which shows the sensor reaching radiance produced by each of the two SKY configurations for both the dark and bright cloud cases.

An ELM was then performed to produce a linear fit between radiance and reflectance using the first cloud configuration. The sensor reaching radiance for target

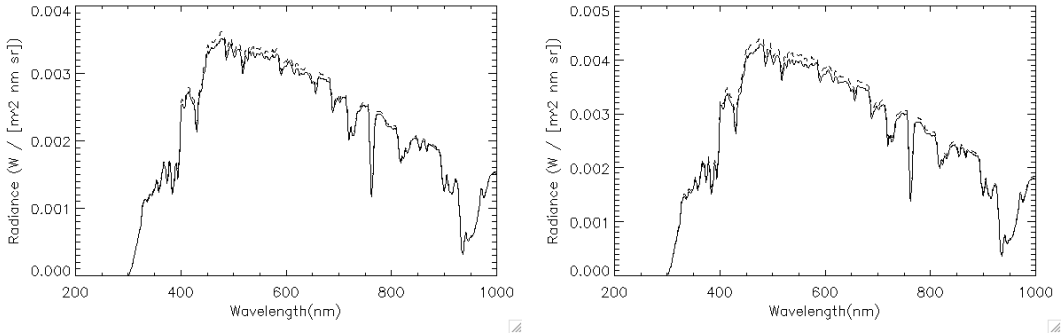

(a) Dark Clouds Used (b) Bright Clouds Used

Figure 3.29: Sensor reaching radiance produced by different cloud configurations using a target reflectance of 90%. Solid line is cloud configuration one, dashed line is cloud configuration two.

reflectances of 5% and 90% were used. The ELM was then applied to the sensor reaching radiance produced by a 25% reflector using the second cloud configuration. This results in an error in retrieved reflectance which is shown in Figure 3.30 and are below 5% , or under 1.25 reflectance units.

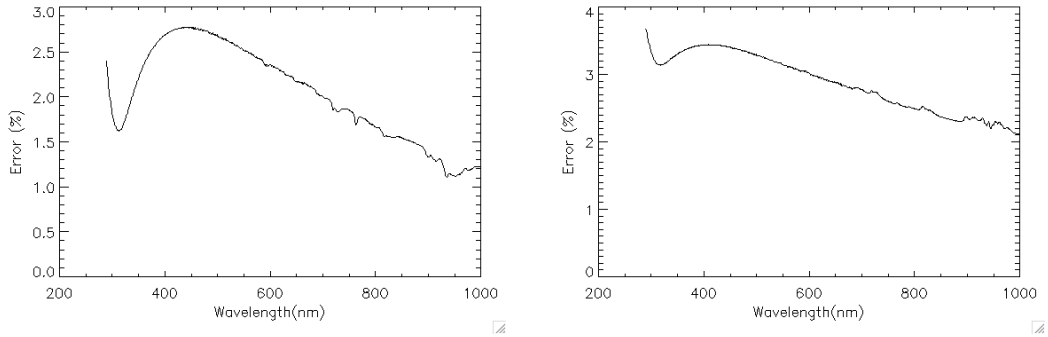

(a) Dark Clouds Used (b) Bright Clouds Used

Figure 3.30: Error produced when retrieving reflectance from the sensor reaching radiance of a 25% reflectance target.

The ELM slope was then adjusted to account for the change in radiance due to the cloud shift. This correction can be done perfectly since the data was simulated. The adjustment was therefore done with clouds in the second configuration, but with an error in the cloud thickness. The error in reflectance retrieval with the unmodi-

fied ELM was under 5% so twice this error was used in cloud thickness to see if the adaptive ELM could still improve the ELM results. The results of this correction are shown in Figure 3.31. This shows that a 10% error in cloud thickness does not keep the correction from improving the error from the original ELM. There is a significant decrease in the error (of around one to two reflectance units) for retrieved reflectance across most bands. One exception is around the water absorption bands, 940nm, for the bright cloud model. More work needs to be done to study the reason for this as well as the consequence of varying different cloud parameters to judge the effect on the performance of the correction.

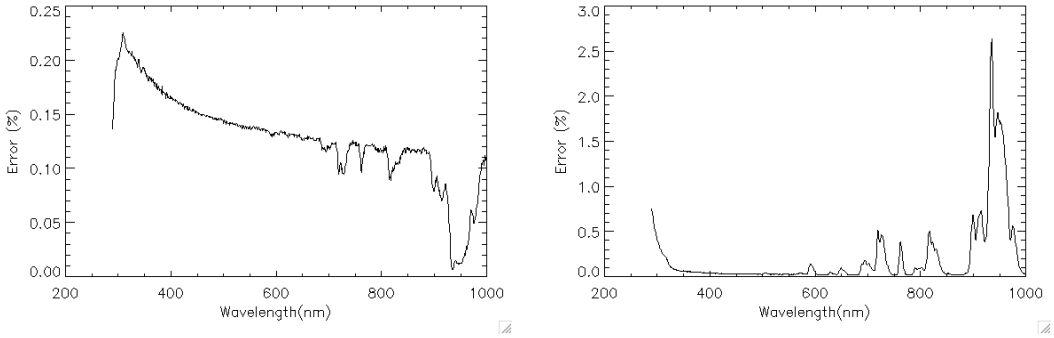

(a) Dark Clouds Used (b) Bright Clouds Used

Figure 3.31: Error produced when retrieving reflectance from the sensor reaching radiance of a 25% reflectance target using adaptive ELM. The clouds used to adjust ELM slope have a 10% error in thickness.

3.3.6 Adaptive ELM using Real Data

The adaptive ELM will be able to adjust the linear fit of an ELM for each site which has a SKY measurement. Each location in the image which is without this measurement will require an adjustment of the measurement to account for spatial in-homogeneity. To accomplish this, the SKYGEN interface will be run with varied inputs until a close match of the measured SKY radiance is achieved at the calibration site. The cloud locations in the hemisphere will then be shifted to match the locations of adjacent pixels. Each pixel will now have a modeled value for the SKY radiance allowing an adjustment of the ELM to be performed. This process is shown in Figure 3.32.

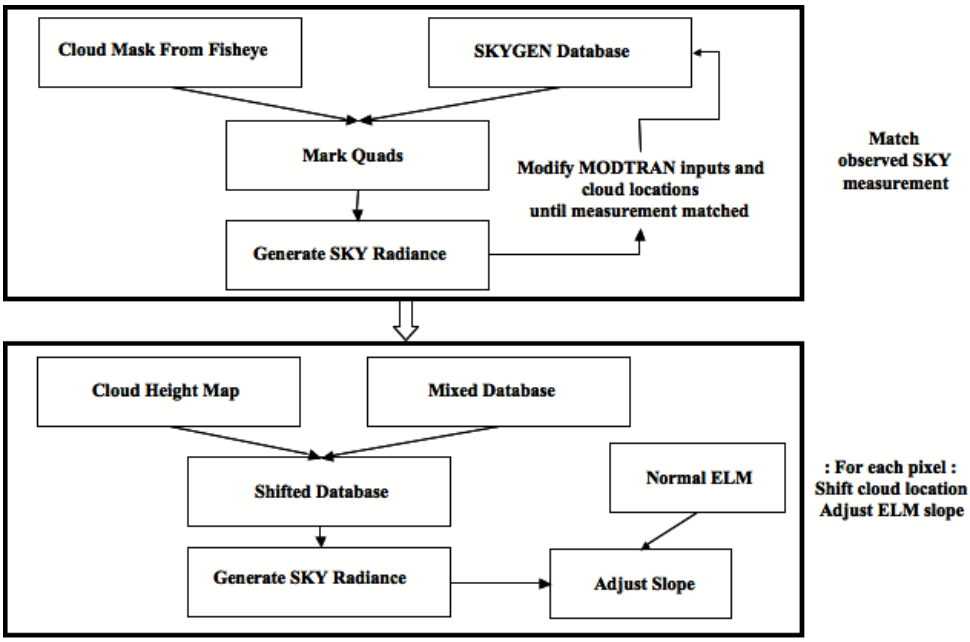

Figure 3.32: Process to apply adaptive ELM to real imagery.

In order to create a realistic radiometric model of the hemisphere, the location and types of all clouds present for each quad must be obtained. This can be accomplished through the use of a cloud mask algorithm like the one outlined in section 3.3.4. When working with real data, three sky types must be determined. The first type is blue sky which is found by comparing the blue and red channels of the image. The second type is a dark cloud which is transmitting incident sunlight. Both of these first two types of quad can be generated readily with MODTRAN. The third type of quad is a bright cloud in which sunlight is being scattered and reflected from the cloud itself. The process of generating this type of quad is outlined in section 3.3.3. These cloud types are

found by using a threshold that varies as a function of distance from the brightest area in the whole-sky image. The parameters for this threshold are interactively modified through the use of a GUI, shown in Figure 3.33.

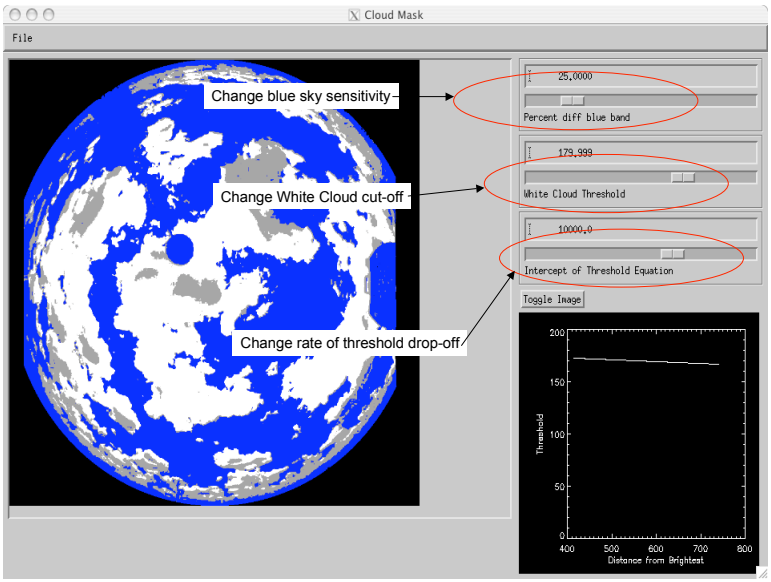

Figure 3.33: Graphical interface used to generate cloud mask.

Matching the SKY illumination was attempted using data from the MMC. The total irradiance was measured using the Ocean Optics spectrometer and calculated using the skygen software. It was then scaled into units of radiance for comparison, shown in Figure 3.34. The results indicate that a match should be possible with placement of clouds into the database, and with an instrument which is more sensitive in the short / long wavelengths.

Another approach to obtaining the downwelling radiance at remote locations is through measurement. If the directional downwelling field is measured directly at each site, the need for modeling is eliminated assuming that the measurement takes place at the same wavelengths as the image. The geometry could then simply be adjusted for each remote site and re-integrated. A device such as PARABOLA III could be used since it measures quads in a manner similar to that of the modeling approach. Figure 3.35 shows the device as well as its field of view projected into the hemisphere. This method will almost certainly be more accurate than modeling and certainly much

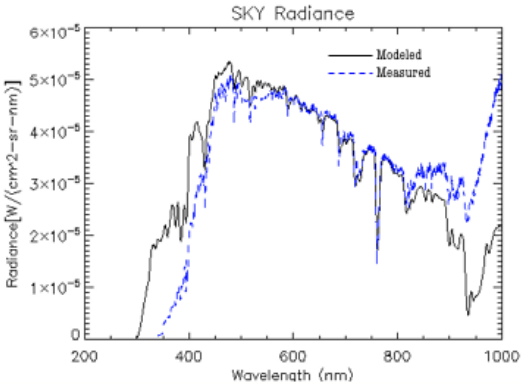

Figure 3.34: Modeled vs. measured total SKY radiance. Modeled radiance created using clear sky conditions, shown in black.

quicker. However, the equipment is much more expensive than what is required for a downwelling measurement that is not directional.

(a) The parabola instrument.

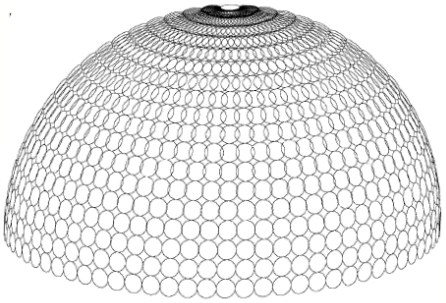

(b) The quads produced by projecting parabola's FOV into the sky.

Figure 3.35: The PARABOLO III instrument can be used to obtain directional downwelling terms, and was developed by the Jet Propulsion Laboratory [Bruegge et al., 2000].

3.3.7 Polynomial Theory

As discussed in the background, the use of a polynomial fit to produce the look up table for conversion between sensor recorded values and reflectance produced in highly scattering bands yields superior results compared to linear fits. To explore why this is, it is helpful to examine a mathematical model for sensor reaching radiance that will encompass the spherical albedo of the atmosphere. Equation 3.10 shows one way to express this relationship (wavelength dependence left out).

$$L_{sensor} = \frac{mr}{1 - \rho S} + L_u \tag{3.10}$$

where $m = \left(\frac{E_s \tau_1}{\pi} + L_d\right) \tau_2$. If it is assumed that $r = \rho$, this equation can be expanded out into series form and expressed as a polynomial, shown in equation 3.11.

$$\begin{aligned} L_{sensor} &= m[r + r^2 S + r^3 S^2 + ...] + L_u \\ L_{sensor} &\approx r^2 S m + rm + L_u = a_2 r^2 + a_1 r + a_0 \end{aligned} \tag{3.11}$$

Using this relationship now requires more than just two reflectance measurements at the calibration site. However, m can still be adjusted as before at remote sites using the same technique outlined in the linear theory section. The quad based downwelling model should provide more insight in determining a method to adapt the S parameter for areas away from the calibration area.

3.4 Requirements

The use of auxiliary measurements to enhance algorithms used with airborne imagery coincides with the goals of ISSI. One way of using ground based measurements to improve the inversion of imagery from sensor based units into reflectance units has been presented. This section will address what instrumentation would be useful to facilitate this improvement based on the experienced gained in the MMC. The computational requirements in order to process this data will also be discussed.

3.4.1 Instrumentation

The adaptive ELM will require at least one site which has been set up to provide for an accurate ELM. The site will therefore need to have the capability to measure the cloud conditions, the total irradiance, and have two areas of known low and high reflectance.

This was accomplished during the MMC by using a Nikon D50 with fisheye lens, an Ocean Optics USB 4000 to measure the irradiance, and an Analytical Spectral Devices (ASD) spectro-radiometer to measure two tarps of low and high reflectance. Other measurements that should be made if using MODTRAN to simulate the irradiance instead of measuring directional SKY irradiance should be atmospheric in nature. These can be used to decrease error in matching MODTRAN to the observed irradiance. GPS can be used to estimate total integrated perceived water, a radiosonde can be launched to obtain temperature, pressure, and relative humidity as a function of height. The visibility and aerosol content of the atmosphere would also be useful information.

The fisheye measurement using the D50 should be improved upon since not an entire hemisphere was captured due to lens stops present. The reflectance measurement using the ASD can also be problematic when working in cloudy conditions since the sequential method is used. A ratio method would be more practical to obtain calibration target reflectance.

As the distance from the calibration site increases, the viability of using the fisheye data for cloud location decreases. This means that the predictions for the SKY term will contain increasing amounts of error as well. A remote site should be able to solve this problem by making new fisheye and SKY measurements. The model can then be re-matched to the remote SKY measurement.

The most expensive required measurement is that of the SKY irradiance. Currently a USB 4000 spectrometer costs approximately $3500. However, if an ELM is being performed on an instrument with fewer bands such as RIT's WASP Lite sensor, the number of bands could be reduced. In fact, it is not a strict requirement that a large number of bands needs to be measured. Further work to study which bands are needed could show that only a few band-passes need be measured which could be coupled with a model to obtain the rest of the curve. If this is the case, cost would be significantly decreased.

One can imagine a network of fisheye and SKY measurements being made as an aircraft passes overhead automatically. This approach would provide for the speed that is needed to minimize variability in measurement due to cloud effects. The term 'sensor web' could be used to describe such a network and in this case would consist of one master node residing at the calibration site. Remote nodes would be placed around the calibration site at a spatial sampling interval which would be dictated by what is financially feasible. These nodes must be in communication with each other to allow for near simultaneous capture of data as the imaging platform acquires data. The nodes could also be able to communicate status information such as calibration and power.

3.4.2 Calibration

Each node making a radiometric measurement such as irradiance needs to be calibrated. This is essential since the data will be used to modify the calibration site information. One approach to this web-wide calibration is to transfer the calibration present at the calibration site from node to node. This could be accomplished on days where there is very high atmospheric homogeneity, so called 'severe-clear' days. Care must be taken to choose days in which variable signals are due to sensor drift and not to atmospheric variance. Figure 3.36 shows output from a hypothetical sensor network in which clear and cloudy days are shown. The output for each node is shown where in one case, sensor response is not taken into account, and in the other a cross-calibration is applied.

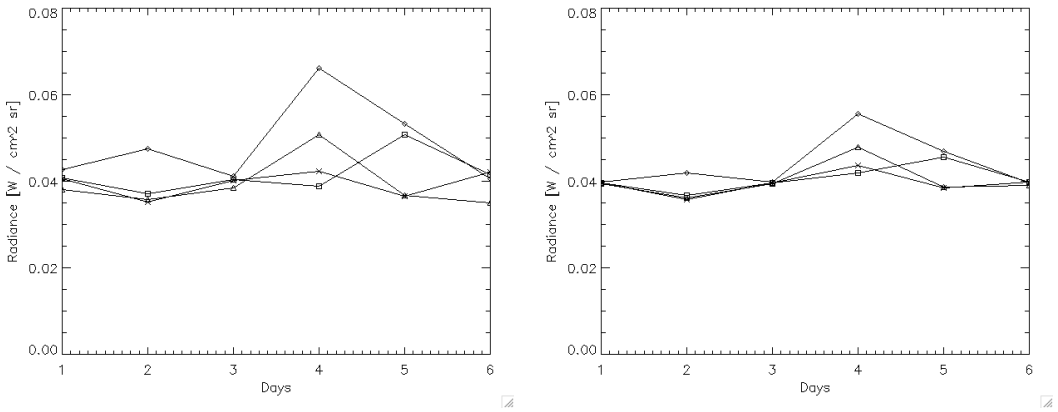

(a) No sensor cross-calibration. (b) Sensor cross-calibration applied.

Figure 3.36: Simulated data of a sensor web measuring SKY radiance. Each symbol represents a different node in web. Days one, three, and six represent clear days with no cloud cover. Days two, four, and five have clouds present in the atmosphere.

In addition, the data recorded at the node closest in spatial terms to the calibration site should be calibrated first which will further minimize spatial variability. This remote node can now be used to calibrate the next farthest node. As a node becomes farther away from the calibration site, it will have a larger chance of seeing a different signal than the calibration node. However, it will also be possible to combine calibrations from more nodes in the network, thus averaging out variability. This process is illustrated in Figure 3.37, which shows how node 1 only used one average since it is close to the calibration site while node 3 uses information from 3 nodes.

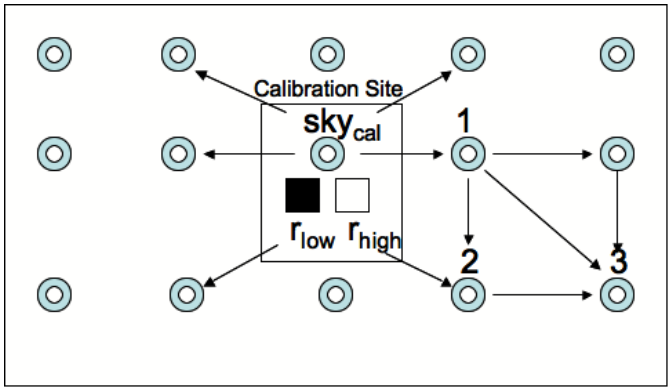

Figure 3.37: Each arrow indicates a calibration transfer. Different averaging strategies can be used to obtain higher accuracy.

3.4.3 Computational Requirements

When dealing with large amounts of auxiliary data during a collection, the main challenge for operators becomes timing. Since all measurements need to be made when the airborne imagery is being taken, it becomes non-trivial for people to operate the equipment quickly enough. The best solution for this problem would be to automate the system so that the data is organized and the equipment is operated automatically. With this said, processing the data also takes time. The largest computational burden in the adaptive ELM algorithm is the SKY database generation since it requires on the order of one thousand MODTRAN runs each taking a minimum of several minutes.

The DISORT algorithm within MODTRAN was used to account for multiple scatter. Multiple scatter becomes important when modeling an atmosphere with cloud cover. Figure 3.38 indicates how long running DISORT with different number of streams takes.

A higher number of streams will increase accuracy but lengthen run-time. The examples in section 3.3.5 were run with an 8-stream solution. The database generation is implemented using the condor system which distributes jobs across 60 machines in the CIS and 160 in computer science. This management system works well with many different types of platforms and can lead to an order of magnitude decrease in run time.

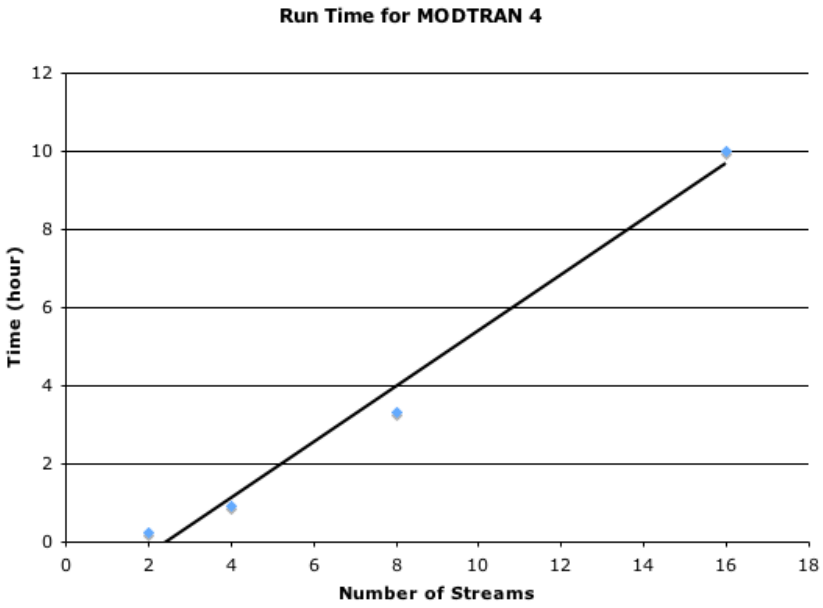

Figure 3.38: Run time for a single MODTRAN 4 run on a SUN Blade 1500 with different numbers of streams for DISORT.

Chapter 4

Validation

4.1 Overview

So far it has been shown that clouds do create spatial variability in the observed hemispherical radiance field. A method to correct for this variability has been developed which in theory should improve upon current ELM approaches. This chapter will delve into the details of how to implement the method using real data. The real data will be used to validate the approach, during which an observation leads to the development of a novel method to merge ground based measurement with modeled data.

This validation will use data which has limited spatial extent in its ground truth. In other words, the validation panels are close spatially to each other. However, the AELM can be also be applied to the same scene in which just the time has changed. Since the cloud field is in motion, each scene will therefore have a unique cloud configuration. As long as the sun movement is accounted for, the observed variability will be that which is generated by the cloud movement.

The validation will take three forms. First the variability between the two scenes will be corrected for using SKY measurements. Second, cloud masks for each scene are generated and the SKY terms are found using a three dimensional model. Last the spectral character of the model is changed using the measured SKY term from scene one. The results from each approach show that the AELM is an improvement over a traditional approach.

The algorithm is also validated with the spectral response of two different imaging systems. The data used is collected with the Hyperspectral Digital Imagery Collection Experiment (HYDICE) which is a hyperspectral sensing system which has a spectral range of approximately 400 - 2500nm[Basedow et al., 1995]. This data is then spectrally degraded using the sensor response function of a multi-spectral system called the

Wildfire Airborne Sensor Program Lite (WASP LT) which is currently in use by the Laboratory for Imaging Algorithms and Systems at the Rochester Institute of Technology.

4.2 Atmospheric Radiation Measurement (ARM) site

The validation data comes from a site located in Lamont, OK which is an ideal location for studying atmospheric effects. The site has a permanent infrastructure installed for collection of ground truth and is situated such that there are minimal background effects. Figure 4.1 shows the ground location of the tarps and the sky camera.

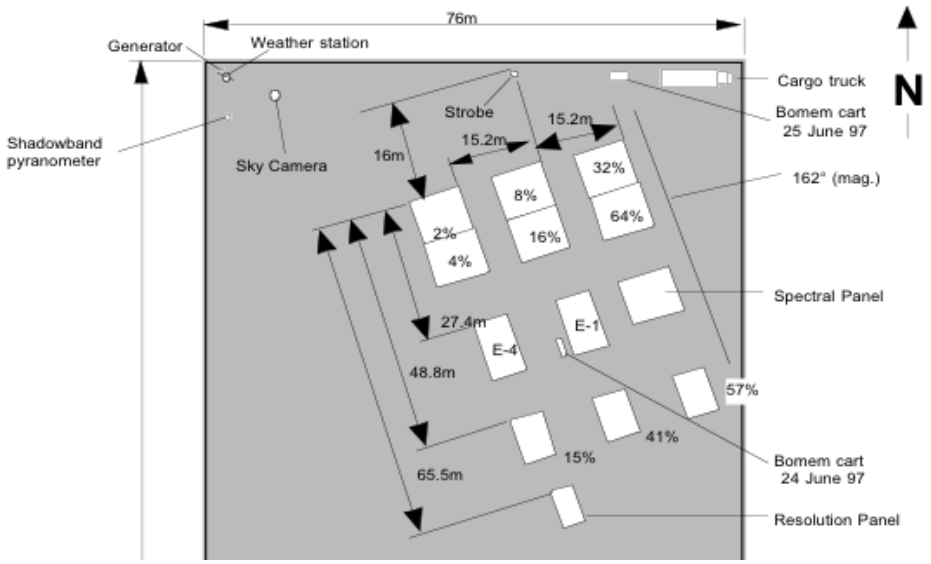

Figure 4.1: Layout of ground truth used in validation.[MTL, 1997]

The data collection was performed from June 24^{th} through the 26^{th} in 1997. The sensing system used to collect data was the Hyperspectral Digital Imagery Collection Experiment (HYDICE) which is a hyperspectral sensing system which has a spectral range of approximately 400 - 2500nm[Basedow et al., 1995]. Ground truth was also collected of the area shown in Figure 4.1 by MTL Systems, Inc. (MTL)

4.2.1 Ground Truth

Extensive ground truth was collected which took many different forms [MTL, 1997]. This research uses three measurements from the collection. The first is standard panel reflectance measured in a sequential fashion, which is described in section 2.2.2. The 2,4,32, and 64% panels are used in the first ELM while the 8 and 16% panels are used for validation. The second measurement used is the SKY term which was obtained by measurement of the reflective standard Spectralon© using a Geophysical Environmental Research Mark IV spectroradiometer (GER). The final measurement used was collected using the sky camera. This camera produced whole sky images showing cloud location / orientation. These were captured on film and then scanned to produce digital images.

4.2.2 Airborne Collection

The airborne asset used in this collect was the system HYDICE. It flew over the site several times at various altitudes and orientations. Three runs in particular where chosen for use as seen in table 4.1. The runs where chosen for several reasons. First, the amount of cloud cover in the sky was sufficient to produce significant variability in the radiance field. Second, the flying height of the aircraft was low enough to give several fully resolved pixels of the tarps at a good signal to noise ratio. Third, both the sky camera and the SKY measurements were made at a time which coincides very closely to the time in which the HYDICE imagery was collected. Finally, MODTRAN model parameters were developed which work well with atmospheric conditions present during the collect [Sanders, 1999]. Each run shows a slightly different view of the calibration

Table 4.1: Flight and Ground Truth Information

Flight Information			Time		
Run	Date	Altitude (ft)	Hyperspectral Imagery	Whole Sky Image	SKY Radiance
07	6/24/97	6075	12:26	12:30	12:27
10	6/24/97	6030	12:47	12:50	12:47
15	6/25/97	4956	1:56	2:00	1:58

site which can be seen in Figure 4.2.

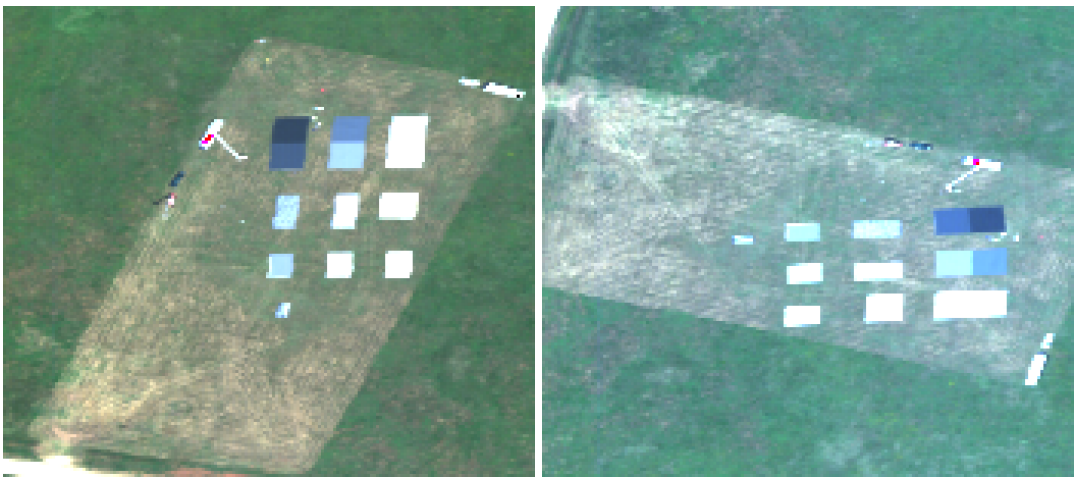

(a) run07 (b) run10

(c) run15

Figure 4.2: Calibration site from each flight-line. Atmospheric effects have not yet been accounted for.

4.3 Traditional ELM Results

The first step in validation is to perform a traditional ELM using the panel reflectance and imagery from run seven. The method outlined in section 2.1.1 was used. This will serve as the baseline to which compare each subsequent result too. Figure 4.3 shows the look up table for a few bands produced using the ELM.

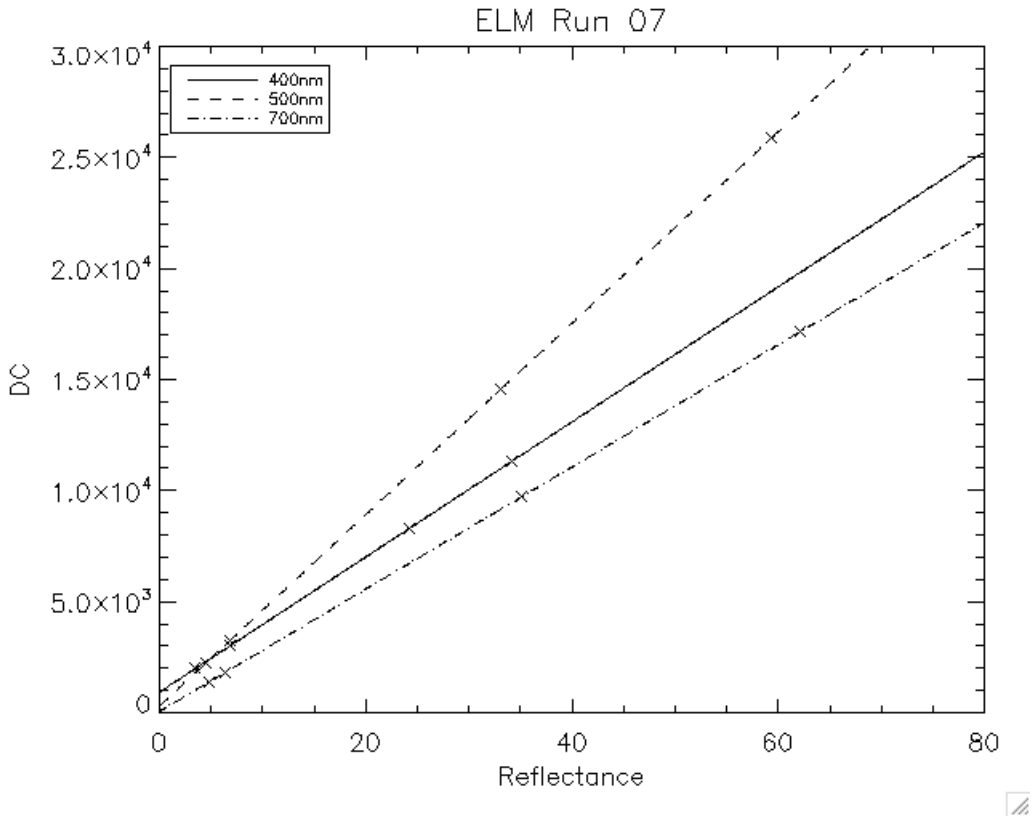

Figure 4.3: ELM for selected bands for run07. The 2,4,32, and 64% tarps were used to produce the linear fit, as indicated by the 'x'.

To assess the absolute accuracy of the ELM the retrieved reflectance from the eight and sixteen percent tarps, or the validation tarps, is compared to both the lab and field measured values. Figure 4.4 shows that the three measurements are all within a few reflectance units of error.

The rest of the validation will focus on correcting the run seven slope so that it will produce accurate reflectance retrieval when applied to scenes with differing atmospheric conditions. A different correction for both runs ten and fifteen will be gen-

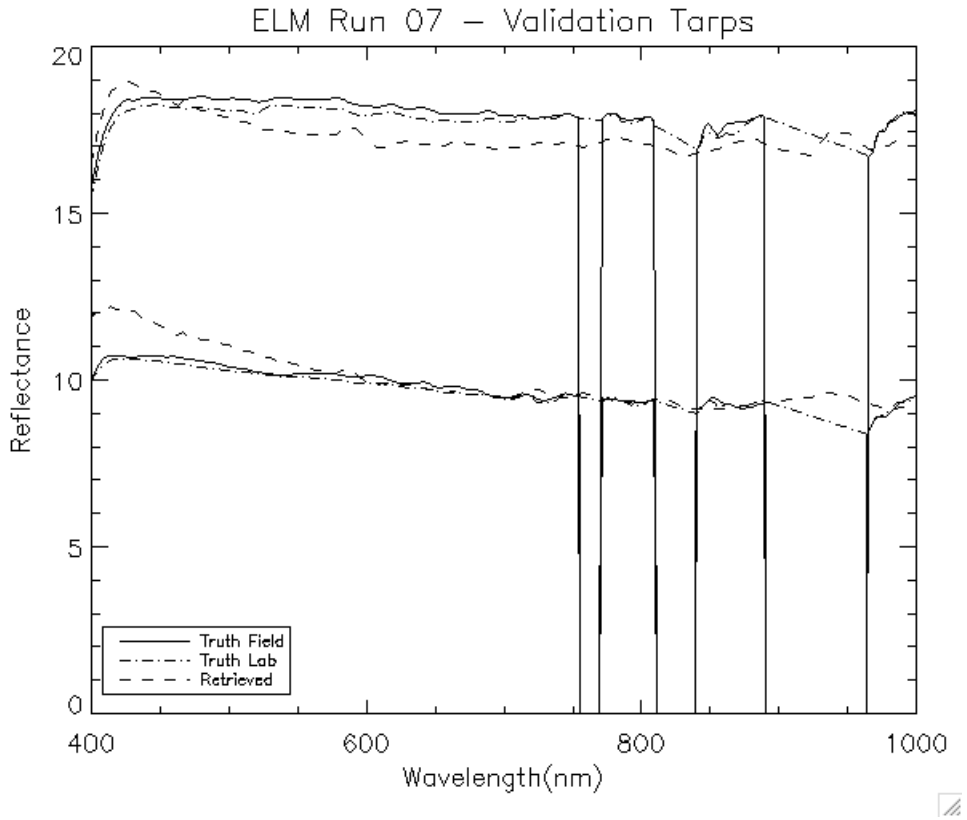

Figure 4.4: Comparison of retrieved reflectance for the eight and sixteen percent tarps to both field and lab ground measurement.

erated. The reflectance off of the two validation tarps will be compared to what was achieved in run seven.

4.4 Adaptive ELM with Variable Cloud Cover

4.4.1 Validation with Measurement and Model

The first method will use only measured SKY values to adjust the slope term which was generated using the run seven data. The slope is adjusted via a ratio of the SKY terms for run seven and run ten via equation 3.3. In this case however, $SKY_{remote} = SKY_{run10}$ and $SKY_{calSite} = SKY_{run07}$.

The second method is the same as the first with the notable exception of generating

the SKY terms using a radiometric model. The model is generated using a similar process to that outline in Figure 3.32. The fisheye image of the sky during the run is used to generate a cloud mask which has three categories: dark cloud, bright cloud, and blue sky. A simple polar projection is assumed since it is a common lens projection [Herbert, 1987], and no lens calibration data is available. In ordered to generate the mask the blue sky was identified by comparing the difference between blue and red channels. For pixels which were not blue (and therefore cloud), a threshold was set to determine if the pixel was a dark or a bright cloud. Since the magnitude of the cloud decreases as the angle away from the sun increases a variable threshold was created based on a pixels distance from the sun. The amount of variation in the threshold was controlled manually and a visual comparison was made to assess the quality of the mask. Figure 4.5 shows the GUI used to generate a mask.

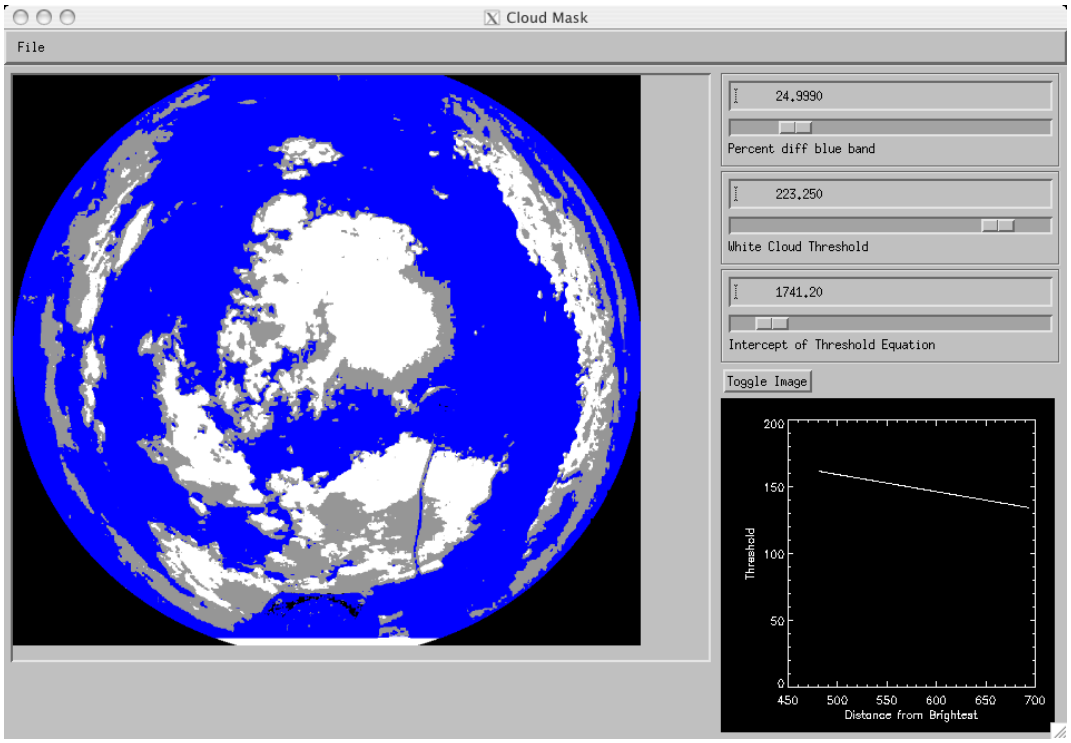

Figure 4.5: Cloud mask generation utility. 'Percent diff blue band' controls the process of finding blue sky. 'White Cloud Threshold' controls the y-intercept of the variable threshold. 'Intercept of Threshold Equation' controls the x-intercept of the threshold. 'Toggle Image' allows for the user to easily compare the cloud mask to the original image.

Once the mask is created, the sky image is broken up into groupings of pixels

termed 'quads'. The radiative transfer model MODTRAN is run for each quad with a path which propagates from the ground into space, and points at the center of the quad. Three databases are generated, one for blue sky and two for dark and bright clouds. A final database is generated containing a mix of all three with, the mix being controlled by the cloud mask.

The cloud mask and mixed database results for runs seven and ten are shown in Figure 4.6 and Figure 4.7.

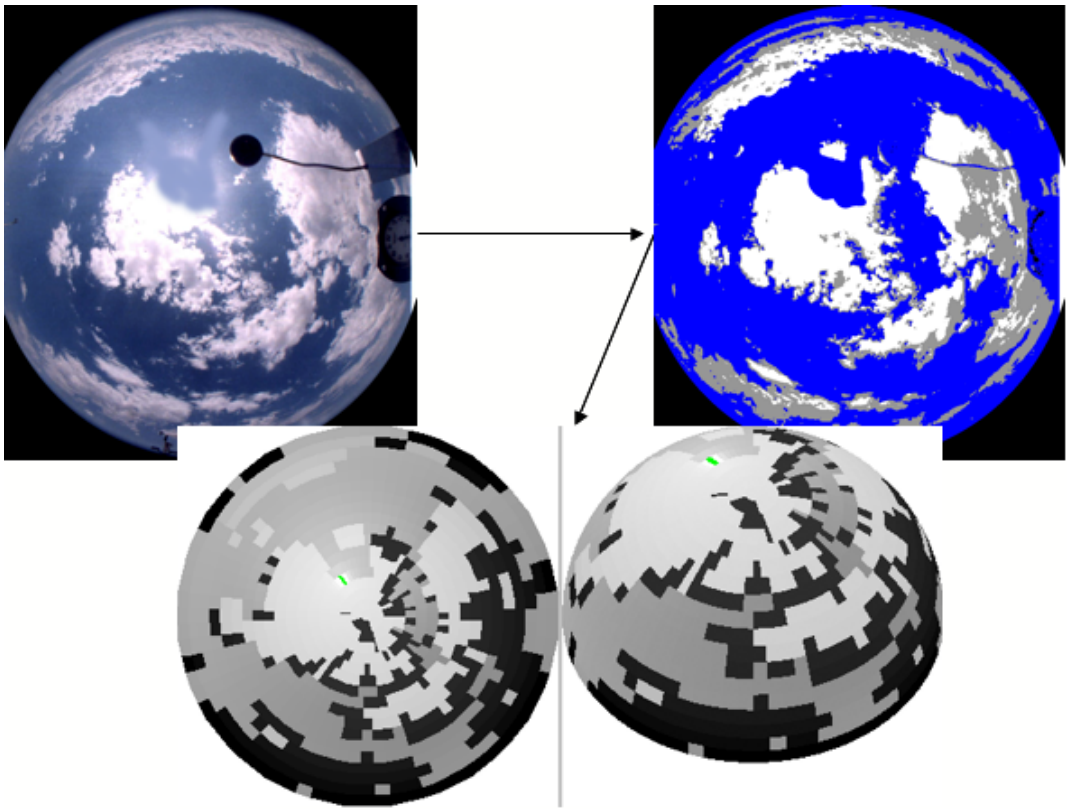

Figure 4.6: Run seven modeling process using 1224 quads. The sun blocker in the original image was not operating correctly, so the sun glint is manually airbrushed out.

Finally, the sky term is calculated by integrating the final mixed database via equation 4.1.

$$SKY = E_{direct} + \sum_{i=0}^{N} \sum_{j=0}^{M} L_{d\lambda}(i,j) cos\sigma_{[i,j]} sin\sigma_{[i,j]} \triangle\sigma \triangle\phi \tag{4.1}$$

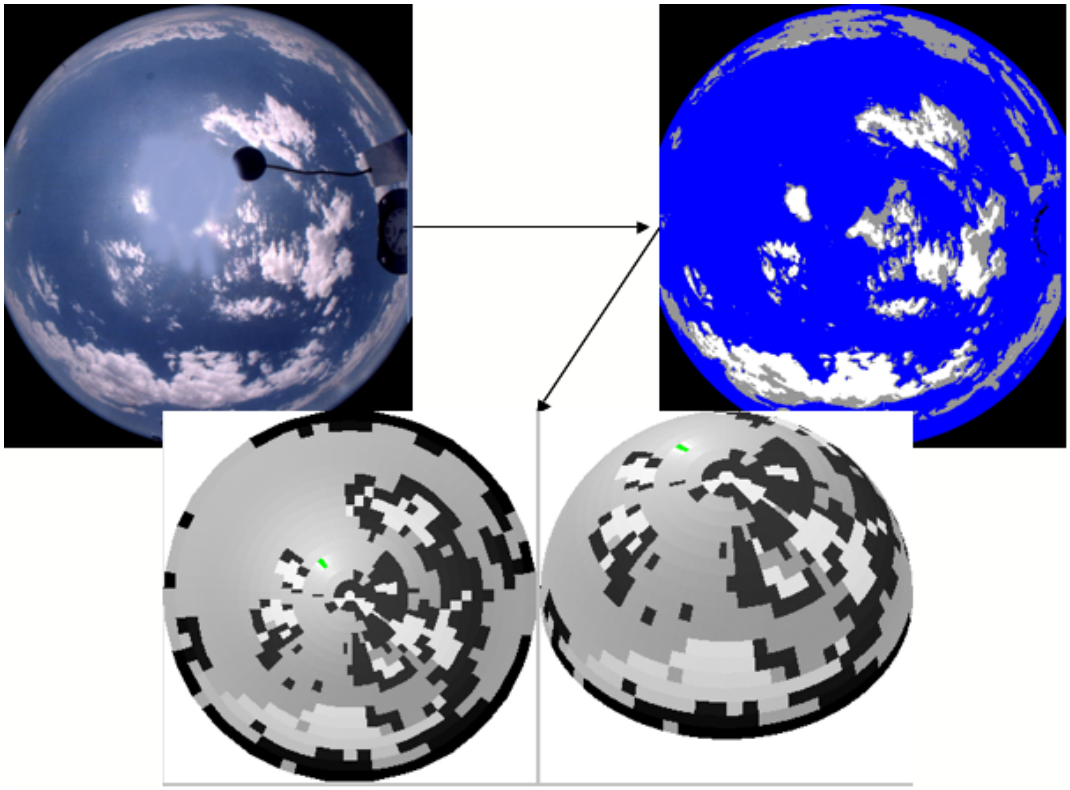

Figure 4.7: Run ten modeling process using 1224 quads.

where m and n are the total number of quads in the azimuth and zenith respectively.

The radiance produced from the modeling process can then be compared to the radiance observed from the SKY measurement. This is shown in Figure 4.8.

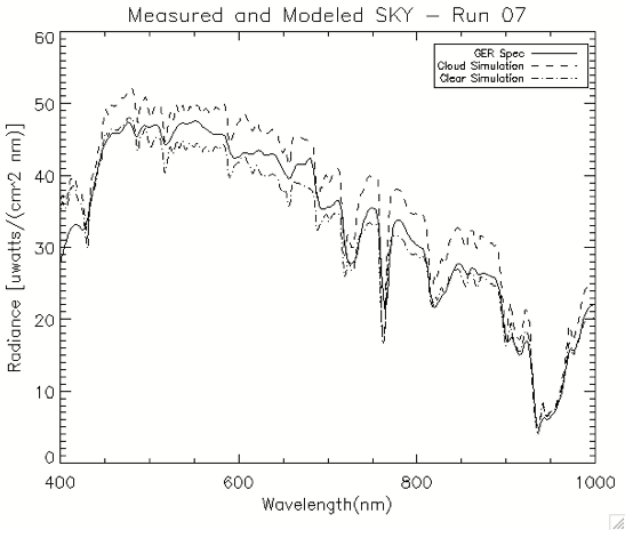

(a) run07

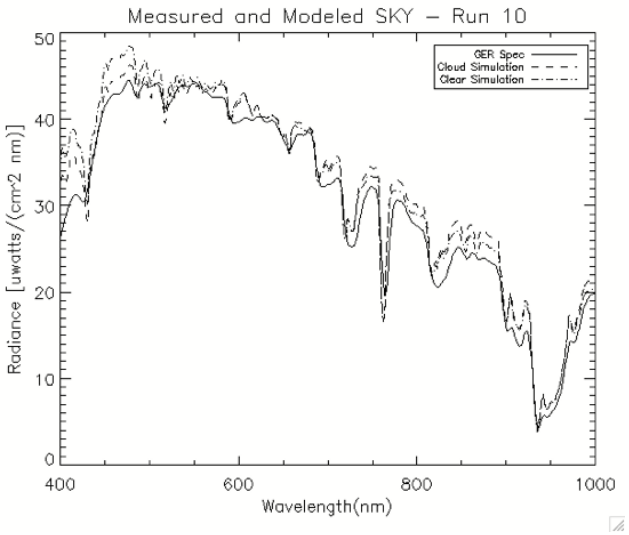

(b) run10

Figure 4.8: Absolute radiance comparison between measured and modeled sky values.

In the run seven comparison the clear sky model is lower in magnitude than the measured results. This makes intuitive sense since there is bright cloud cover in the sky. Though the modeled SKY term over-estimates the observed value this problem will be solved since the correction is a ratio. The magnitude error will therefore cancel and not be an issue as shown later. The run ten comparison shows that both the models are much closer to the actual observed radiance. This also makes intuitive sense since there are fewer clouds at that time.

It is also useful to visualize the SKY ratio term which will do the work of adjusting the run seven slope term. Figure 4.9 shows this ratio for the measurement and the clear and cloudy models.

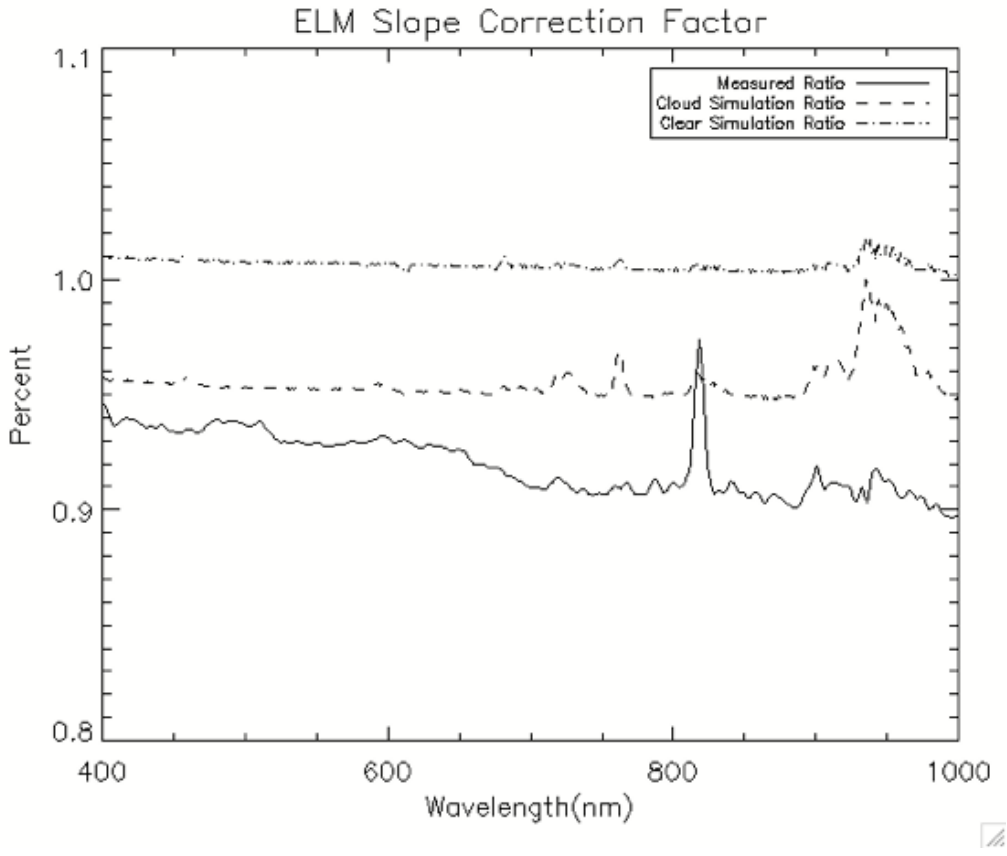

Figure 4.9: Correction ratio produced using different SKY values.

An important consideration is that of the sun location. Since each run is taken at a different time, the sun will move. Examination of equation 2.3 indicates that the

change in solar energy, assuming that τ_1 does not change significantly, will be the ratio of the cosine of the solar declination angle. Table 4.2 shows the solar angles and percent error expected for each of the runs.

Table 4.2: Change in Solar Energy

Run	Time	Solar Declination (σ)	$cos\sigma$	Percent Change
07	12:26	21.11°	0.93	
10	12:47	19.10°	0.95	1.23
15	1:56	13.27°	0.97	4.16

Figure 4.9 clearly shows that the model is taking into account this change since there is a bias of approximately 1.2 percent in the clear sky model. This means that we are not just observing the cosine effect, but that the illumination change is being dominated by the shifting cloud field. The cloudy sky ratio is clearly not the same as the measured ratio which means that it will produce different reflectance retrieval results than that of the measured ratio.

In order to compare the performance of both methods of correction, the retrieved reflectance for each tarp is expressed in percent difference from the retrieved reflectance obtained in run seven. The difference is found using equation 4.2.

$$normalized\ percent = \frac{|r_{07} - r_{10}|}{r_{07}} \cdot 100 \tag{4.2}$$

Figure 4.10 shows this percent difference for the two methods as well as the difference if the ratio is not used on the slope.

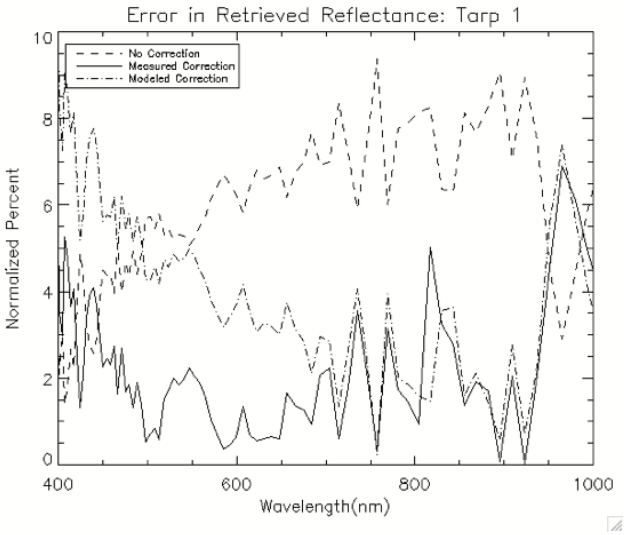

(a) Tarp 1 (8% tarp)

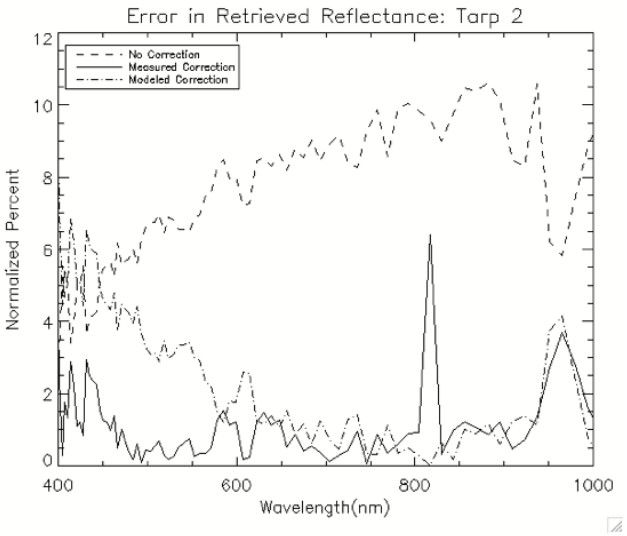

(b) Tarp 2 (16% tarp)

Figure 4.10: Percent error between retrieved reflectance for run seven and run ten .

Both validation tarps indicate that using the measured correction will produce significant improvement over using no correction. However, the model results do not always yield better results in wavelengths below 600nm. A larger error in the lower wavelengths make sense since Rayleigh scattering has an inverse dependence with the wavelength raised to the fourth power. This means as the wavelength decreases the amount of scattering increases [Schott, 1997]. This will put more pressure on the multiple scattering algorithm present in MODTRAN to perform accurately. Even if the multiple scatter algorithm performs perfectly there will be error in the atmospheric inputs to the model which explains this low wavelength error increase. As a test to see if the model can perform better, the area around the sun in run ten was examined closer and the airbrushed region was modified to allow for more cloud cover close to the sun. Figure 4.11 shows the results on the cloud mask and sky model of this change.

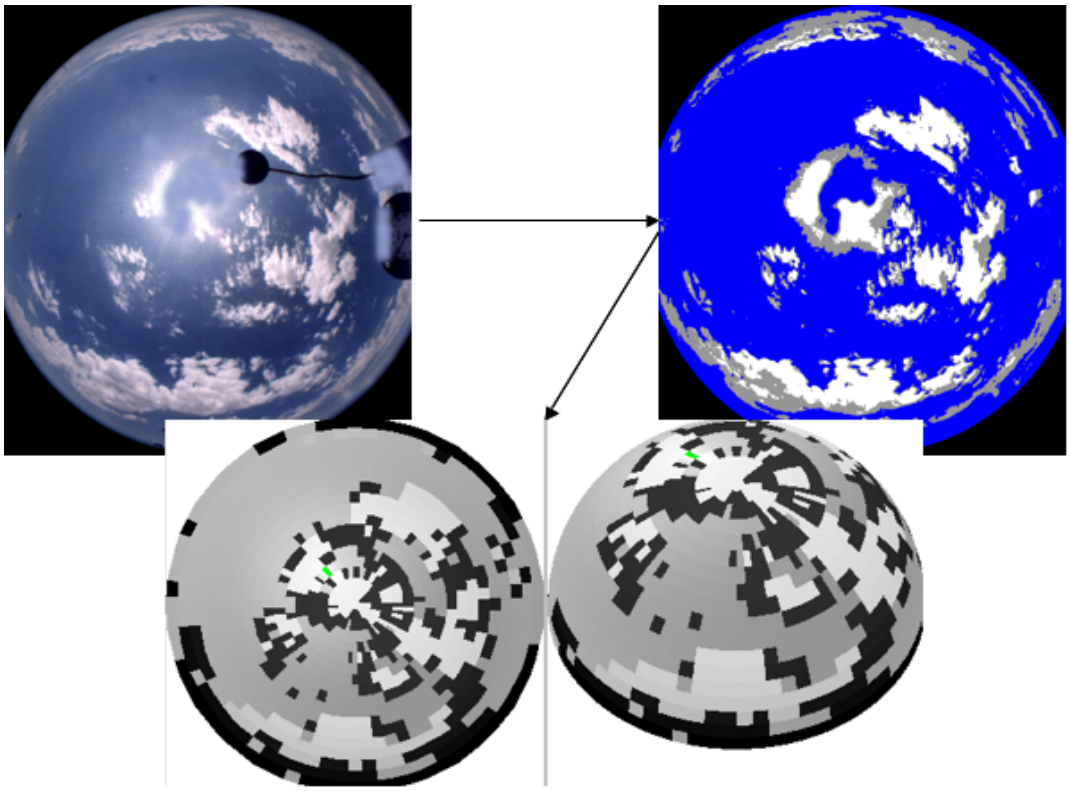

Figure 4.11: Run ten modeling process using 1224 quads. The airbrushed area around the sun is slightly decreased in size.

The new configuration produced a surprisingly large change in the ratio term. This indicates that it is critical to get the cloud cover correct in the area directly surrounding

the sun. This makes intuitive sense since the area directly around the sun contains the largest concentration of energy in the sky. Figure 4.12 shows how the modeled ratio created using the new configuration is now much closer to the measured ratio.

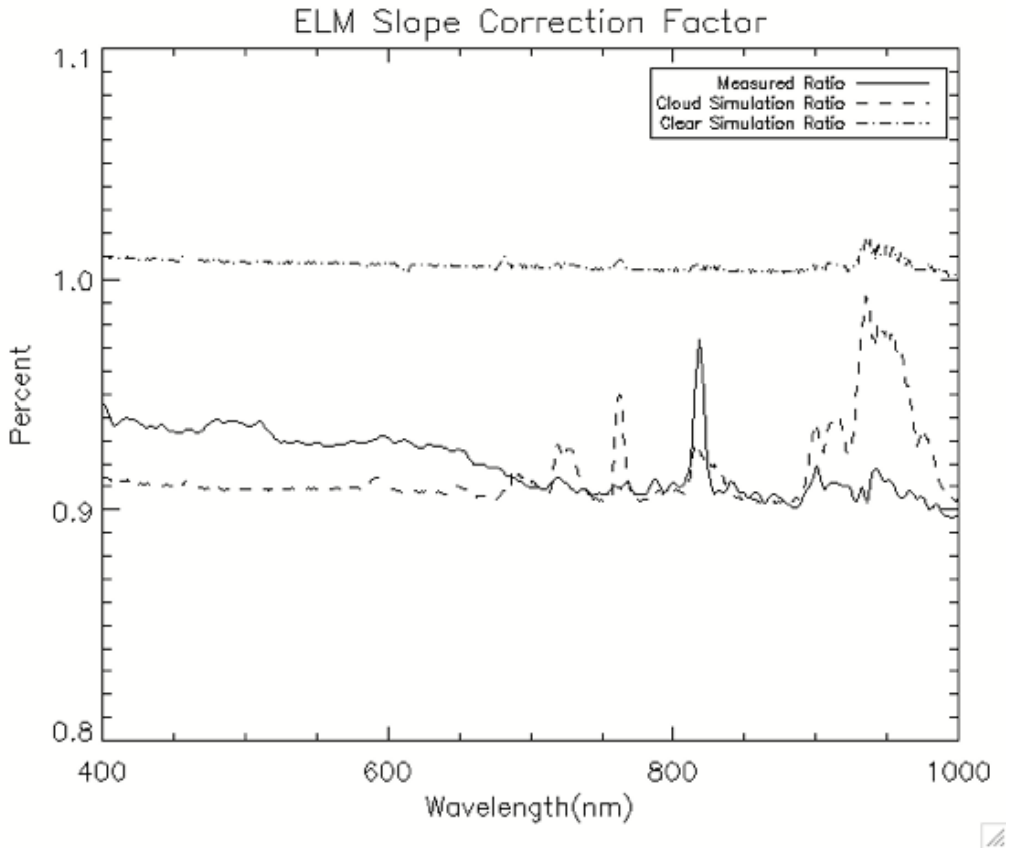

Figure 4.12: Correction ratio produced using new cloud mask for run ten.

The percent difference to run seven is recalculated and compared to the error which was present when using the first cloud mask. Figure 4.13 shows that there is an improvement in the region below 600nm. This indicates that adding in more clouds in that region has helped model the scattering effects more accurately. It is also seen that the model does not operate well in some of the longer wavelength such as around 940nm which will be discussed later.

Even with this change, there is still room to improve the model spectrally. The next section will outline one way to merge the measured data with the modeled to correct for the spectral error.

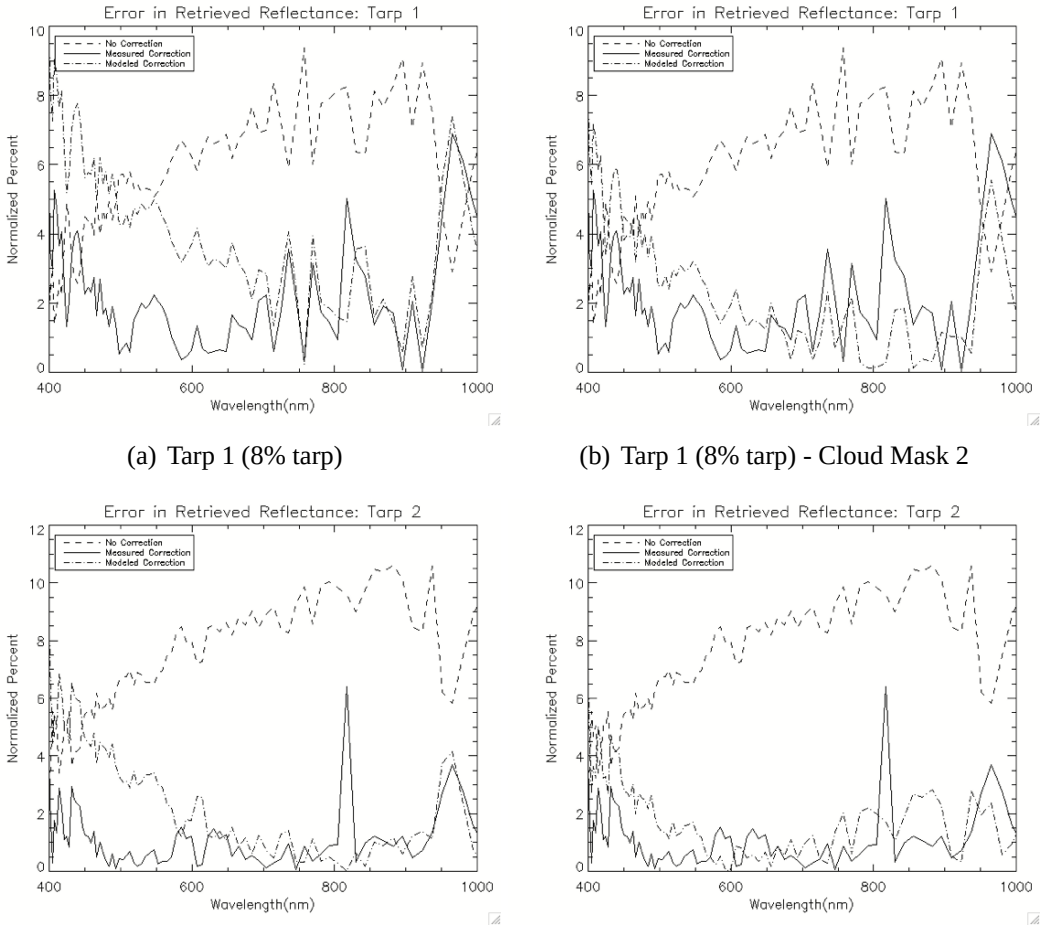

(a) Tarp 1 (8% tarp)

(b) Tarp 1 (8% tarp) - Cloud Mask 2

(c) Tarp 2 (16% tarp)

(d) Tarp 2 (16% tarp) - Cloud Mask 2

Figure 4.13: Percent error between retrieved reflectance for run seven and run ten after changing the airbrushed region in the sky image.

4.4.2 Hybrid Validation

In order to understand the structure of the spectral difference between the model and the measurement a way to compare the two is needed. One way to accomplish this is to euclidean normalized each measurement and each model using equation 3.1. Figure 4.14 shows the results of this normalization.

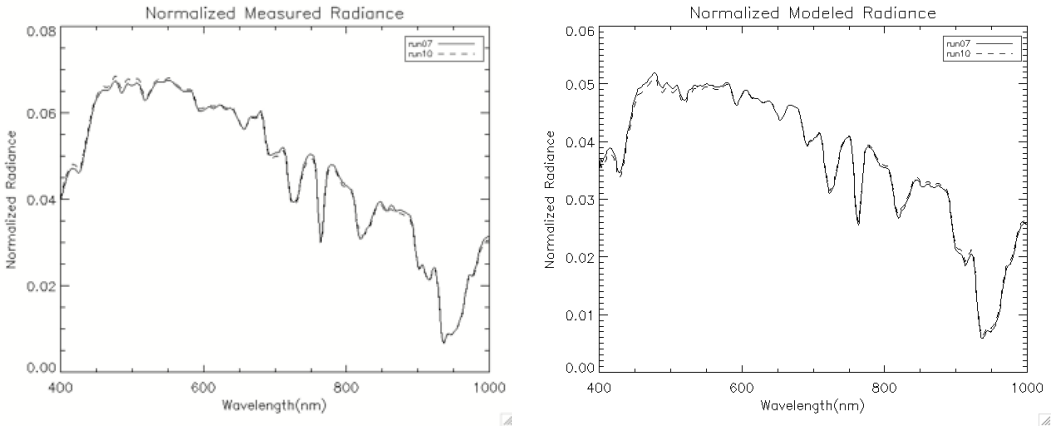

(a) Measurement (b) Model

Figure 4.14: Euclidean normalization of measurement and model SKY values for both run seven and run ten.

Since it is hard to see the spectral change in detail Figure 4.15 was created which shows the percent change between run seven and run ten. This shows that the measurement has significant spectral character in the wavelengths lower than 600nm which is lacking in the model. It is also seen that the model does not spectrally match the measurement in molecular absorption regions such as in the 940nm water absorption band. This again shows how the uncertainty in model inputs such as water vapor amount can lead to errors, which were seen near 900nm in Figure 4.13.

The first step in using the measurement to correct the model is to form a simple correction factor with the first scene for the model which can then be applied to subsequent scenes. However since the correction process relies on a ratio, a simple factor will cancel as shown in the following development.

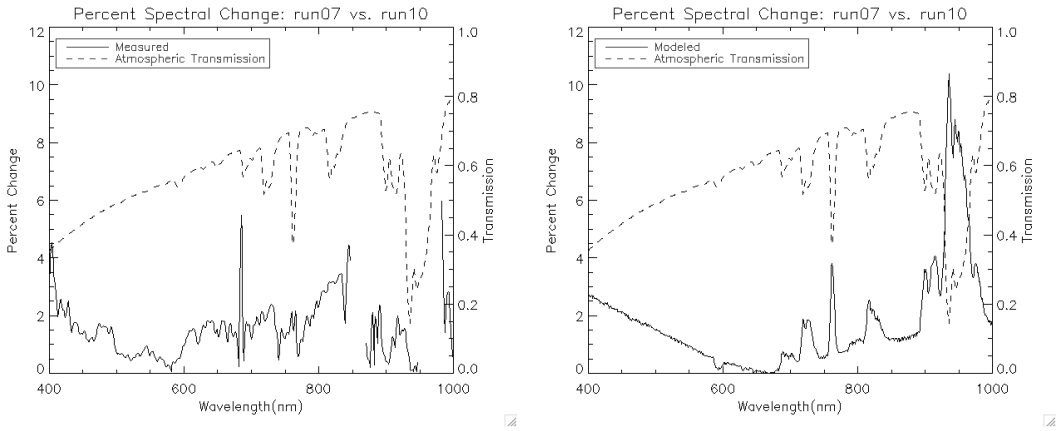

(a) Measurement (b) Model

Figure 4.15: Percent change of run ten relative to run seven. Atmospheric transmission generated by MODTRAN is also plotted for reference.

$$SKY_{mea} = SKY_{mod}\alpha$$

where α is the model correction constant.

Site 1 (in this case time one)

$$k = \frac{m_{t_1}\pi}{SKY_{t_1,mea}}$$

Site 2 (in this case time two)

$$m_{t_2} = \frac{SKY_{t_2,Mod}\alpha k}{\pi}$$

subbing in k

$$m_{t_2} = \frac{SKY_{t_2,Mod}\alpha}{SKY_{t_1,mod}\alpha}m_{t_1}$$

$$m_{t_2} = \frac{SKY_{t_2,Mod}}{SKY_{t_1,mod}}m_{t_1}$$

This method will not work because it changes both SKY measurements in the same way. One way to address the spectral errors without causing a cancellation is to change

the ratio directly. If both the SKY measurement and the SKY model are in the same units, then they can both be peak normalized and compared. The absolute difference between the values can then be used as an additive spectral correction factor. This process is illustrated mathematically below.

$$Ratio_{se} = \frac{SKY_{t_1,Mod}}{SKY_{t_2,Mea}} \tag{4.3}$$

where $Ratio_{se}$ is the value containing spectral error which needs to be accounted for.

$$\Delta = \frac{SKY_{t_1,Mea}}{max(SKY_{t_1,Mea})} - \frac{SKY_{t_1,Mod}}{max(SKY_{t_1,Mod})} \tag{4.4}$$

where Δ will be used as the additive spectral correction factor.

$$Ratio_{corrected} = Ratio_{se} + \Delta \tag{4.5}$$

where $Ratio_{corrected}$ now has the spectral error removed.

Figure 4.16 shows the peak normalized SKY values which do show spectral differences. One trend which is seen in the comparison is that the measurement is on average above the model up until around 700nm when a switch occurs and the model then jumps above the measurement. This behavior will be seen in more detail when the spectral correction delta is formed.

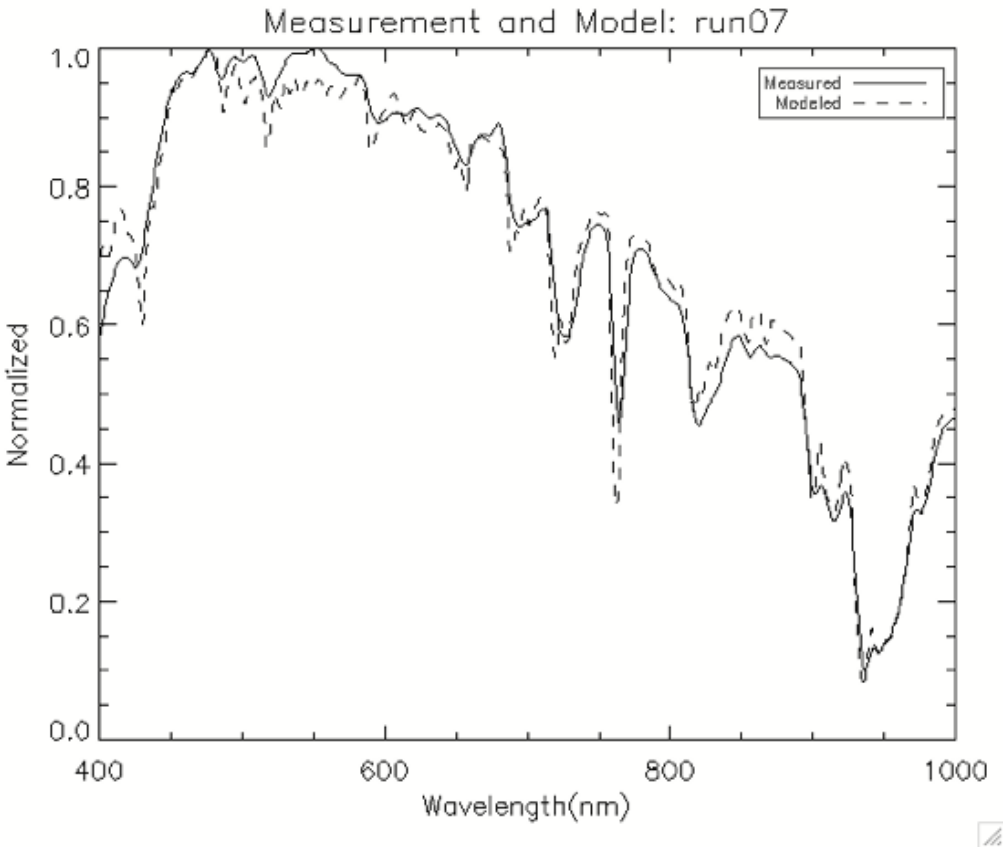

Figure 4.16: Peak normalized SKY values for run seven.

Next the spectral correction delta is formed by subtracting the two peak normalized curves, shown in Figure 4.17. Subtraction of the two peak normalized SKY terms yields a very noisy signal. This makes sense since most of the spectral change is very small in magnitude compared with the overall signal. Since most of the signal is removed to find this change, the noise present is exposed. As mentioned before, the measurement and model switch relative to each other which lends well to a polynomial fit. Since the spectral response of silicon tends to decrease rapildy below 500nm the fit was restricted to higher wavelengths.

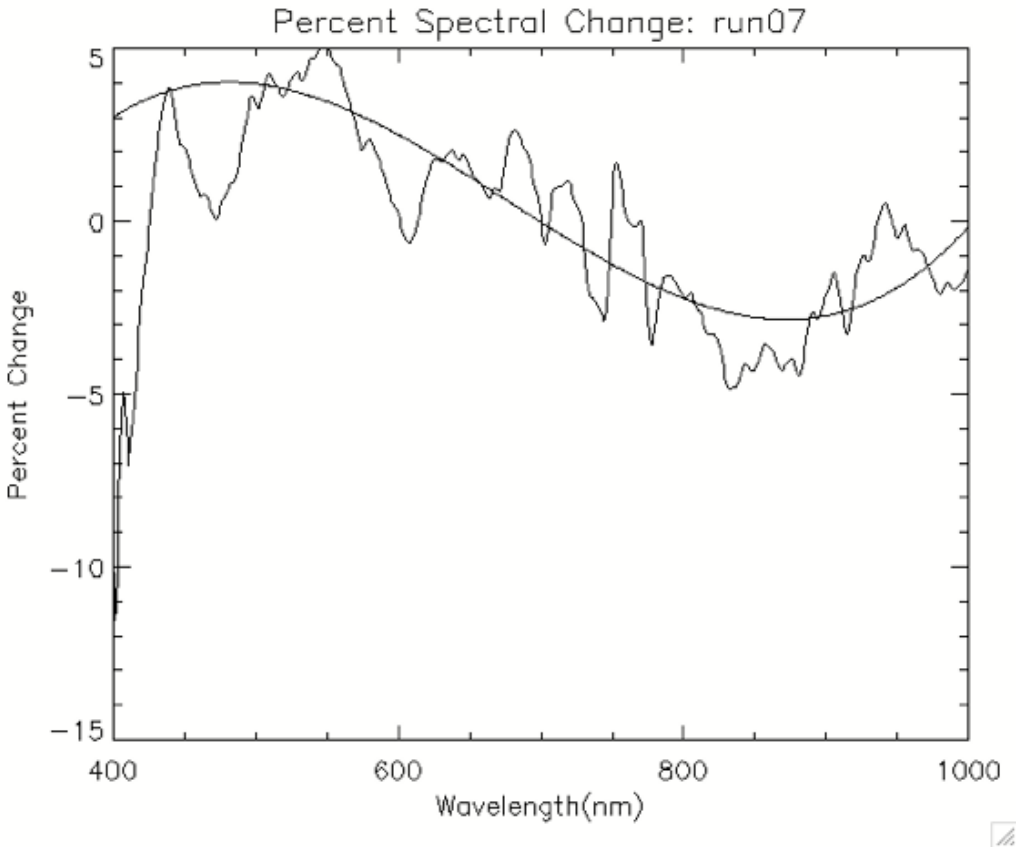

Figure 4.17: Spectral delta for ratio correction. A polynomial fit is performed and plotted over the data.

Now that the spectral delta is fitted it can be applied to the ratio which is shown in Figure 4.18. Inspection of the ratio leads to the speculation that the corrected ratio should yield better results in the highly scattering regions of the spectrum.

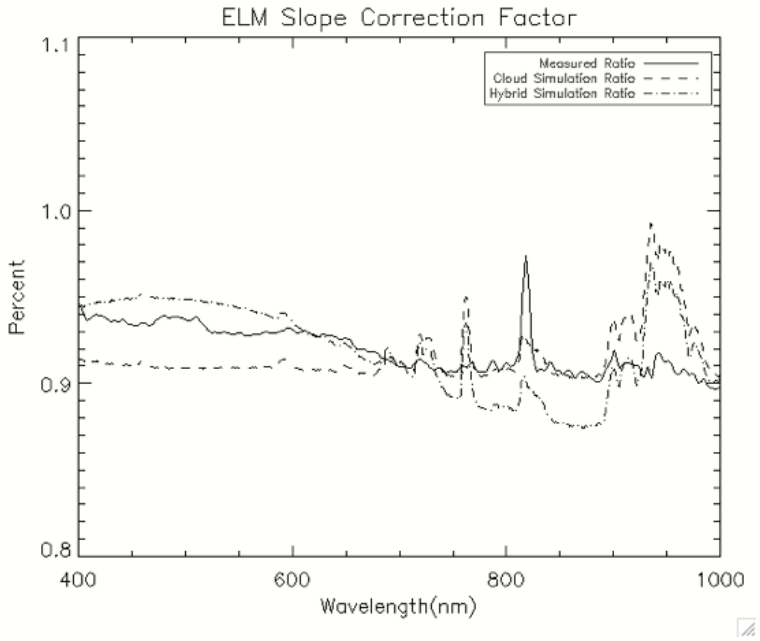

Figure 4.18: Result of applying fitted additive spectral correction to the ratio.

Figure 4.19 shows the percent error for the retrieved reflectance. The improvement in the blue is most apparent which indicates that using the measurement does help correct for scattering events. This makes sense since scattering tends to have a smooth spectral effect and the correction delta has been smoothed using the polynomial fit. However, using the spectral differences between the measurement and model in this case may not yield a significant improvement in all bands. This is most apparent in the region around the 940nm water vapor absorption feature.

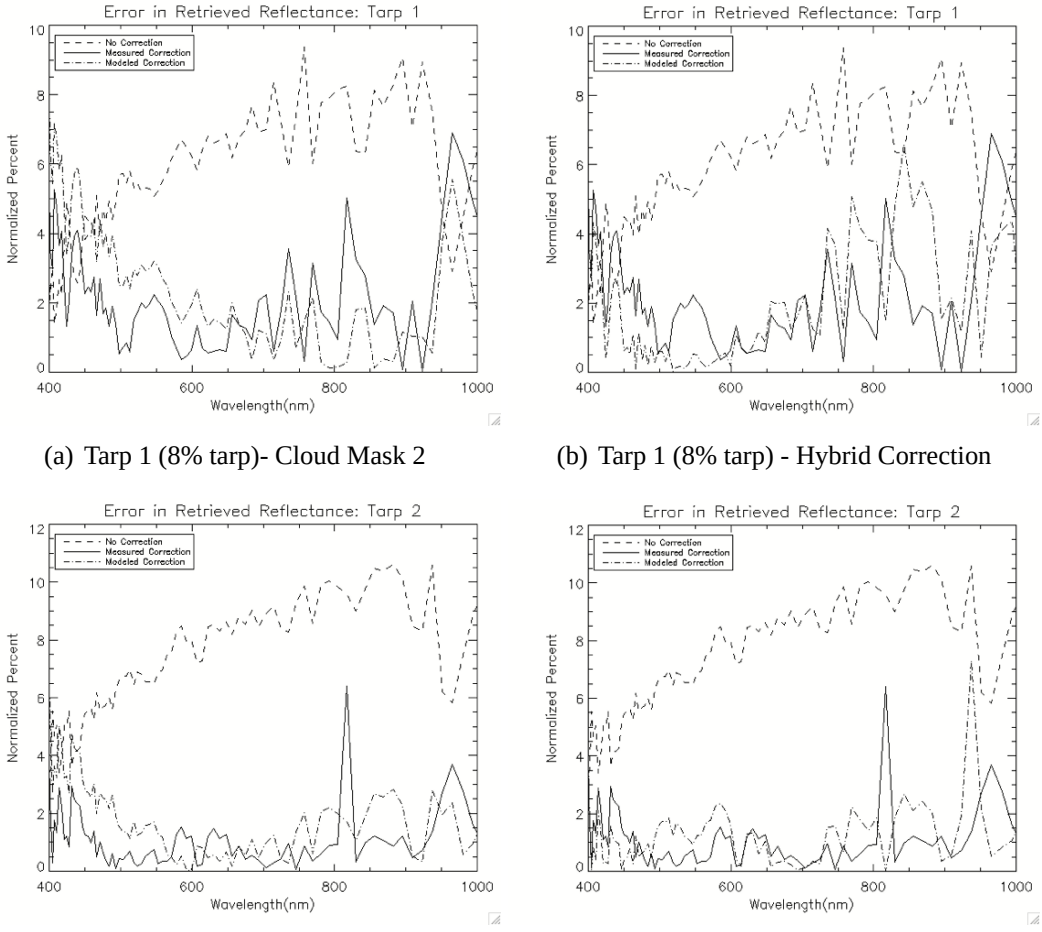

(a) Tarp 1 (8% tarp)- Cloud Mask 2

(b) Tarp 1 (8% tarp) - Hybrid Correction

(c) Tarp 2 (16% tarp) - Cloud Mask 2

(d) Tarp 2 (16% tarp) - Hybrid Correction

Figure 4.19: Percent error between retrieved reflectance for run seven and run ten. Results from of both pre and post hybrid correction shown.

Since the correction being applied is an additive correction factor, this leads to the observation that it is essentially a correction for the path radiance. This is because the path radiance is the additive term in the governing equation used for sensor reaching radiance. The AELM algorithm assumes that the path radiance does not change. To see if this assumption may be the source of the residual error the path radiance for both run 07 and run 10 was found using the a traditional ELM approach for each run. The path radiance is then simply the intercept in the linear regression. Figure 4.20 shows that the path radiance for each run is in fact not the same.

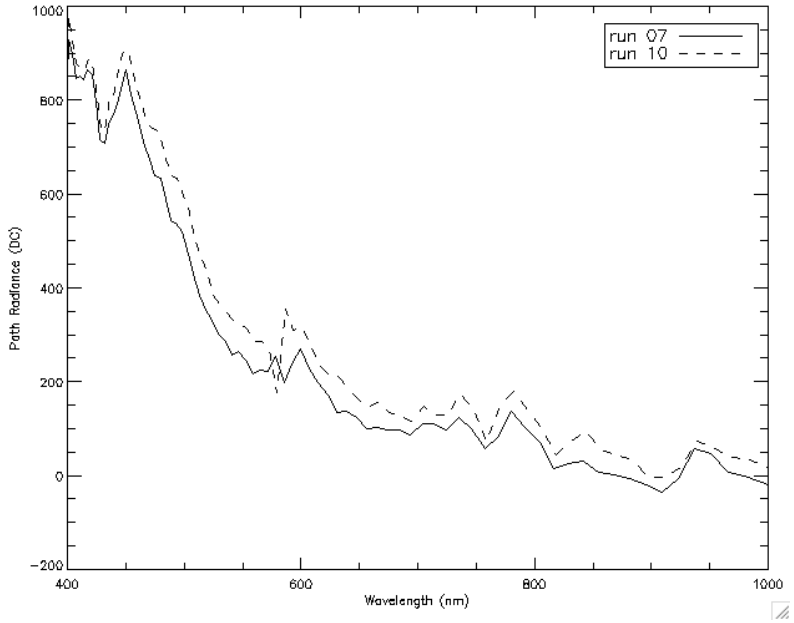

Figure 4.20: Path radiance from ground to sensor in sensor digital counts.

The percent change between the path radiance for run 07 and the path radiance for run 10 is compared to the residual error for the AELM in Figure 4.21. This comparison shows that the source of the residual error is in large part driven by the change in path radiance. This change is also seen while implementing AELM in cloud shadow and is explored in more detail in section 4.5.

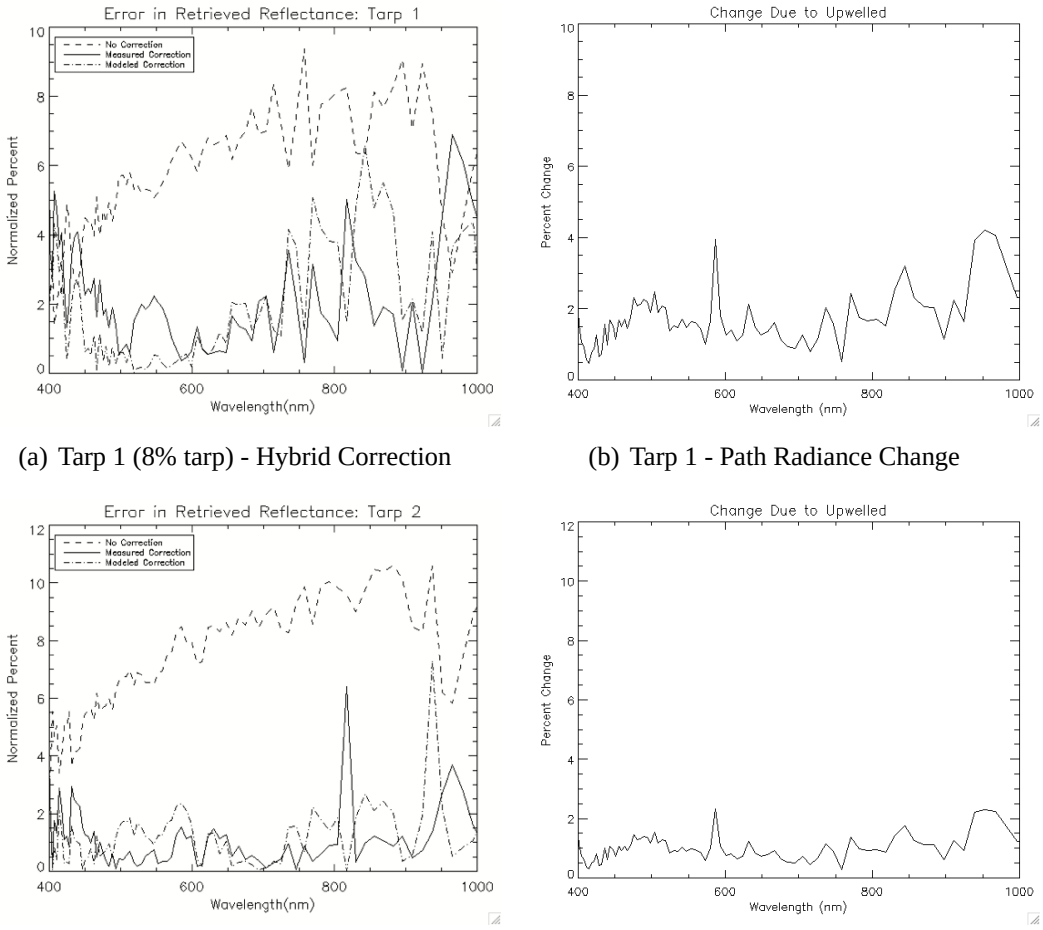

(a) Tarp 1 (8% tarp) - Hybrid Correction

(b) Tarp 1 - Path Radiance Change

(c) Tarp 2 (16% tarp) - Hybrid Correction

(d) Tarp 2 -Path Radiance Change

Figure 4.21: Residual error left from Hybrid correction seen compared to percent difference in path radiance.

While it is clear that the adaptive elm approach works in the run seven and run ten cloud scenarios, it is important to see how it will perform under different conditions. The next section will tackle a scenario which is the worst case for atmospheric correction. This is when the calibration area is under direct sun and the site of interest is under cloud shadow.

4.5 Adaptive ELM with Cloud Shadow

4.5.1 Validation with Measurement and Model

The approach in this case will follow the same path as that of section 4.4 with the exception that the site is now under a cloud shadow. Run fifteen is used since it is at approximately the same flying height and has the validation tarp area under cloud shadow. Run fifteen was taken on the following day after run seven at a significantly later time of day. Using run fifteen will test several things about the algorithm. First, it will test the algorithms ability to adjust the SKY term when the term has undergone much higher levels of change due to the sun being blocked. Second, since atmospheric parameters tend to change over the period of a day, it will test the sensitivity of the model to having correct atmospheric inputs. Finally, both τ_2 and L_u will be slightly different due to the change in flying height and atmospheric conditions.

Again the first step is to generate the model of the SKY term. The cloud mask and mixed database results for run fifteen are shown in Figure 4.22

The radiance produced from the modeling process can then be compared to the radiance observed from the SKY measurement. This is shown in Figure 4.23 which indicates that the SKY values in this case are now less than half that which was tested in run ten.

The slope correction ratio produced by using run seven and run fifteen is shown in Figure 4.24. In this case, there is a significant difference between the measurement and the model. This was anticipated since the inputs into the model are not known as well. However, there is also less signal for the measurement in run fifteen which could mean that it is also incorrect.

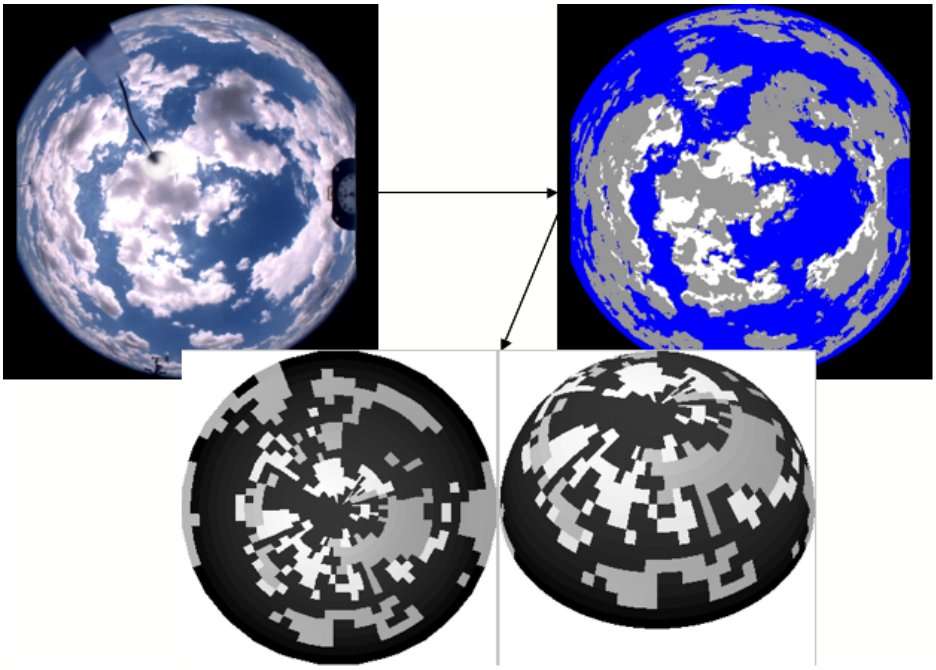

Figure 4.22: Run fifteen modeling process using 1224 quads. The sun blocker is now properly placed although the amount of cloud cover is greatly increased compared to that of runs seven and ten.

In order to see if the measurement or the model performed better, the error was produced and is shown in Figure 4.25. Compared to the best correction achieved using the Hybrid method on run ten data, the run fifteen correction has performed much worse in the lower wavelengths. However the relative improvement is much better, being at most 10% in run ten while being 70% in run fifteen. The effects of noise in the measurement are now more apparent since the unmodified model actually outperforms the measurement over a majority of the spectrum. For this reason, a Hybrid correction will not result in an improvement in this case and was not applied.

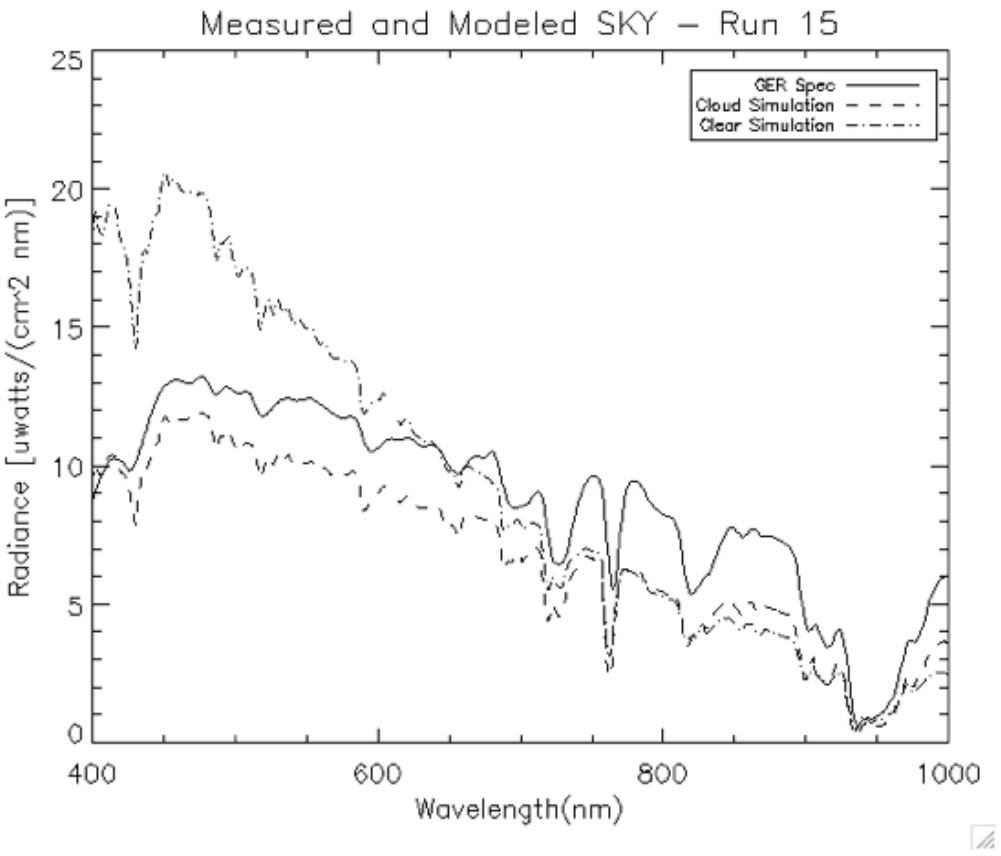

Figure 4.23: Absolute radiance comparison between measured and modeled sky values for run fifteen. Note that the measured value was produced using a sun blocker.

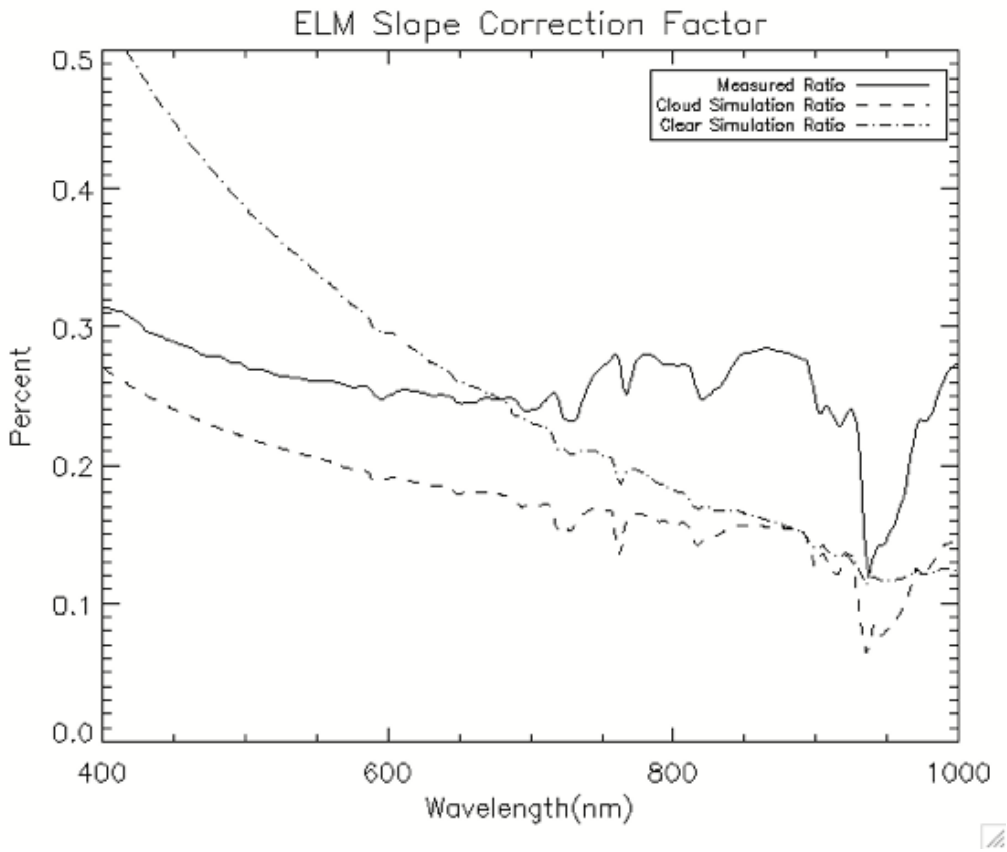

Figure 4.24: Correction ratio produced using different SKY values for the run fifteen validation. In this case, the cosine effect is not seen since its change is small compared with that of blocking the direct solar term.

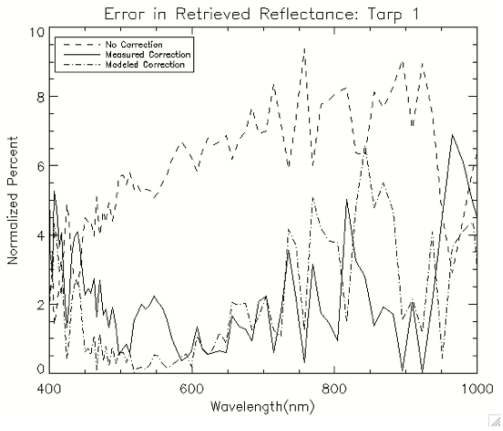

(a) Tarp 1 (8% tarp) - Hybrid Correction Run Ten

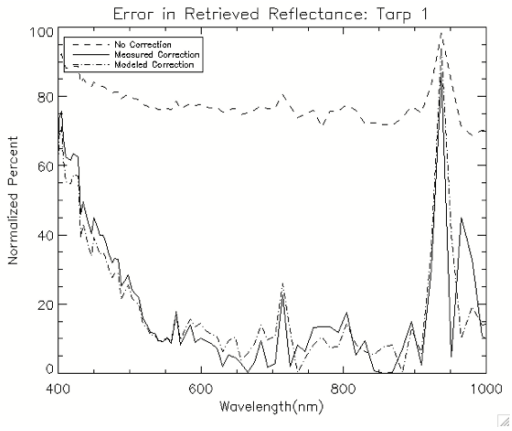

(b) Tarp 1 (8% tarp)- Run Fifteen

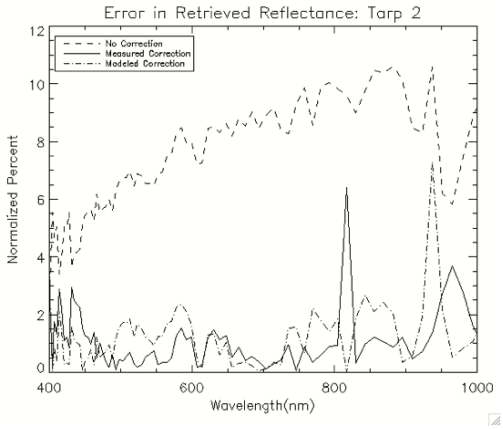

(c) Tarp 2 (16% tarp) - Hybrid Correction Run Ten

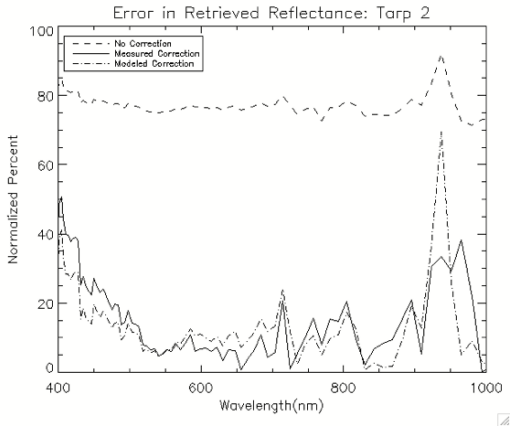

(d) Tarp 2 (16% tarp) -Run Fifteen

Figure 4.25: Percent error between retrieved reflectance for run seven and run fifteen. Results from of both pre and post hybrid correction shown.

There is again a significant amount of residual error present after the slope correction has been applied. As in the run 10 case, this can be explained by a change in path radiance. This change is much more pronounced now that the percentage of the sky that is covered in clouds has increased. Figure 4.26 shows this path radiance.

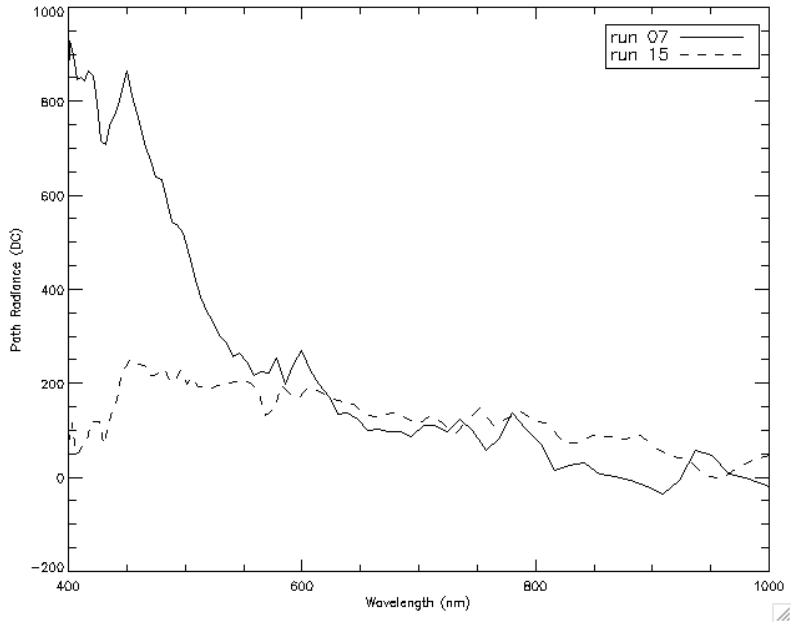

Figure 4.26: Path radiance from ground to sensor in sensor digital counts.

The percent change is again contrasted with the residual error from the AELM process in Figure 4.27. As before the residual error is in large part driven by the change in path radiance.

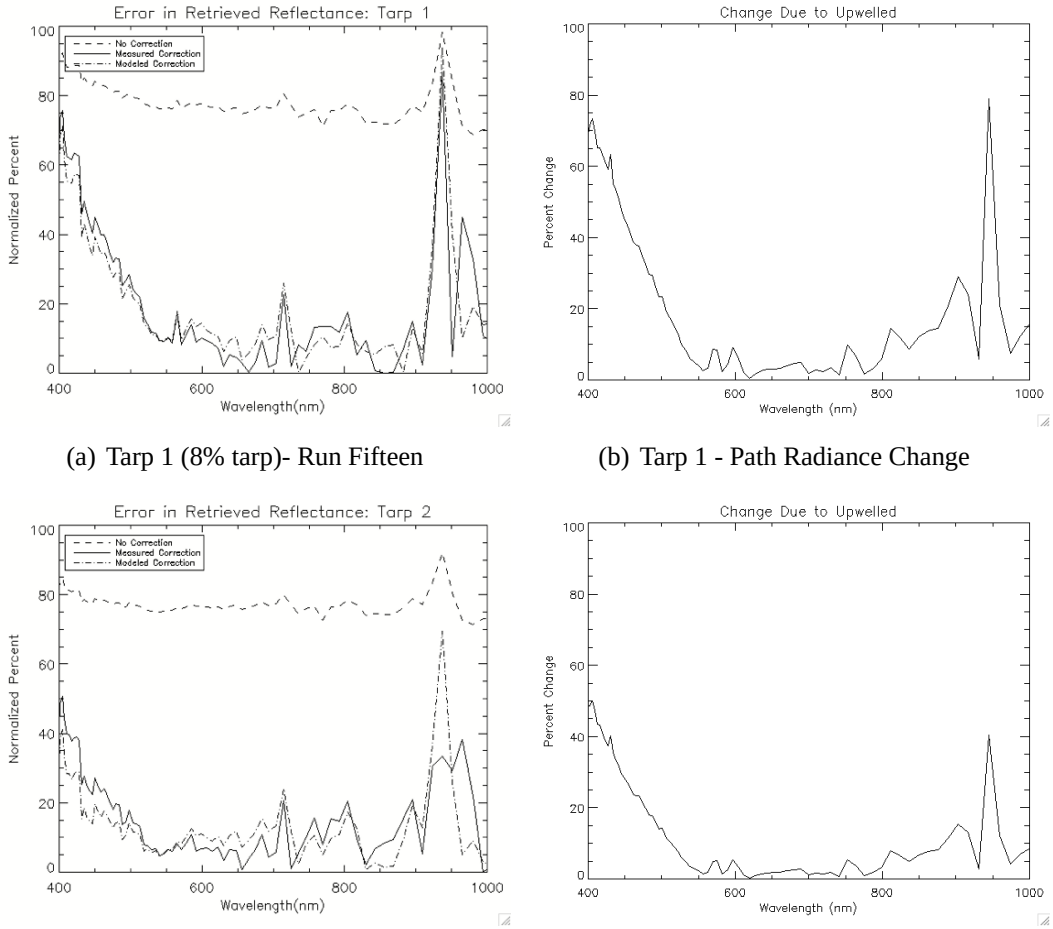

(a) Tarp 1 (8% tarp)- Run Fifteen

(b) Tarp 1 - Path Radiance Change

(c) Tarp 2 (16% tarp) -Run Fifteen

(d) Tarp 2 - Path Radiance Change

Figure 4.27: Percent error between retrieved reflectance for run seven and run fifteen. Results from of both pre and post hybrid correction shown.

An explanation for the way in which the path radiance is influenced by cloud cover is visualized in Figure 4.28. The path radiance is in effect lowered as a cloud casts a shadow through the path seen by the sensor. This will lower the path radiance observed at the sensor.

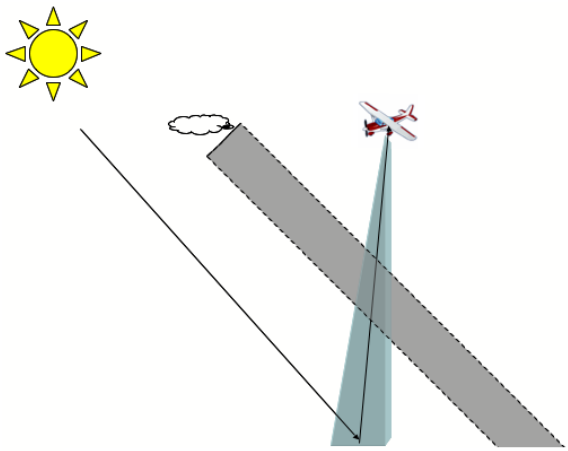

Figure 4.28: A cloud casts a shadow through the path seen by the sensor, thus lowering the path radiance.

This effect can be seen by correlating the upwelling radiance between the runs to the cloud cover present in the runs. Figure 4.29 shows the number of quads marked as clouds for each run. It shows that there are more clouds in run seven than in run ten and less clouds in run seven than in run fifteen. This means that there should be less path radiance in run seven than in run ten and more path radiance in run seven than in run fifteen. This effect is verified by Figures 4.20 and 4.26. An approach to account for this effect on upwelling path radiance is outlined in Chapter 6.

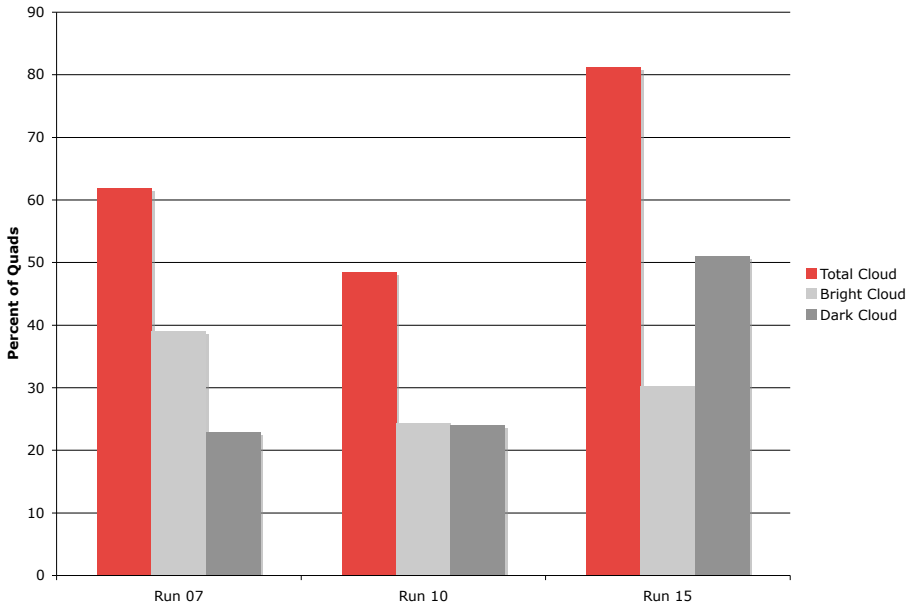

Figure 4.29: Cloud cover conditions for each run used in validation.

4.6 Multi-Spectral System

So far all work has been done hyper-spectrally using the HYDICE systems spectral response. However, many systems that are currently in use do not have spectral responses on the order of a few nanometers. The performance of the AELM will therefore be assessed using the spectral response of a multi-spectral system which has five bands.

This system is currently in use by the Laboratory for Imaging Algorithms and Systems at the Rochester Institute of Technology. It is a seven camera system that consists of one micro-bolometer long wave infrared camera, one infrared imager, and five silicon based CCD imagers. This study will use the spectral response of the five silicon camera system when fitted with a dichroic RGB set and two long-pass filters.

The spectral response of the multi-spectral system WASP LT was used to degrade the spectral resolution of the data from the ARM site. Figure 4.30(a) shows a diagram of the layout of the front of WASP LT which shows that it contains seven cameras. The response functions for the lower five cameras are used. Each camera has a different spectral filter, the set of which is comprised of a Dichroic red, green, blue, a 695nm longpass, and a 715nm longpass. The normalized spectral response functions were obtained through laboratory measurement which is outlined in appendix D. The current system has significant spectral response in the long wave for the RGB filter set. This research will however assume an IR reject is present for the first three cameras. This modified spectral response function is shown in Figure 4.30(b).

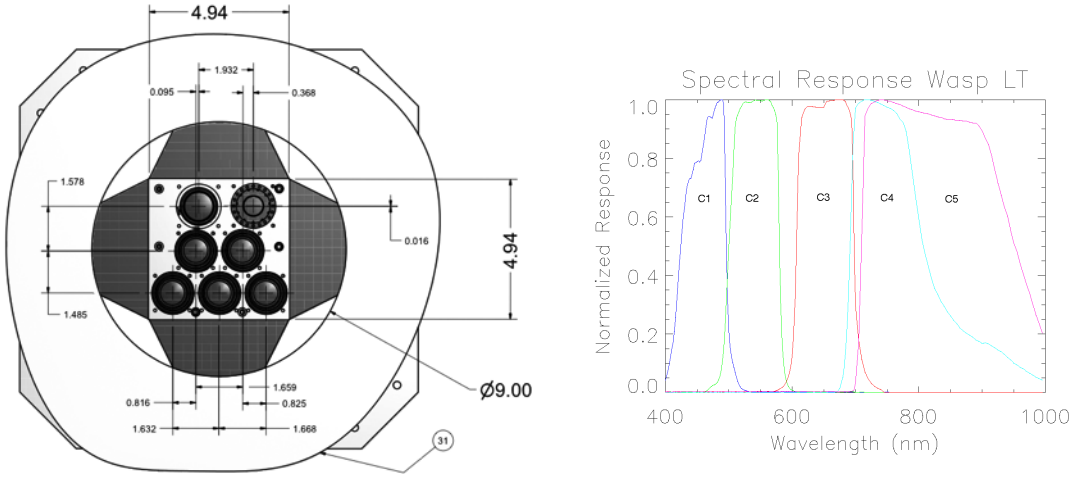

(a) CAD schematic of the front of WASP LT.

(b) Spectral response of WASP LT.

Figure 4.30: Wasp LT system used to degrade spectral resolution of HYDICE data.

In order to use the AELM with the five spectral bands defined by WASP LT, each measurement must be resampled spectrally. This includes the airborne imagery, the ground-based SKY measurements, the model-based SKY radiance, and the ground tarp reflectance. This process is shown in the following sections.

4.6.1 Spectral Resampling

The first step in resampling the data spectrally is to multiply the data by each of the five spectral response functions. Figure 4.31 shows the this step for the measured SKY value, the sensor digital count values for tarp 1, and the reflectance for tarp 1 during run 07.

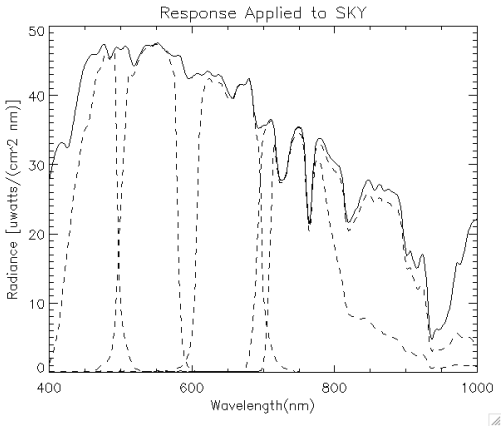

(a) SKY measurement resampling for run 07.

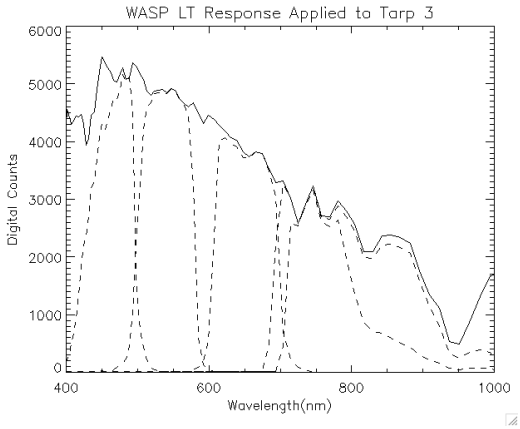

(b) Site tarp 3 (validation tarp 1) DC values resampled.

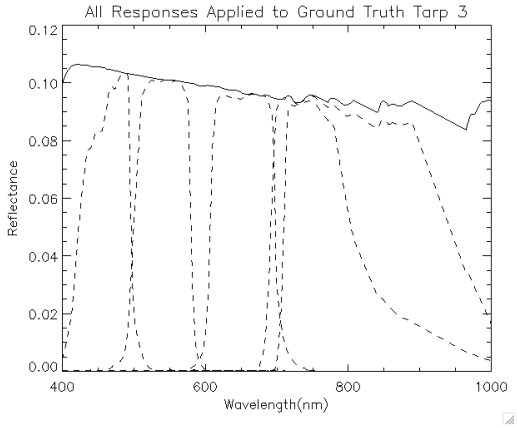

(c) Site tarp 3 (validation tarp 1) reflectance values resampled.

Figure 4.31: Applying spectral response for each camera to various measurements.Dotted lines represent values after multiplication for each camera.

Once the spectral response is applied, each curve is then integrated using equation 4.6 where μ represents the value being resampled and R is the spectral response of the camera being used.

$$\mu(\lambda)_{resampled} = \frac{\int \mu(\lambda) R(\lambda) d\lambda}{\int R(\lambda) d\lambda} \tag{4.6}$$

4.6.2 Multi-spectral Validation

Now that the data is spectrally down-sampled to the five band WASP LT system, the AELM process is applied in exactly the same was as shown in sections 4.4 and 4.5. The SKY correction ratio for both the hyper- and multi-spectral cases is shown in Figure 4.32.

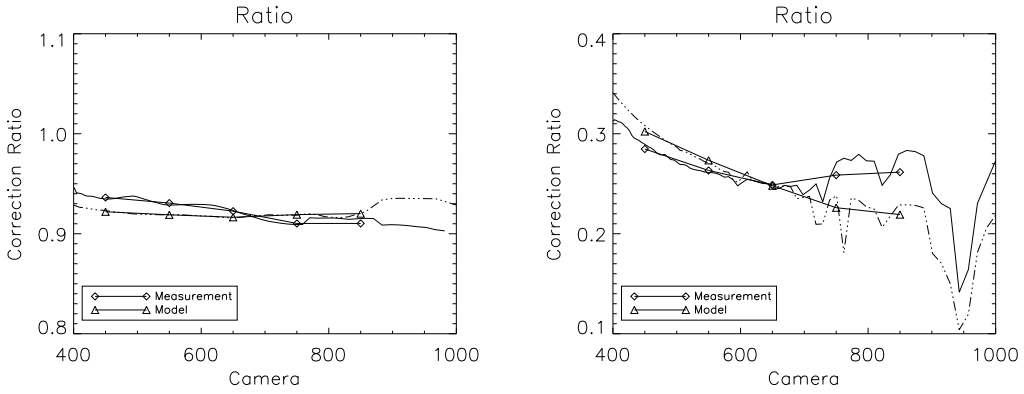

(a) SKY ratio for run 10

(b) SKY ratio for run 15

Figure 4.32: SKY ratio produced for after spectral down sampling. The five bands of WASP LT are shown overlaid with the hyper-spectral data which has been smoothed for easier comparison.

The run 07 slope can now be corrected for run 10 and run 15 using the new ratio and the reflectance for both validation tarps retrieved. Figure 4.33 shows the error for the five band system next to the hyper-spectral system. Note that the hyper-spectral error now includes the sign since this is what the mutli-spectral system is actually resampling.

The multi-spectral system has the interesting effect of improving the correction for longer wavelengths, specifically for cameras four and five, in the run 07 case. This is because the spectral resampling essentially averages the error which oscillates about

the x-axis. In this case, the resampling produces a net difference which is very close to zero. For run 15 this is not the case since the level of error is much higher. However, the multi-spectral system for this run does still average out much of the variability present in the longer wavelengths.

While all of the corrections discussed so far have used modeling with 1224 quads, the question of quad resolution on model accuracy has not yet been addressed. The next section will begin to explore this variable on algorithm performance.

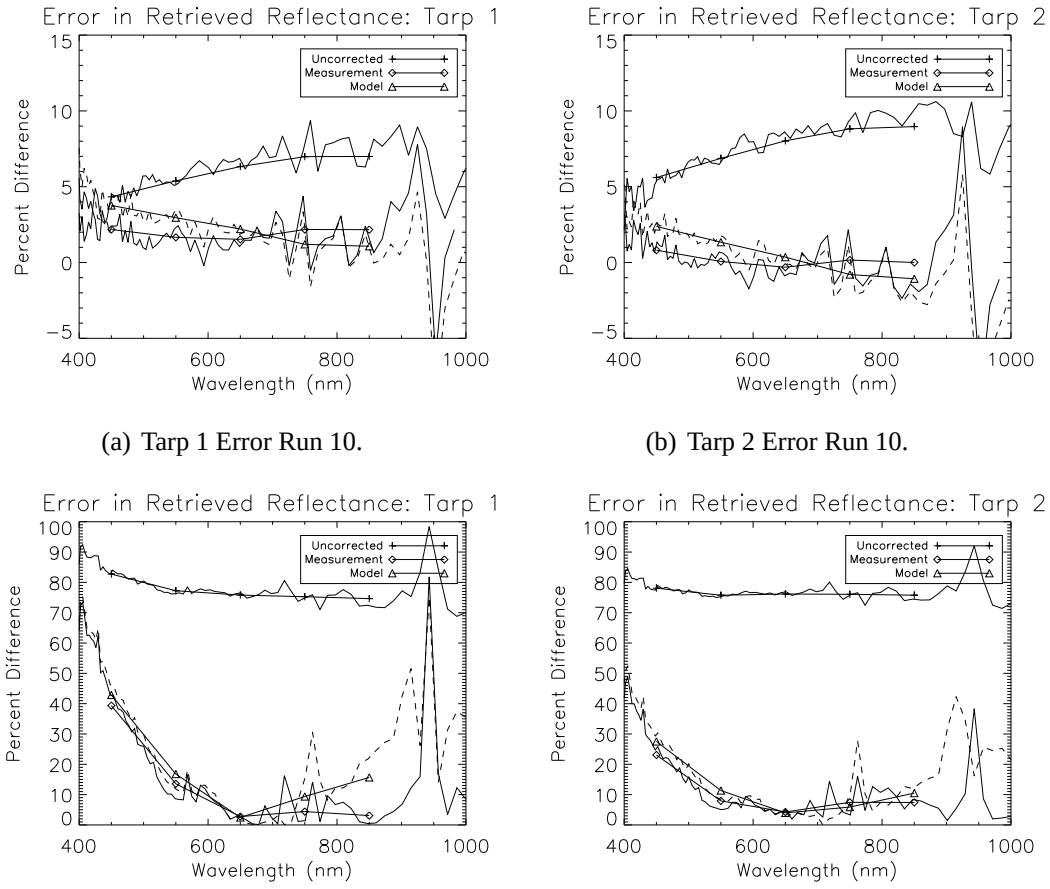

(a) Tarp 1 Error Run 10.

(b) Tarp 2 Error Run 10.

(c) Tarp 1 Error Run 15.

(d) Tarp 2 Error Run 15.

Figure 4.33: The percent difference between the retrieved reflectance obtained with AELM for each validation tarp for run 10 and the retrieved reflectance obtained with ELM for run 07.

4.7 Quad Resolution Effects

So far all SKY modeling has functioned by breaking the sky up into 1224 discrete quads. It is desirable however to have a fewer number of quads since it takes a substantial investment in time, approximately 20 minutes, for each MODTRAN run. To understand the effects of decreasing the number of quads, the specific way in which they are produced is first explained.

The quad generation algorithm takes the number of azimuth and zenith angles entered by the user to compute the angle between each quad center. Near the apex of the sky, the size of each quad can become very small. For this reason, the algorithm asks for the angular size of the top of the quad structure. This is called the endcap, which contains the scaled radiance from a MODTRAN run pointing straight up. The quad structure is then started from the bottom of the endcap. Figure 4.34 shows the location of the endcap in a situation where there are only 72 quads.

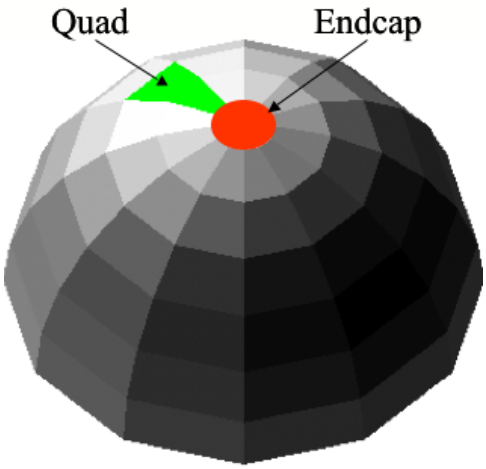

Figure 4.34: Three dimensional visualization of quad structure.

To test the effects of having a small versus larger number of quads, the parameters shown for 72 quads in Table 4.3 were used.

Table 4.3: Quad Parameters and Associated Angles

Total Quads	# Azimuth	# Zenith	Endcap Angle	Azimuth Angle	Zenith Angle
1224	72	17	5°	5°	5.15°
72	12	6	15°	30°	13.75°

The cloud masks generated at the 72 quad resolution are shown in Figure 4.35 and Figure 4.36.

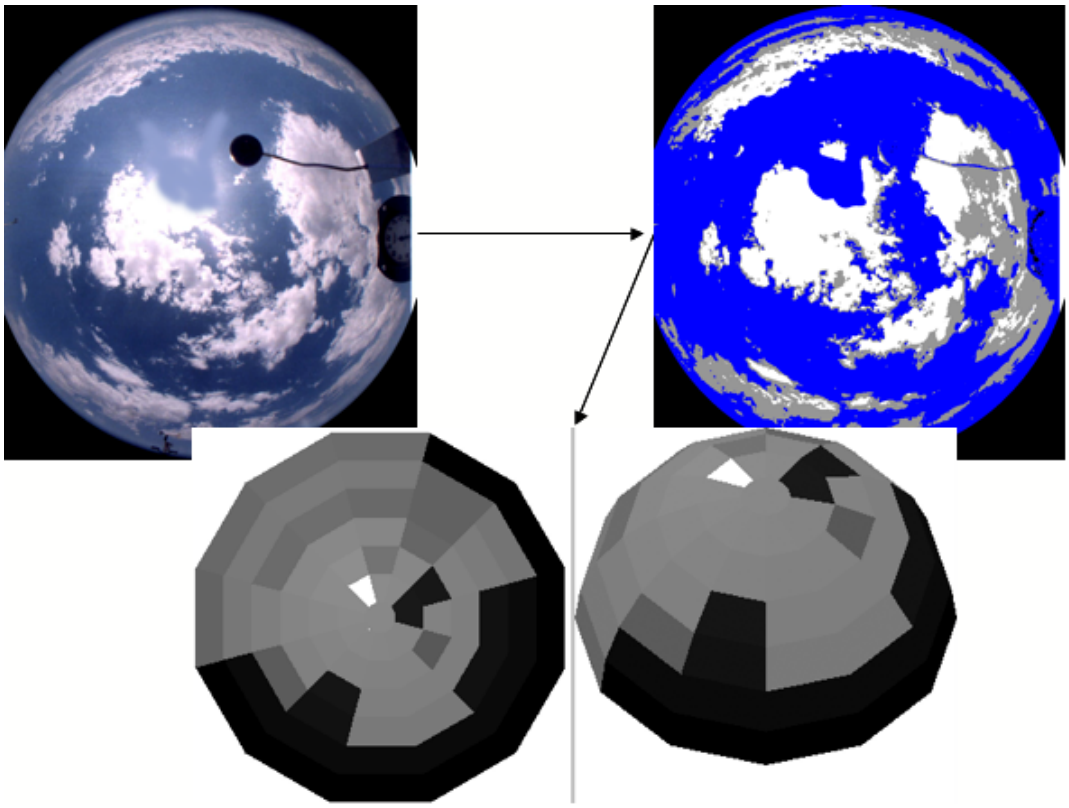

Figure 4.35: Run seven modeling process using 72 quads. The sun blocker in the original image was not operating correctly, so the sun glint is manually airbrushed out.

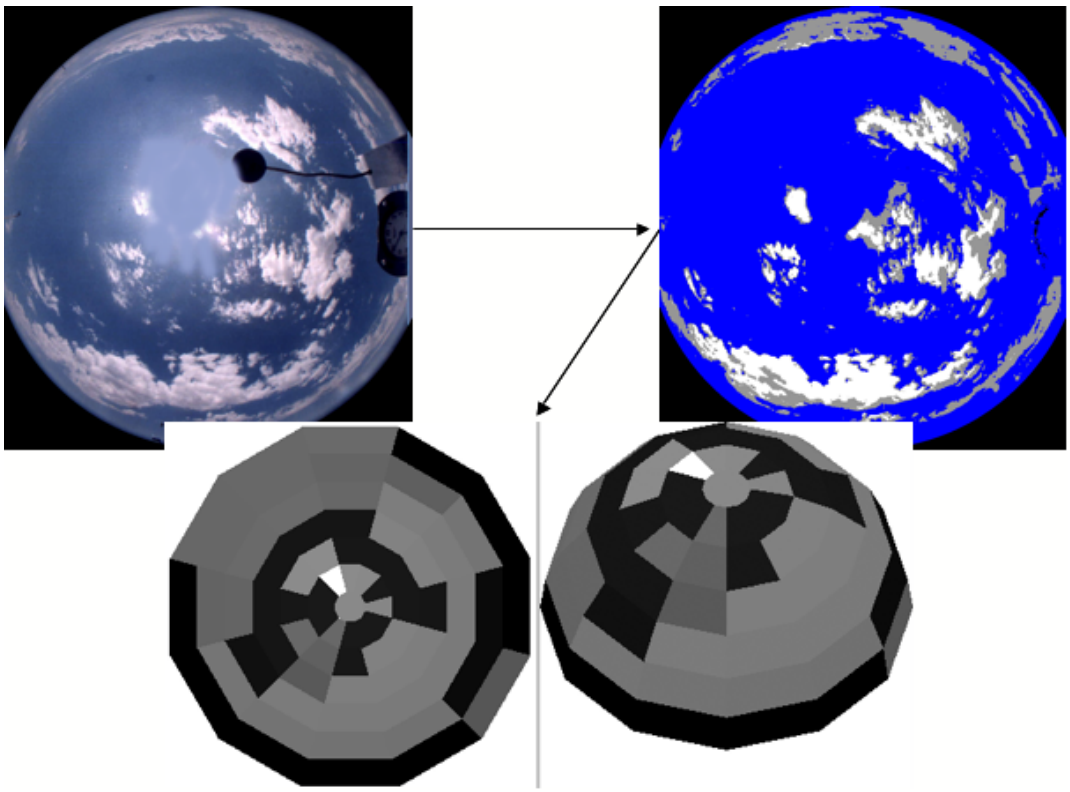

Figure 4.36: Run ten modeling process using 72 quads.

It has already been found that it is critical to model the area around the sun correctly in section 4.4.1. This would lead to the expectation that having fewer quads will produce a model which is less accurate than that of a high number of quads. Figure 4.37 shows the correction ratio produced using the fewer number of quads. The ratio compared to that which was produced by the 1224 quad run validates the previous assumption.

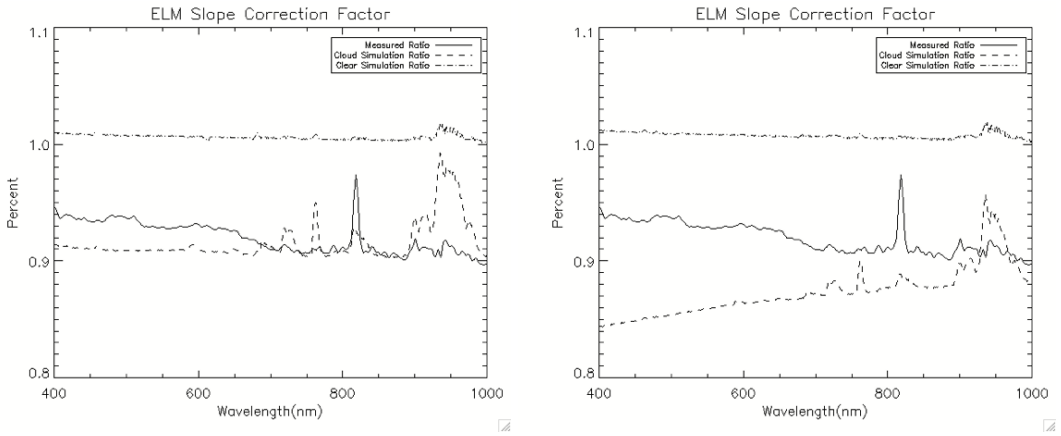

(a) Using 1224 quads. (b) Using 72 quads.

Figure 4.37: Correction ratio produced using different quad resolutions.

Final evidence that using fewer quads produces more error takes the form of error comparison in Figure 4.38 where once again the 1224 model outperforms the 72 quad model.

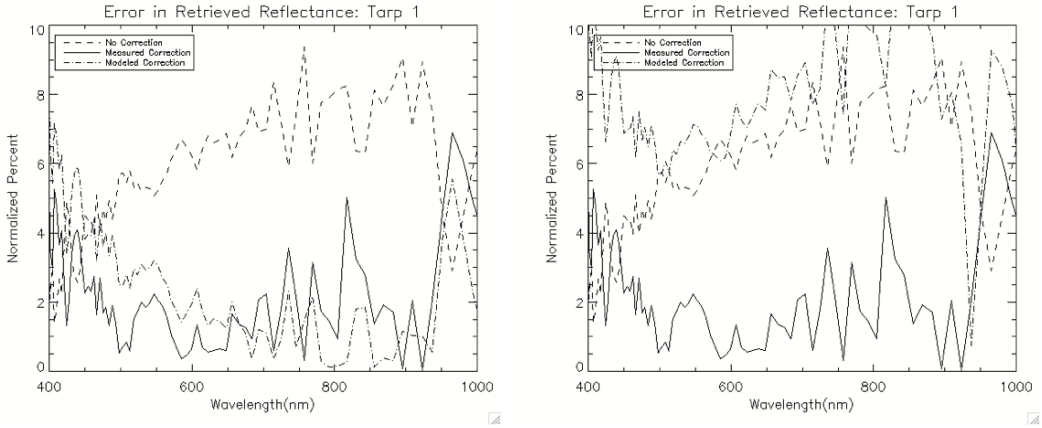

(a) Tarp 1 (8% tarp) - 1224 Quads

(b) Tarp 1 (8% tarp) - 72 Quads

(c) Tarp 2 (16% tarp) - 1224 Quads

(d) Tarp 2 (16% tarp) - 72 Quads

Figure 4.38: Percent error between retrieved reflectance for run seven and run ten after changing the number of quads in the model.

In this case, using a smaller number of quads produces only a few percent improvement over doing nothing at all. This again verifies using accurate representation of the cloud structure to produce the SKY term with modeling.

Since the spatial aspect of the cloud structure is so important, another approach can be taken which uses a smaller number of runs while maintaining a high spatial

resolution. This approach uses the 72 quad resolution to obtain the quad radiance values. A 1224 quad structure is then filled using the lower resolution radiometry. This idea is shown in Figure 4.39 where the 1224 quad structure is essentially draped over the 72 quad radiometry.

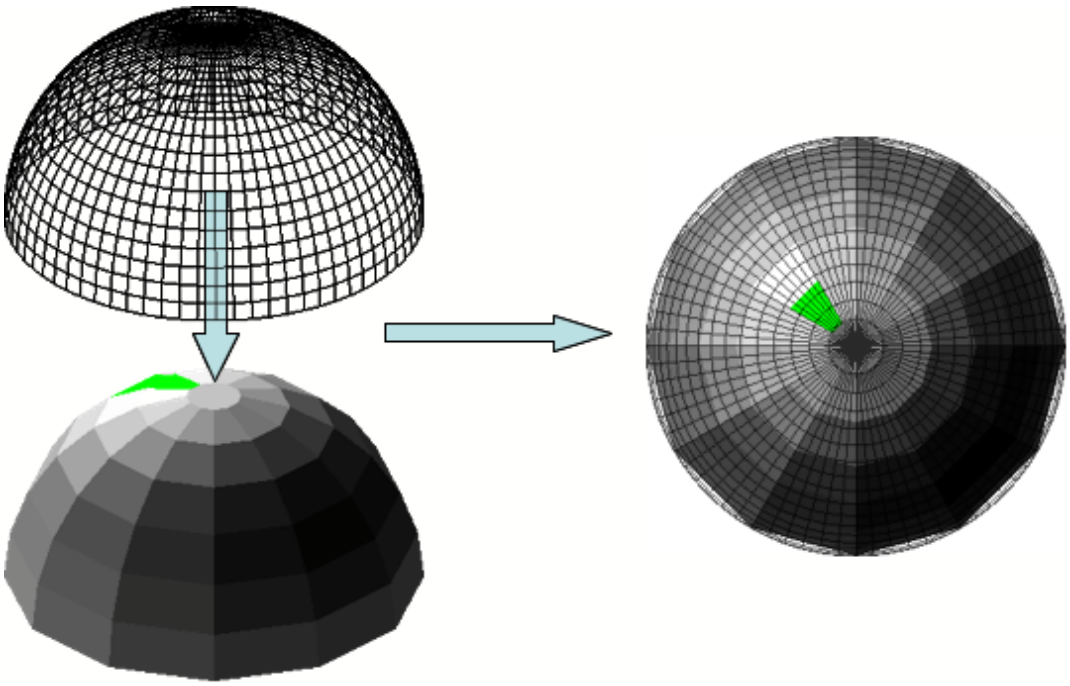

Figure 4.39: Process using 72 quad MODTRAN runs with 1224 quad spatial sampling.

The cloud masks generated with this new approach are shown in Figure 4.40 and Figure 4.41.

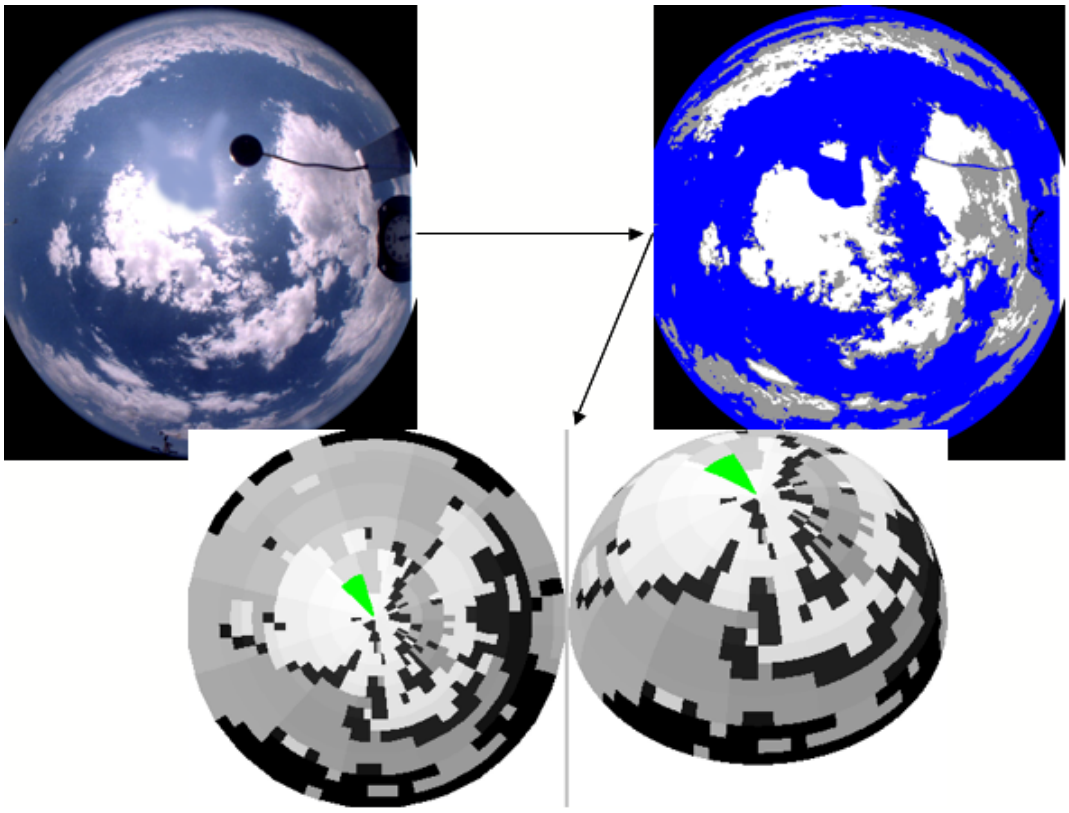

Figure 4.40: Run seven modeling process using 72 quad radiometry and 1224 quad spatial sampling.

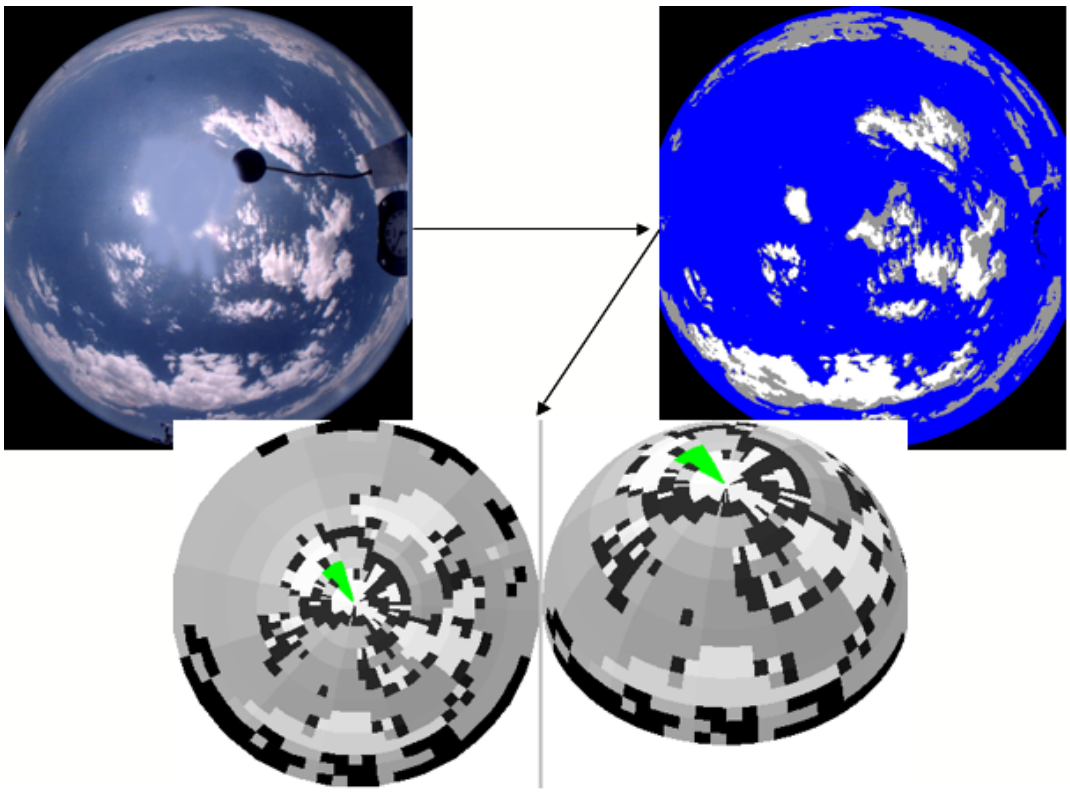

Figure 4.41: Run ten modeling process using 72 quad radiometry and 1224 quad spatial sampling.

This process should produce lower error in reflectance retrieval verses using the 72 quad structure alone since the spatial sampling utilizes a higher resolution. The first evidence that this statement is correct is shown in Figure 4.42 where the SKY ratio is indeed improved.

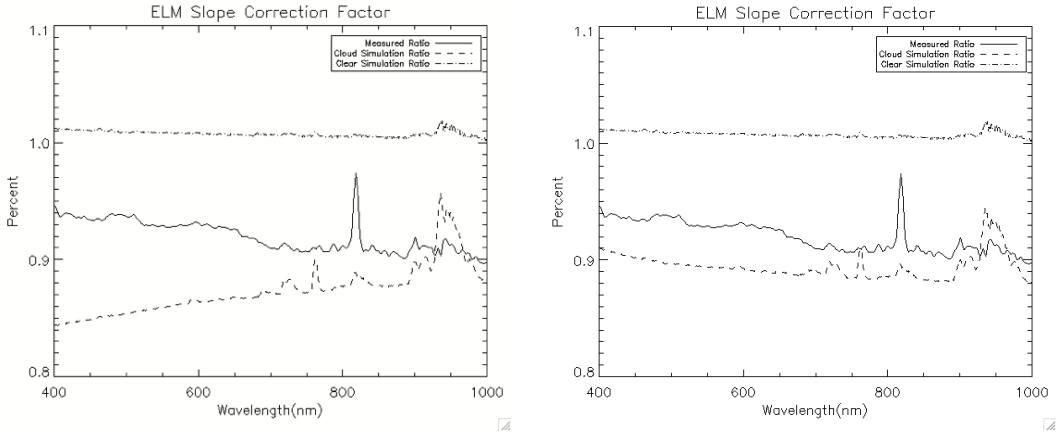

(a) Using 72 quads. (b) Using 1224 samples of 72 quads.

Figure 4.42: Correction ratio produced using different quad resolutions.

The error assessment shown in Figure 4.43 shows that this increased spatial sampling produces a retrieved reflectance error that is lower than using strictly a 72 quad approach. However the residual error in the lower wavelengths is still unacceptably high. One possible modification to this new sampling approach is outlined in chapter 6 which should help bring the error back to acceptable levels.

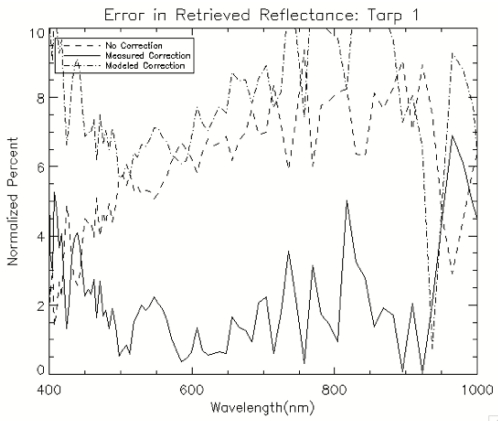

(a) Tarp 1 (8% tarp) - 72 quad resolution.

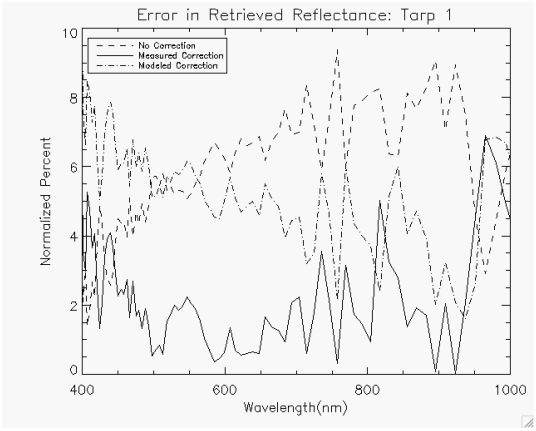

(b) Tarp 1 (8% tarp) - 72 quads with 1224 spatial samples.

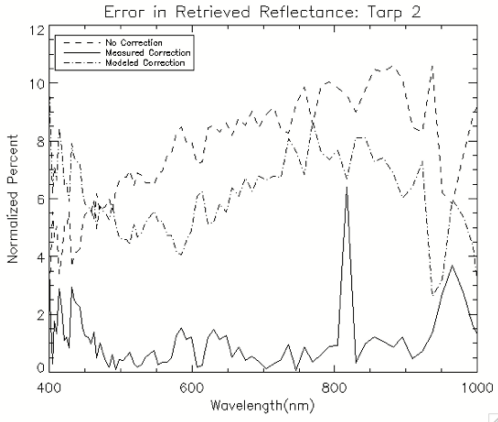

(c) Tarp 2 (16% tarp) - 72 quad resolution.

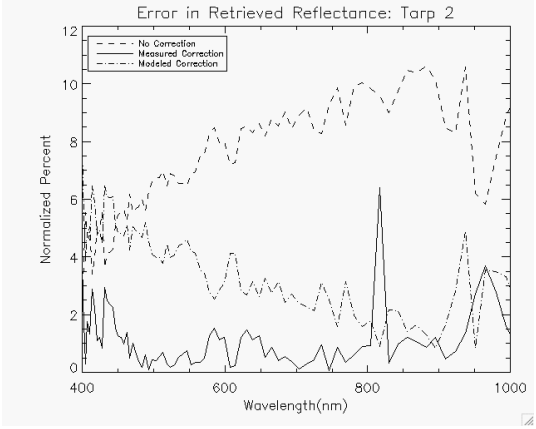

(d) Tarp 2 (16% tarp) - 72 quads with 1224 spatial samples.

Figure 4.43: Percent error between retrieved reflectance for run seven and run ten after changing the spatial sampling of the 72 quad run.

Chapter 5

Summary

The algorithm developed in this thesis is an empirical line method that will have a different LUT for each pixel. The process starts by performing the ELM at a calibration site with known reflectance measurements. This linear fit will be updated to account for illumination that varies spatially. The adjustment takes place by first generating a MODTRAN modeled database that matches the cloud location and overall SKY radiance. The cloud locations in the database are then adjusted to produce illumination values for pixels near the ELM calibration site.

The approach was tested by simulating the sensor reaching radiance for two different cloud configurations. When applying the linear fit from one configuration to another, error in retrieved reflectance was present. This error was reduced when adjusting the linear fit, even with incorrect cloud thickness.

A validation using real data was performed using temporal instead of spatial change. The validation tarps were located spatially close to the calibration tarps which meant that spatial correction could not be validated directly. However, since the clouds present during the collect were in motion, images from different times had significantly different illumination and cloud conditions. Imagery from three different times were used to validate the algorithm, run seven, ten, and fifteen. The first two had the validation site in direct sun while the third was under cloud shadow. The slope from run seven was adjusted and applied to both run ten and fifteen. The results indicate that in general adjustment using measurement will produce reflectance retrieval results that are within a few percent of those found using a traditional ELM in run seven. This is also the case using modeled and hybrid adjustments when direct sun is present. When cloud shadow occurs the retrieved reflectance is still on the order of ten percent different than run seven. However the relative decrease in error is the largest.

It is also useful to assess the pros and cons of the different correction methods to

determine which situations are ideal for which method. For instance, if the scene does not have a large number of clouds present it may be sufficient to use just measurements. The slope for each pixel in between the measurements could then be adjusted using a simple linear change with the SKY measurements as endpoints. If the scene has significant cloud cover, and the calibration site has a SKY measurement with high signal to noise then using the sky measurement to adjust the model would be best. The slope terms could then be adjusted on a per pixel (or multi-pixel) level with the model. If the scene has heavy cloud cover and the calibration site is under cloud shadow, it may be best to adjust the slope simply using the model unless a good signal can be achieved with measurement. Table 5.1 outlines some of these pros and cons.

Table 5.1: Pros and cons of Adaptive ELM Methods

Type	Pros	Cons
Measurement	Quick Accurate Assuming Good S/N	Expensive Small Spatial Range
Model	Good Spatial Resolution Adjustable Spectral Range	Model Inputs Required Long Initial Run Time
Hybrid	Less Expensive than Dual Measurement	Absolute Radiometric Calibration

It is also useful to consider the retrieved reflectance error metric as a panchromatic value as opposed to a spectral value. This value works well to give a sense of how each approach performs and is essentially the average error seen between 400nm and 1000nm. Table 5.2 shows this for each of the different methods used in correction of run 10 data.

Table 5.2: Summary of Average Spectral Error

Method	Tarp 1 Error	Tarp 2 Error
ELM	6.23	7.97
AELM Measurement	2.14	1.12
AELM 1224 Quad Model	2.20	1.32
AELM 72 Quad Model	8.23	5.84
AELM 72 Quad Model with 1224 Samples	4.89	3.10
Upwelling Residual	2.23	1.08

The summary shown in Table 5.2 indicates that the 1224 quad model performs on average within a few tens of a percent of the measurements. The 72 quad model performs much worse, but is improved when using a higher spatial sampling. This

shows that achieving a good spatial reconstruction of cloud cover will produce the best model results. The residual error is on average explained by the change in upwelling radiance. A discussion outlining possible modeling solutions to account for this effect is discussed in Chapter 6.

Chapter 6

Future Work

While the implementation of the current version of the adaptive ELM algorithm performs much better than using no correction at all, many different area's of improvement can be identified. These areas can be grouped into two sections; one for measurement and one for modeling.

6.1 Measurement

The major lesson learned in the validation portion of this thesis was that the cloud location in the modeling database was critical to good performance. This is particularly true near zenith and azimuth values close to the sun. There was no calibration data for the fisheye lens used to capture the cloud images. This means that there is error in obtaining the cloud azimuth and zenith values. This error can be minimized by calibration of the fisheye lens which is discussed in appendix A.

Another area that can be improved upon is the cloud height. This research simply used the default values for MODTRAN cumulus clouds, shown in Table 6.1.

Table 6.1: Default MODTRAN cloud parameters.

Cloud Type	Thickness (km)	Base (km)
Cumulus	2.34	0.66
Altostratus	0.60	2.40
Stratus	0.67	0.33

One way to measure cloud height is through the use of a laser ceilometer. Equipment of this nature is operational at many airports and will provide an estimate of the

height of the cloud deck. This type of instrument will not however give a good estimate of the height of each individual cloud. One approach that could be used to obtain cloud height for each cloud pixel is to use photogrammetric techniques. This approach is outlined in appendix B.

6.2 Modeling

While the first steps were taken in this thesis to model a three dimensional cloud field radiometrically, there is room for improvement. One area that could be improved upon is the sun / cloud geometry. The model so far has assumed just one scattering angle for all cloud locations. There could also be more rigorous tuning of the MODTRAN model parameters to obtain the closest possible spectral match between output model radiance and measured radiance at the calibration site.

While the model parameters are important, a better model could be developed to take into account the three-dimensional variability present in real world cloud structures since MODTRAN uses an infinite plane assumption. The current MODTRAN produced quads are independent of each other and therefore do not model the multiple scatter between cloud groupings correctly. One kind of modeling process which would work well for this type of multiple scattering would be photon mapping [Goodenough, 2007].

A photon mapping process could also be used to produce the path radiance based on a particular cloud configuration. It was seen in both the run 10 and run 15 cases that the path radiance was different than the run 07 case. While one explanation of this phenomena was presented at the end of section 4.5, the physical processes that lead to such an observed change in path radiance should be explored. Once the physics of the partial cloudy scene is understood, the residual error that is present in the AELM approach could be driven down with an appropriate model. When implementing the AELM algorithm spatially instead of temporally, the path length for each pixel will also change as a function of view angle. Figure 6.1 shows the results of a MODTRAN study showing the effect of view angle on both the path radiance and the transmission from the ground to the sensor (τ_2).

This study shows that even without cloud-cover present, the path radiance and transmission from the ground to sensor change significantly over high view angles. This should be accounted for when implementing the AELM algorithm over large spatial areas.

Another area that could be explored is the use of sampling when creating the cloud models. Current sampling of the hemisphere uses equal angular divisions over the az-

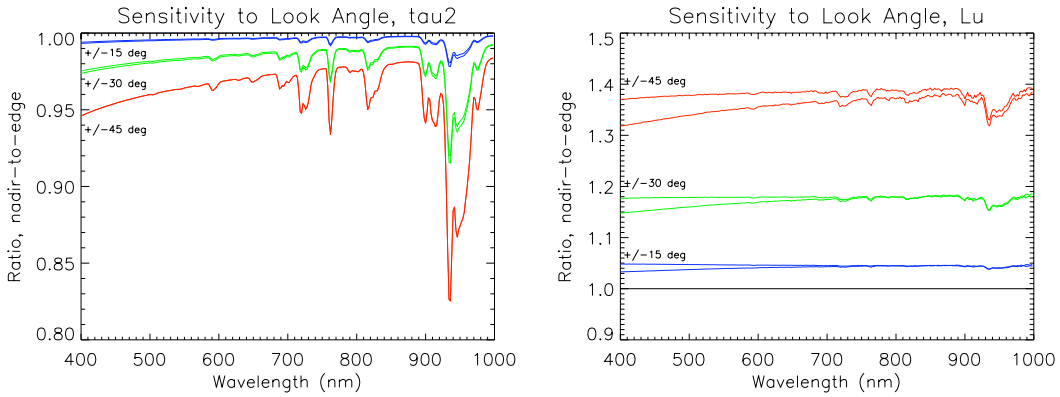

(a) Change in τ_2. (b) Change in L_u.

Figure 6.1: Percent change for both path radiance (L_u) and τ_2 in across-track direction, courtesy of Scott Klempner.

imuth and zenith. An approach was implemented which used a hemisphere filled with 72 MODTRAN runs to populate a 1224 quad hemisphere. This essentially allows for a more accurate cloud structure to be modeled while running MODTRAN fewer times. While the results using this approach had a higher error than running MODTRAN 1224 times, a sampling approach which over-samples near the sun and under-samples near the horizon should perform with higher accuracy. The sampling could also be determined by using the cloud mask to determine which areas of the sky should be sampled at a higher rate to resolve cloud structure with more fidelity.

6.3 Future Collection Scenarios

The research presented so far has been validated using a lapse in time to observe unique cloud configurations. However, the question of exactly how retrieved reflectance changes spatially under different cloud conditions needs to be addressed. Figure 6.2 shows just one way that error could increase as distance increases from the calibration area. In fact, in real world situations, the error will most likely follow irregular shapes much like cloud shadows. In order to observe this variation an airborne collection should focus on placing validation tarps at spatial intervals throughout the scene. This will also allow for the AELM algorithm to be validated in a spatial manner.

In an operational sense, the inputs for the AELM radiometric modeling process can also be derived from data sources such as satellite products. For example, if fisheye

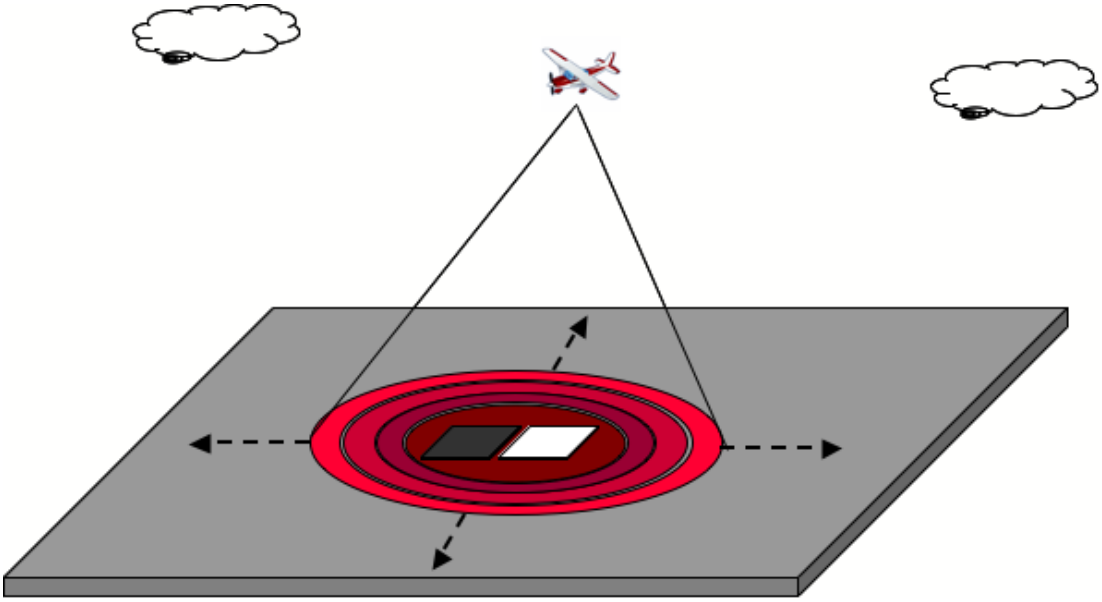

Figure 6.2: As distance from the calibration site, in this case shown with two tarps, increases, so does the error in retrieved reflectance. Lighter shades of red indicate higher levels of error.

imagery is not available, an estimate of cloud location and height can be derived from a data source such as the Geostationary Operational Environmental Satellite (GOES) system. Combined with a digital elevation map of the scene, the angular location of each cloud as seen from each pixel can then be calculated using the geometry outlined in appendix B. This relaxes the requirement for a fisheye image to be obtained from the ground. The value for the SKY term produced using this model could also be incorporated into such reflectance retrieval algorithms such as FLAASH and ATREM, discussed in section 2.1.2. Successfully merging the SKY term which takes into account cloud variability into such radiometric algorithms would further relax the requirement of calibration tarps which is the main drawback of performing an AELM in certain collection scenarios such as restricted parts of the world.

Appendix A

Fisheye Lens Calibration

Whole sky images used for obtaining cloud locations in this research are made with wide angle lens configurations, commonly known as fisheye lenses. Such lens systems produce large amounts of aberrations. In order to obtain the azimuth and zenith angles for clouds located in such images, the type of lens distortion must be known. Calibration is also critical when performing an AELM spatially on a scene. The validation section used time to obtain shifted cloud images, however if the AELM is applied spatially to the whole scene, the cloud images must be shifted geometrically. This means that lens distortion must be removed.

One way to characterize the lens distortion present is to image a scene which has objects with known spatial parameters [Wolf and Dewitt, 2000]. The Laboratory for Imaging Algorithms and Systems in the Rochester Institute of Technology has a calibration cage which can be used to form such images which is shown in Figure A.1.

It is essentially a cube which has reflective stickers affixed to the edges. Since the spatial location of each sticker is known, they can be used in a nine photo-block photogrammetric adjustment to determine the lens distortion parameters. Figure A.2 shows the location where each image was taken relative to the cage, and which points were found in common.

The lens calibration software Australis was used to find the coefficients in the symmetric radial distortion and de-centering distortion, shown in equations A.1 and A.2.

$$dr = k_1 r^3 + k_2 r^5 + k_3 r^7 \tag{A.1}$$

$$\begin{aligned} dx &= p_1(r^2 + 2x^2) + 2p_2 xy \\ dy &= p_2(r^2 + 2y^2) + 2p_1 xy \end{aligned} \tag{A.2}$$

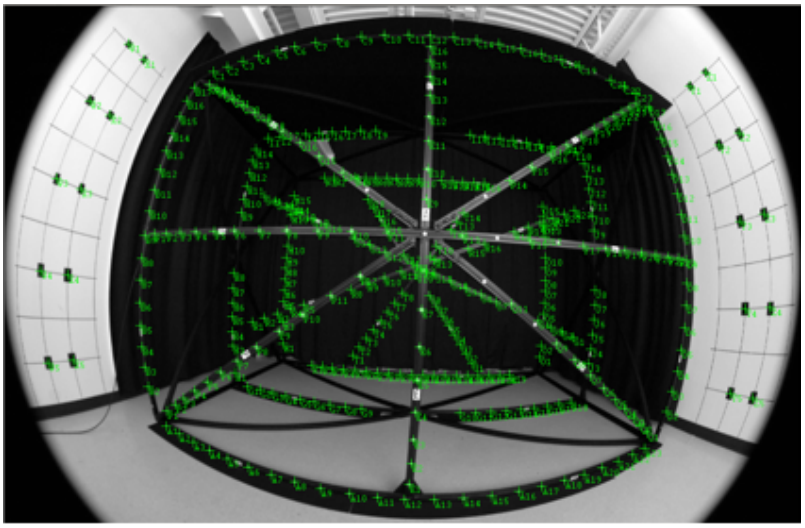

Figure A.1: Calibration cage used to correct lens distortions. Green dots highlight the sticker locations.

After the distortion parameters are found the images can then corrected. This is done by shifting the pixels based on the radial distance from the lens center. The image is then re-grided and interpolated to the new pixel centers. Figure A.3 shows the results of applying the correction to an image of the cage. This correction was performed on a Nikon D50 with Sigma 8mm wide angle lens. The correction was also applied to a sky image which is shown in Figure A.4.

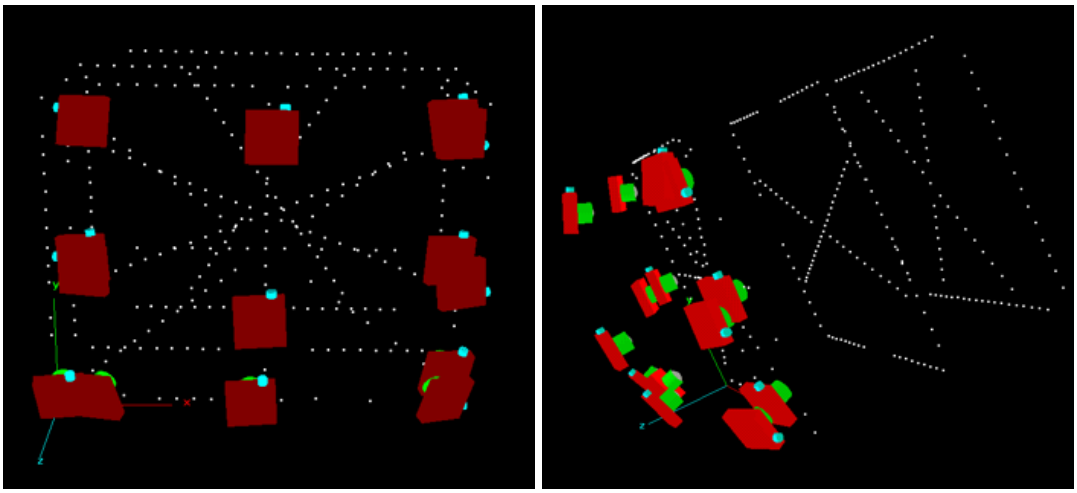

(a) View from front. (b) View from side.

Figure A.2: Camera locations indicated by red objects, common points used in correction are shown with white dots.

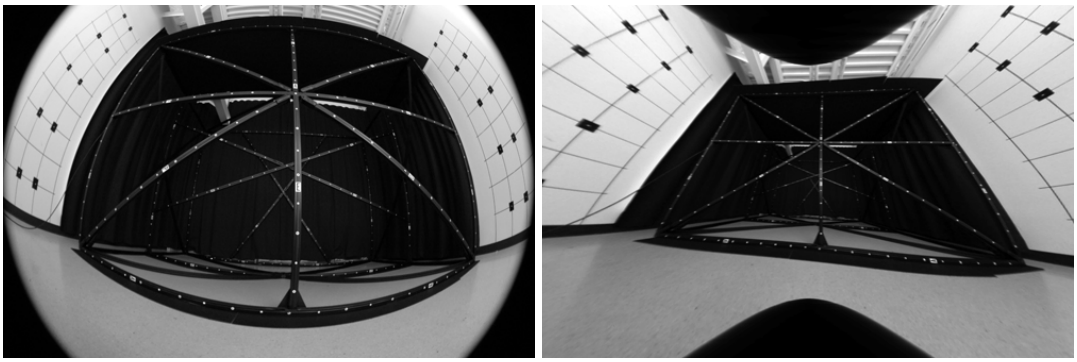

(a) Before Correction (b) After Correction

Figure A.3: Calibration applied to cage image. The bars of the cage appear much straighter after applying the correction.

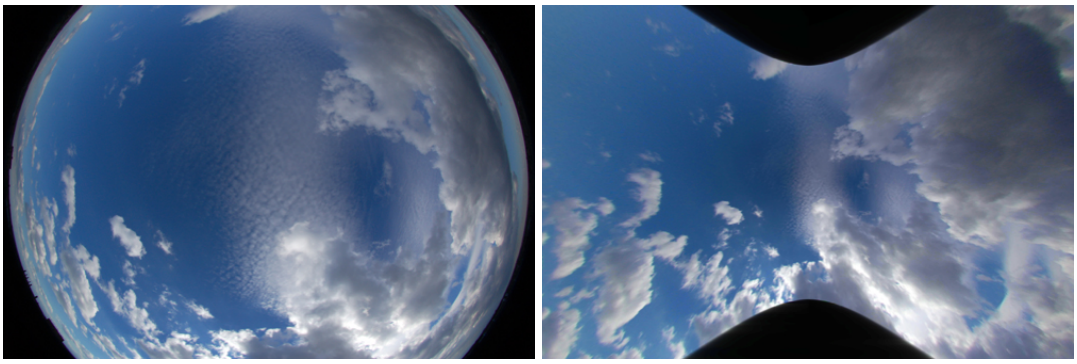

(a) Before Correction (b) After Correction

Figure A.4: Calibration applied to sky image. Interpolation error starts to become apparent at extreme edges.

Appendix B

Cloud Height Determination

One source of error that could be minimized is that of cloud height. While the AELM works using the default value for height present in MODTRAN, the cloud height also needs to be known in order to shift the whole sky image as discussed in appendix A.

Photogrammetry allows for the determination of the height and position of points on the ground. A system of ground control points with known location and aircraft with accurate GPS and orientation can be used to solve for the point parameters. This problem is laid out in the following sections since it can be used to solve the problem of cloud height.

B.1 Photogrammetric Bundle Adjustment

B.1.1 Introduction

This section will describe how to set up a 3-photo bundle adjustment. This is intended to supplement section 17-9 of the text *Elements of Photogrammetry* [Wolf and Dewitt, 2000].

This explanation is based on the following 3-photo arrangement, but the math is kept general for any number of points and photo's.

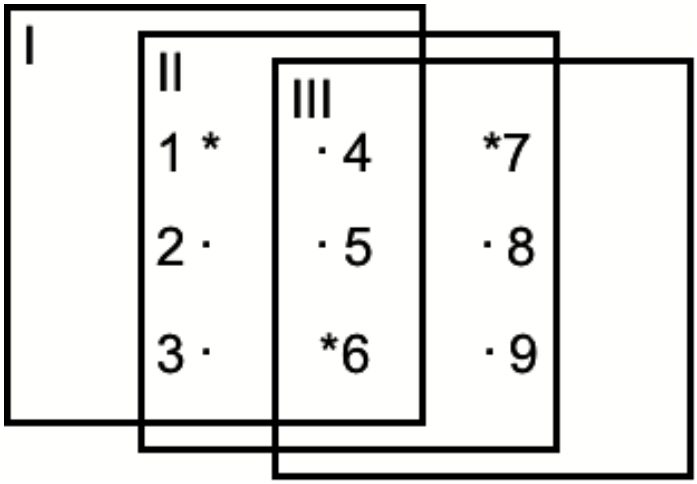

Figure B.1: The layout of photos used in this document. $*$ indicates control point while $\bullet$ indicates tie point.

B.1.2 Defining the Problem

The overall problem can be expressed in the following matrix form:

$$\begin{aligned} \boldsymbol{B\delta} &= \boldsymbol{\epsilon - V} \\ \boldsymbol{\delta} &= \left(\boldsymbol{B^T B}\right)^{-1} \boldsymbol{B^T \epsilon} \end{aligned} \tag{B.1}$$

where $\boldsymbol{B}$ is called the observation matrix, $\boldsymbol{\delta}$ is called the correction matrix (which we will be solving for), $\boldsymbol{\epsilon}$ is called the error matrix, and $\boldsymbol{V}$ are the residuals. A weighting matrix can be inserted to allow for the uncertainty of the observations to be included. With the weight matrix the solution becomes:

$$\boldsymbol{\delta} = \left(\boldsymbol{B^T W B}\right)^{-1} \boldsymbol{B^T W \epsilon} \tag{B.2}$$

To find the residuals, $\boldsymbol{V}$:

$$\boldsymbol{V} = \boldsymbol{W\epsilon - WB\delta}$$

B.1.3 Observation Matrix

With the equation structure laid out, it is time to start defining what is in the matrices. The first matrix discussed is $\boldsymbol{B}$ since understanding it is the key to the whole problem. $\boldsymbol{B}$ contains the coefficients to the observation equations. These equations come from three sources. The first is from measured photo coordinates in the images which are used in the linearized form of the collinearity equations, as defined in appendix D-4 in Wolf's book. The next source can come from the inertial measurement unit (IMU) on the aircraft. These values are used as constraints on the elements of orientation. The final source comes from the use of GPS from a surveyor. These values are constraints on the ground points, or ground control points. Each set of points will fit into the observation matrix in a particular way which will require definition.

Contribution from the Collinearity Equations

The collinearity equations relate an image point to the ground accounting for the geometry of the system. This geometry is shown in the following figure:

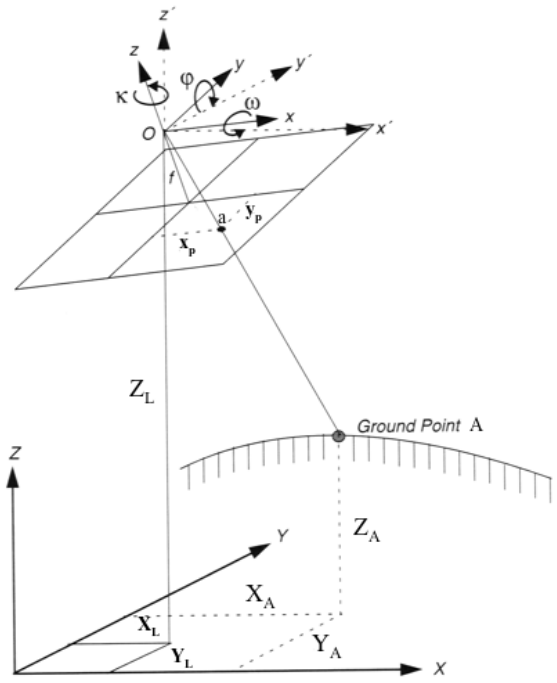

Figure B.2: The terms of in the collinearity equation defined by their geometry.

An analysis of Figure B.2 will produce the following equations which are in fact the collinearity equations:

$$\begin{aligned} F_x = x_A - x_p &= -f\left[\frac{m_{11}(X_A - X_L) + m_{12}(Y_A - Y_L) + m_{13}(Z_A - Z_L)}{m_{31}(X_A - X_L) + m_{32}(Y_A - Y_L) + m_{33}(Z_A - Z_L)}\right] \\ 0 &= x_A - x_p + f\frac{U}{W} \end{aligned} \tag{B.3}$$

$$\begin{aligned} F_y = y_A - y_p &= -f\left[\frac{m_{21}(X_A - X_L) + m_{22}(Y_A - Y_L) + m_{23}(Z_A - Z_L)}{m_{31}(X_A - X_L) + m_{32}(Y_A - Y_L) + m_{33}(Z_A - Z_L)}\right] \\ 0 &= y_A - y_p + f\frac{V}{W} \end{aligned} \tag{B.4}$$

where:

$$\begin{aligned} U &= m_{11}(X_A - X_L) + m_{12}(Y_A - Y_L) + m_{13}(Z_A - Z_L) \\ V &= m_{21}(X_A - X_L) + m_{22}(Y_A - Y_L) + m_{23}(Z_A - Z_L) \\ W &= m_{31}(X_A - X_L) + m_{32}(Y_A - Y_L) + m_{33}(Z_A - Z_L) \end{aligned}$$

and m_{xx} are elements of the orientation matrix. The orientation matrix accounts for the roll(ω), pitch(ϕ), and yaw(κ) of the aircraft. The following shows the orientation matrices for each angle, as well as their product.

$$\begin{aligned} M &= \underset{M_\kappa}{\begin{bmatrix} cos\kappa & sin\kappa & 0 \\ -sin\kappa & cos\kappa & 0 \\ 0 & 0 & 1 \end{bmatrix}} \underset{M_\phi}{\begin{bmatrix} cos\phi & 0 & -sin\phi \\ 0 & 1 & 0 \\ sin\phi & 0 & cos\phi \end{bmatrix}} \underset{M_\omega}{\begin{bmatrix} 1 & 0 & 0 \\ 0 & cos\omega & sin\omega \\ 0 & -sin\omega & cos\omega \end{bmatrix}} \\ &= \begin{bmatrix} cos\phi cos\kappa & cos\omega sin\kappa + sin\omega sin\phi cos\kappa & sin\omega sin\kappa - cos\omega sin\phi cos\kappa \\ -cos\phi sin\kappa & cos\omega cos\kappa - sin\omega sin\phi sin\kappa & sin\omega cos\kappa + cos\omega sin\phi sin\kappa \\ sin\phi & -sin\omega cos\phi & cos\omega cos\phi \end{bmatrix} \end{aligned}$$

The angles in the above equation are all defined in Figure B.2. The collinearity

equations can be linearized using Taylor's theorem, as shown next:

$$\begin{aligned} x_A - x_p &= F_x + \left(\frac{\partial F}{\partial \omega}\right)_o d\omega + \left(\frac{\partial F}{\partial \phi}\right)_o d\phi + \left(\frac{\partial F}{\partial \kappa}\right)_o d\kappa + \left(\frac{\partial F}{\partial X_L}\right)_o dX_L \\ &\quad + \left(\frac{\partial F}{\partial Y_L}\right)_o dY_L + \left(\frac{\partial F}{\partial Z_L}\right)_o dZ_L \\ &\quad + \left(\frac{\partial F}{\partial X_A}\right)_o dX_A + \left(\frac{\partial F}{\partial Y_A}\right)_o dY_A + \left(\frac{\partial F}{\partial Z_A}\right)_o dZ_A \end{aligned}$$

$$\begin{aligned} y_A - y_p &= F_y + \left(\frac{\partial G}{\partial \omega}\right)_o d\omega + \left(\frac{\partial G}{\partial \phi}\right)_o d\phi + \left(\frac{\partial G}{\partial \kappa}\right)_o d\kappa + \left(\frac{\partial G}{\partial X_L}\right)_o dX_L \\ &\quad + \left(\frac{\partial G}{\partial Y_L}\right)_o dY_L + \left(\frac{\partial G}{\partial Z_L}\right)_o dZ_L \\ &\quad + \left(\frac{\partial G}{\partial X_A}\right)_o dX_A + \left(\frac{\partial G}{\partial Y_A}\right)_o dY_A + \left(\frac{\partial G}{\partial Z_A}\right)_o dZ_A \end{aligned}$$

Each derivative is evaluated with initial approximations. These approximations need to be refined, so the problem is to solve for the correction factors. These factors are $[d\omega, d\phi, d\kappa, dX_L, dY_L, dZ_L, dX_A, dY_A, dZ_A]$. The above equation can be re-written as follows:

$$\begin{aligned} F_x &\approx b_{11}d\omega + b_{12}d\phi + b_{13}d\kappa - b_{14}dX_L - b_{15}dY_L - b_{16}dZ_L \\ &\quad + b_{14}dX_A + b_{15}dY_A + b_{16}dZ_A \\ F_y &\approx b_{21}d\omega + b_{22}d\phi + b_{23}d\kappa - b_{24}dX_L - b_{25}dY_L - b_{26}dZ_L \\ &\quad + b_{24}dX_A + b_{25}dY_A + b_{26}dZ_A \end{aligned}$$

Where the derivatives have been defined as follows:

$$\triangle X = X_A - X_L \quad \triangle Y = Y_A - Y_L \quad \triangle Z = Z_A - Z_L$$

$$
\begin{aligned}
b_{11} &= \tfrac{f}{W^2}\left[U(-m_{33}\triangle Y + m_{32}\triangle Z) - W(-m_{13}\triangle Y + m_{12}\triangle Z)\right] \\
b_{12} &= \tfrac{f}{W^2}[U(cos\phi\triangle X + sin\omega sin\phi\triangle Y - cos\omega sin\phi\triangle Z) \\
&\quad -W(-sin\phi cos\kappa\triangle X + sin\omega cos\phi cos\kappa\triangle Y - cos\omega cos\phi cos\kappa\triangle Z)] \\
b_{13} &= \tfrac{-f}{W}(m_{21}\triangle X + m_{22}\triangle Y + m_{23}\triangle Z) \\
b_{14} &= \tfrac{f}{W^2}(Um_{31} - Wm_{11}) \\
b_{15} &= \tfrac{f}{W^2}(Um_{32} - Wm_{12}) \\
b_{16} &= \tfrac{f}{W^2}(Um_{33} - Wm_{13}) \\
b_{21} &= \tfrac{f}{W^2}\left[V(-m_{33}\triangle Y + m_{32}\triangle Z) - W(-m_{23}\triangle Y + m_{22}\triangle Z)\right] \\
b_{22} &= \tfrac{f}{W^2}[V(cos\phi\triangle X + sin\omega sin\phi\triangle Y - cos\omega sin\phi\triangle Z) \\
&\quad -W(-sin\phi cos\kappa\triangle X + sin\omega cos\phi cos\kappa\triangle Y - cos\omega cos\phi cos\kappa\triangle Z)] \\
b_{23} &= \tfrac{-f}{W}(m_{21}\triangle X + m_{22}\triangle Y + m_{23}\triangle Z) \\
b_{24} &= \tfrac{f}{W^2}(Vm_{31} - Wm_{21}) \\
b_{25} &= \tfrac{f}{W^2}(Vm_{32} - Wm_{22}) \\
b_{26} &= \tfrac{f}{W^2}(Vm_{33} - Wm_{23})
\end{aligned}
$$

With this formulation the first set of observation equations can be formed and placed into the matrix $\boldsymbol{B}$.

$$\dot{\boldsymbol{B}}_{ij}\dot{\boldsymbol{\delta}}_i + \ddot{\boldsymbol{B}}_{ij}\ddot{\boldsymbol{\delta}}_j = \boldsymbol{\epsilon}_{ij} + \boldsymbol{V}_{ij}$$

where j is a point on photo i. The elements contained inside the dotted $\boldsymbol{B}$ and $\boldsymbol{\delta}$ matrices are:

$$\dot{\boldsymbol{B}} = \begin{bmatrix} b_{11} & b_{12} & b_{13} & -b_{14} & -b_{15} & -b_{16} \\ b_{21} & b_{22} & b_{23} & -b_{24} & -b_{25} & -b_{26} \end{bmatrix} \quad \ddot{\boldsymbol{B}} = \begin{bmatrix} b_{14} & b_{15} & b_{16} \\ b_{24} & b_{25} & b_{26} \end{bmatrix}$$

$$\dot{\boldsymbol{\delta}} = \begin{bmatrix} d\omega \\ d\phi \\ d\kappa \\ dX_L \\ dY_L \\ dZ_L \end{bmatrix} \quad \ddot{\boldsymbol{\delta}} = \begin{bmatrix} dX_j \\ dY_j \\ dZ_j \end{bmatrix} \quad \boldsymbol{\epsilon} = \begin{bmatrix} (x^o - x_p) - x^c \\ (y^o - y_p) - y^c \end{bmatrix} \quad \boldsymbol{V} = \begin{bmatrix} v_x \\ v_y \end{bmatrix}$$

The $\boldsymbol{\epsilon}$ array holds the measured minus the computed x and y photo coordinates for point j on photo i while the $\boldsymbol{V}$ array holds the residuals. We can now place the dotted $\boldsymbol{B}$ matrices in the $\boldsymbol{B}$ matrix as follows:

$$\boldsymbol{B} = \begin{bmatrix} \dot{\boldsymbol{B}}_1 & \dot{\boldsymbol{B}}_2 & \ldots & \dot{\boldsymbol{B}}_m & \ddot{\boldsymbol{B}}_1 & \ddot{\boldsymbol{B}}_2 & \ldots & \ddot{\boldsymbol{B}}_g \\ . & & . & & . & & . & \\ & . & & . & & . & & . \\ & & . & & . & & . & \\ & & & . & & . & & . \end{bmatrix}^1_{2n}$$

where m is the number of photo's, g is the number of points on the ground, and n is the number of image points.

With the given 3-photo strip shown in Figure B.1, there are $2n = 2(21) = 42$ equations. However there are $6m + 3g = 6(3) + 3(9) = 45$ unknowns. There is therefore the need for more equations in ordered for the system to be determinant. The next two sources of equations will provide enough information not only to solve the problem, but also to allow for the calculation of residuals.

Contribution from Position and Orientation Systems

The first source that will be used to add to the $\boldsymbol{B}$ matrix are constraints on the elements of orientation. These are usually obtained through the use of an inertial measurement unit (IMU) located in the aircraft. They can be defined as:

$$\begin{aligned} \omega_i &= \omega_i^0 + v_{\omega i} \\ \phi_i &= \phi_i^0 + v_{\phi i} \\ \kappa_i &= \kappa_i^0 + v_{\kappa i} \\ X_{Li} &= X_{Li}^0 + v_{XL} \\ Y_{Li} &= Y_{Li}^0 + v_{XL} \\ Z_{Li} &= Z_{Li}^0 + v_{XL} \end{aligned}$$

where $\omega_i, \phi_i, \kappa_i, X_{Li}, Y_{Li}, Z_{Li}$ are the unknown coordinates for image i, and $\omega_i^0, \phi_i^0, \kappa_i^0, X_{Li}^0$ Y_{Li}^0, Z_{Li}^0 are measured values (IMU). This equation therefore says that the true value of the orientation is the measured value plus some correction. While these equations are already linear, they will are not in the same form as the collinearity equations. If they are re-written using a taylor series expansion they will easily fit into the matrix system that is already in place.

$$\begin{aligned}
\omega_i^{00} + d_{\omega_i} &= \omega_i^0 + v_{\omega i} \\
\phi_i^{00} + d_{\phi_i} &= \phi_i^0 + v_{\phi i} \\
\kappa_i^{00} + d_{\kappa_i} &= \kappa_i^0 + v_{\kappa i} \\
X_{Li}^{00} + d_{X_{Li}} &= X_{Li}^0 + v_{XL} \\
Y_{Li}^{00} + d_{Y_{Li}} &= Y_{Li}^0 + v_{XL} \\
Z_{Li}^{00} + d_{Z_{Li}} &= Z_{Li}^0 + v_{XL}
\end{aligned}$$

Where now $\omega_i^{00}, \phi_i^{00}, \kappa_i, X_{Li}^{00}, Y_{Li}^{00}, Z_{Li}^{00}$ are the initial approximations for the ground points. These equations can be expressed as follows:

$$\dot{\boldsymbol{\delta}}_i = \dot{\boldsymbol{\epsilon}} + \dot{\boldsymbol{V}}$$

Where:

$$\dot{\boldsymbol{\delta}} = \begin{bmatrix} d\omega_i \\ d\phi_i \\ d\kappa_i \\ dX_{Li} \\ dY_{Li} \\ Z_{Li} \end{bmatrix} \quad \dot{\boldsymbol{\epsilon}} = \begin{bmatrix} \omega_i^0 - \omega_i^{00} \\ \phi_i^0 - \phi_i^{00} \\ \kappa_i^0 - \kappa_i^{00} \\ X_{Li}^0 - X_{Li}^{00} \\ Y_{Li}^0 - Y_{Li}^{00} \\ Z_{Li}^0 - Z_{Li}^{00} \end{bmatrix} \quad \dot{\boldsymbol{V}} = \begin{bmatrix} v_{\omega_i} \\ v_{\phi_i} \\ v_{\kappa_i} \\ v_{X_{Li}} \\ v_{Y_{Li}} \\ v_{Z_{Li}} \end{bmatrix}$$

Now its time to insert these equations into the B matrix. The numbers that will go into the matrix will be either a one or a zero. For this reason the matrix inserted will be termed the activation matrix, $\boldsymbol{A}$. This matrix will essentially pull off the correction in $\boldsymbol{\delta}$ that corresponds to a exterior orientation element. This matrix can also be configured to account for the off-diagonal, or covariance present in the weighting matrix which will be discussed in section B.1.4. The activation matrix for the first photo can be expressed as the following assuming that the covariance is to be ignored:

$$\dot{\boldsymbol{A}}_1 = \begin{bmatrix} -1 & 0 & 0 & 0 & 0 & 0 & 0 & 0 & 0 & ... & 0 & 0 & 0 \\ 0 & -1 & 0 & 0 & 0 & 0 & 0 & 0 & 0 & ... & 0 & 0 & 0 \\ 0 & 0 & -1 & 0 & 0 & 0 & 0 & 0 & 0 & ... & 0 & 0 & 0 \\ 0 & 0 & 0 & -1 & 0 & 0 & 0 & 0 & 0 & ... & 0 & 0 & 0 \\ 0 & 0 & 0 & 0 & -1 & 0 & 0 & 0 & 0 & ... & 0 & 0 & 0 \\ 0 & 0 & 0 & 0 & 0 & -1 & 0 & 0 & 0 & ... & 0 & 0 & 0 \end{bmatrix}_{6\times(6m+3g)}$$

The activation matrices can now be inserted into the $\boldsymbol{B}$ matrix as follows:

$$\boldsymbol{B} = \begin{bmatrix} \begin{bmatrix} \dot{\boldsymbol{B}}_1 & \dot{\boldsymbol{B}}_2 & ... & \dot{\boldsymbol{B}}_m & \ddot{\boldsymbol{B}}_1 & \ddot{\boldsymbol{B}}_2 & ... & \ddot{\boldsymbol{B}}_g \\ . & & . & & . & & . & \\ & . & & . & & . & & . \\ & & . & & . & & . & \\ & & & . & & . & & . \end{bmatrix}^{1}_{2n} \\ \begin{bmatrix} & & & \dot{\boldsymbol{A}}_1 & & & & \\ & & & \dot{\boldsymbol{A}}_2 & & & & \\ . & & . & & . & & . & \\ & . & & . & & . & & . \\ & & . & & . & & . & \\ & & & \dot{\boldsymbol{A}}_m & & & & \end{bmatrix}^{1}_{6m} \end{bmatrix}$$

Contribution from Ground Control

The final source of equations that will be inserted into the $\boldsymbol{B}$ matrix are constraints on ground control. These are usually obtained through the use of a surveyor. The treatment here is exactly the same as the constraints on orientation, but is included for completeness. They can be defined as:

$$\begin{aligned} X_j &= X_j^0 + v_{xj} \\ Y_j &= Y_j^0 + v_{yj} \\ Z_j &= Z_j^0 + v_{zj} \end{aligned}$$

where X_j, Y_j, Z_j are the unknown coordinates for point j, and X_j^0, Y_j^0, Z_j^0 are measured values (surveyor's values). While these equations are already linear, they can be re-written as before to match with form of the linearized collinearity equations.

$$\begin{aligned} X_j^{00} + dX_j &= X_j^0 + v_{xj} \\ Y_j^{00} + dY_j &= Y_j^0 + v_{yj} \\ Z_j^{00} + dZ_j &= Z_j^0 + v_{zj} \end{aligned}$$

Where now $X_j^{00}, Y_j^{00}, Z_j^{00}$ are the initial approximations for the ground points. These equations can be expressed as follows:

$$\ddot{\boldsymbol{\delta}}_j = \ddot{\boldsymbol{\epsilon}} + \ddot{\boldsymbol{V}}$$

Where:

$$\ddot{\boldsymbol{\delta}} = \begin{bmatrix} dX_j \\ dY_j \\ dZ_j \end{bmatrix} \quad \ddot{\boldsymbol{\epsilon}} = \begin{bmatrix} X_j^0 - X_j^{00} \\ Y_j^0 - Y_j^{00} \\ Z_j^0 - Z_j^{00} \end{bmatrix} \quad \ddot{\boldsymbol{V}} = \begin{bmatrix} v_{xj} \\ v_{yj} \\ v_{zj} \end{bmatrix}$$

Now its time to insert these equations into the B matrix. The numbers that will go into the matrix will be either a one or a zero. The activation matrix, again assuming that the covariance weighting terms will be ignored, for the first photo can be expressed as:

$$\ddot{\boldsymbol{A}}_1 = \begin{bmatrix} 0 & 0 & 0 & 0 & 0 & 0 & ... & -1 & 0 & 0 & ... & 0 & 0 & 0 \\ 0 & 0 & 0 & 0 & 0 & 0 & ... & 0 & -1 & 0 & ... & 0 & 0 & 0 \\ 0 & 0 & 0 & 0 & 0 & 0 & ... & 0 & 0 & -1 & ... & 0 & 0 & 0 \end{bmatrix}_{3\times(6m+3g)}$$

The activation matrices can now be inserted into the $\boldsymbol{B}$ matrix as follows:

$$\boldsymbol{B} = \begin{bmatrix} \begin{bmatrix} \dot{\boldsymbol{B}}_1 & \dot{\boldsymbol{B}}_2 & \dots & \dot{\boldsymbol{B}}_m & \ddot{\boldsymbol{B}}_1 & \ddot{\boldsymbol{B}}_2 & \dots & \ddot{\boldsymbol{B}}_g \end{bmatrix}^{1} \\ \begin{bmatrix} & & & \dot{\boldsymbol{A}}_1 & & & & \\ & & & \dot{\boldsymbol{A}}_2 & & & & \\ & & & & & & & \\ & & & & & & & \\ & & & & & & & \end{bmatrix}^{1} \\ \begin{bmatrix} & & & \ddot{\boldsymbol{A}}_1 & & & & \\ & & & \ddot{\boldsymbol{A}}_2 & & & & \\ & & & & & & & \\ & & & & & & & \\ & & & \ddot{\boldsymbol{A}}_c & & & & \end{bmatrix}^{1} \end{bmatrix}_{(2n+6m+3c)\times(6m+3g)}$$

where c is the number of ground control points.

Now that the observation matrix is formed, least squares can be used to find a solution to the $\boldsymbol{\delta}$ vector (equation B.1). The forms of the $\boldsymbol{\delta}$ and $\boldsymbol{\epsilon}$ matrices can now also be defined in full:

$$\boldsymbol{\delta} = \begin{bmatrix} \dot{\boldsymbol{\delta}}_1 \\ \\ \dot{\boldsymbol{\delta}}_m \\ \ddot{\boldsymbol{\delta}}_1 \\ \\ \ddot{\boldsymbol{\delta}}_g \end{bmatrix}_{(6m+3g)\times 1} \qquad \boldsymbol{\epsilon} = \begin{bmatrix} \boldsymbol{\epsilon}_1 \\ \\ \boldsymbol{\epsilon}_n \\ \dot{\boldsymbol{\epsilon}}_1 \\ \\ \dot{\boldsymbol{\epsilon}}_m \\ \ddot{\boldsymbol{\epsilon}}_1 \\ \\ \ddot{\boldsymbol{\epsilon}}_c \end{bmatrix}_{(2n+6m+3c)\times 1}$$

The solutions can be used to update the initial approximations, and the process is

repeated until the updates are below a pre-defined threshold. The following dimensional analysis is provided for further clarification:

$$\begin{aligned}\boldsymbol{\delta}_{(6m+3g)\times 1} &= (\boldsymbol{B}^T\boldsymbol{B})_{(6m+3g)\times(6m+3g)}\boldsymbol{B}^T_{(6m+3g)\times(2n+6m+3c)}\boldsymbol{\epsilon}_{(2n+6m+3c)\times 1}\\ &= [(6m+3g)\times(2n+6m+3c)]\times[(2n+6m+3c)\times 1]\\ &= (6m+3g)\times 1\end{aligned}$$

B.1.4 Accounting for Uncertainty

In ordered for this technique to work effectively, the uncertainty in each measurement must be factored in. For example, in the system of equations there are initial approximations made for the unknown parameters as well as measurements made through inertial measurement and GPS. There must therefore be a way to weight the initial approximations differently than the direct measurements. It is the opinion of the writer that applying the weight factors before formation of the $\boldsymbol{B}$ matrix is more intuitive than after. This can be done by first defining weight matrices in the same way as the dotted $\boldsymbol{B}$ matrices are formed.

$$\underset{\boldsymbol{Photo\ Coord.}}{\boldsymbol{W}} = \begin{bmatrix} \sigma_x^2 & \sigma_{x,y} \\ \sigma_{x,y} & \sigma_y^2 \end{bmatrix}^{-1} \qquad \underset{\boldsymbol{Ground\ Control}}{\ddot{\boldsymbol{W}}} = \begin{bmatrix} \sigma_{X_L}^2 & \sigma_{X_L,Y_L} & \sigma_{X_L,Z_L} \\ \sigma_{Y_L,X_L} & \sigma_{Y_L}^2 & \sigma_{Y_L,Z_L} \\ \sigma_{Z_L,X_L} & \sigma_{Z_L,Y_L} & \sigma_{Z_L}^2 \end{bmatrix}^{-1}$$

$$\underset{\boldsymbol{Exterior\ Orientation}}{\dot{\boldsymbol{W}}} = \begin{bmatrix} \sigma_\omega^2 & \sigma_{\omega,\phi} & \sigma_{\omega,\kappa} & \sigma_{\omega,X_L} & \sigma_{\omega,Y_L} & \sigma_{\omega,Z_L} \\ \sigma_{\phi,\omega} & \sigma_\phi^2 & \sigma_{\phi,\kappa} & \sigma_{\phi,X_L} & \sigma_{\phi,Y_L} & \sigma_{\phi,Z_L} \\ \sigma_{\kappa,\omega} & \sigma_{\kappa,\phi} & \sigma_\kappa^2 & \sigma_{\kappa,X_L} & \sigma_{\kappa,Y_L} & \sigma_{\kappa,Z_L} \\ \sigma_{X_L,\omega} & \sigma_{X_L,\phi} & \sigma_{X_L,\kappa} & \sigma_{X_L}^2 & \sigma_{X_L,Y_L} & \sigma_{X_L,Z_L} \\ \sigma_{Y_L,\omega} & \sigma_{Y_L,\phi} & \sigma_{Y_L,\kappa} & \sigma_{Y_L,X_L} & \sigma_{Y_L}^2 & \sigma_{Y_L,Z_L} \\ \sigma_{Z_L,\omega} & \sigma_{Z_L,\phi} & \sigma_{Z_L,\kappa} & \sigma_{Z_L,X_L} & \sigma_{Z_L,Y_L} & \sigma_{Z_L}^2 \end{bmatrix}^{-1}$$

In most cases, the measurements made are statistically independent and therefore uncorrelated. This means that the weight matrices reduce to the following:

$$\underset{\boldsymbol{Photo\ Coord.}}{\boldsymbol{W}} = \begin{bmatrix} \frac{1}{\sigma_x^2} & 0 \\ 0 & \frac{1}{\sigma_y^2} \end{bmatrix} \qquad \underset{\boldsymbol{Ground\ Control}}{\ddot{\boldsymbol{W}}} = \begin{bmatrix} \frac{1}{\sigma_{X_L}^2} & 0 & 0 \\ 0 & \frac{1}{\sigma_{Y_L}^2} & 0 \\ 0 & 0 & \frac{1}{\sigma_{Z_L}^2} \end{bmatrix}$$

$$\dot{\boldsymbol{W}} = \begin{matrix} \\ \\ \\ \\ \\ \\ \end{matrix} \overset{\boldsymbol{Exterior\ Orientation}}{\begin{bmatrix} \frac{1}{\sigma^2_\omega} & 0 & 0 & 0 & 0 & 0 \\ 0 & \frac{1}{\sigma^2_\phi} & 0 & 0 & 0 & 0 \\ 0 & 0 & \frac{1}{\sigma^2_\kappa} & 0 & 0 & 0 \\ 0 & 0 & 0 & \frac{1}{\sigma^2_{X_L}} & 0 & 0 \\ 0 & 0 & 0 & 0 & \frac{1}{\sigma^2_{Y_L}} & 0 \\ 0 & 0 & 0 & 0 & 0 & \frac{1}{\sigma^2_{Z_L}} \end{bmatrix}}$$

The weight matrices can now be applied to the dotted $\boldsymbol{B}$ matrices and the dotted $\boldsymbol{A}$ matrices as follows:

$$\hat{\dot{\boldsymbol{B}}}_{2\times 6} = \boldsymbol{W}_{2\times 2}\dot{\boldsymbol{B}}_{2\times 6} \quad \hat{\ddot{\boldsymbol{B}}}_{2\times 6} = \boldsymbol{W}_{2\times 2}\ddot{\boldsymbol{B}}_{2\times 6}$$
$$\hat{\dot{\boldsymbol{A}}}_{2\times 6} = \dot{\boldsymbol{W}}_{2\times 2}\dot{\boldsymbol{A}}_{2\times 6} \quad \hat{\ddot{\boldsymbol{A}}}_{2\times 6} = \ddot{\boldsymbol{W}}_{2\times 2}\ddot{\boldsymbol{A}}_{2\times 6}$$

The problem then proceeds as normal, with the new values substituted in. It is important to note that without this application of weights, the solution will not yield reasonable results since to much or too little emphasis will be placed on parts of the observation matrix. This can for example end up basing the solution on the observation equations and not at all on the ground control which would increase the error to unacceptable levels. The weights also control which parameter is a known or an unknown.

B.2 Application to Cloud Height Determination

The height of each cloud can then be found by performing a bundle adjustment in the opposite direction. In this case the whole sky camera takes the place of the airplane and the cloud field takes the place of the ground. A photo block is generated by taking several images as the cloud field moves over the camera. This assumes that there is not much vertical motion in the observed clouds over the time it takes for them to move over the camera. To obtain the equivalent of ground control points, the aircraft performing the over-flight can be used assuming it has accurate GPS. If the aircraft flies several parallel lines a good network of points can be obtained. This situation is illustrated in Figure B.3.

The value for 'B' or the airbase will also have to be estimated. This can be done by observing the distance in which the aircraft travels over a given time since its velocity

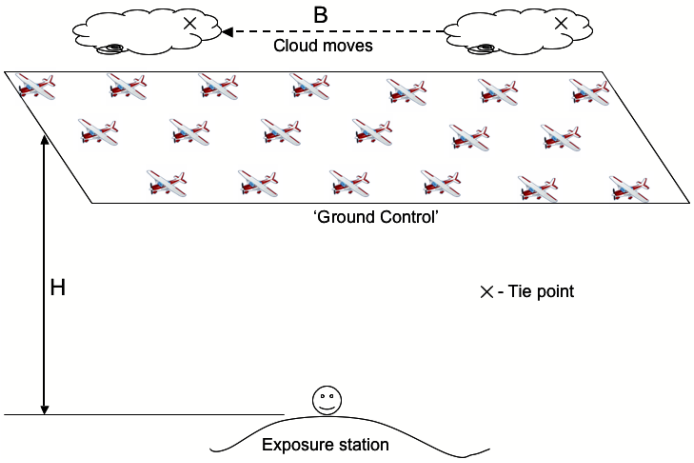

Figure B.3: The layout of a collection scenario where the aircraft is used to simulate ground control points.

is known. Once this is know, the block adjustment can be performed and the height of the cloud formations can be found.

An interesting trade-off to be considered in this case is the competing error processes between the size of the airbase and the error in the height. Equation B.5 shows the error that would be present in the height retrieval [Light, 1996].

$$\sigma_h = \frac{H}{f}\frac{H}{B}\sqrt{2}\sigma_x \tag{B.5}$$

where H is the vertical height from the camera to the plane, f is the focal length of the camera, B is the distance between the images, and σ_x is the measurement error in locating a pixel. This equation shows that the larger B becomes the lower the error. However, in order to obtain a larger distance, more time must elapse which will increase the error in the value of H since there is more chance that the object will drift up or down in the atmosphere. This means that an interesting study would be to explore the best way to obtain the optimal value of B for a given atmosphere which will produce the least error.

Appendix C

Shifting Cloud Locations

This research requires the azimuth and zenith of each cloud to be known. This information is usually only known for one location on the ground where a fisheye image is obtained of the sky. However, the observed azimuth and zenith for a cloud changes for different locations on the ground. This means that the inputs into the hemispherical model will change on a per-pixel basis. One way to determine how the heading to a cloud changes given the cloud height and change in ground position is discussed.

The geometry involved for two different ground positions and one cloud is shown in Figure C.1.

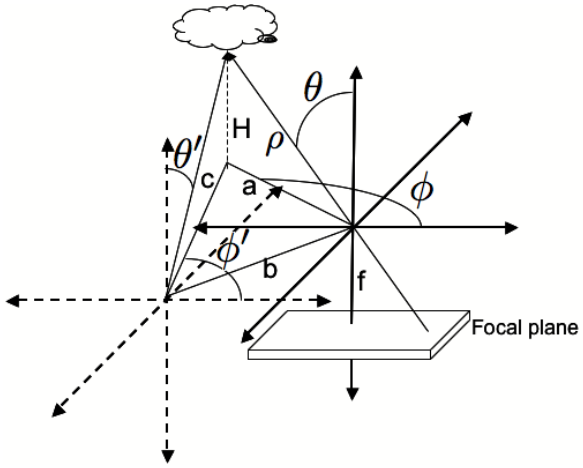

Figure C.1: Geometry defined for two ground locations and one cloud.

It is assumed in this case that the values for the azimuth and zenith (ϕ' and θ'), the height (H), and the distance between the two origins (c) are known. The azimuth and

zenith in the primed coordinate system are the variables which are to be solved.

First the azimuth can be found by examining the triangle formed in the x-y axis between the two locations. The new azimuth can be broken into two angles: σ_1 and σ_2. Figure C.2 shows how to solve for σ_1.

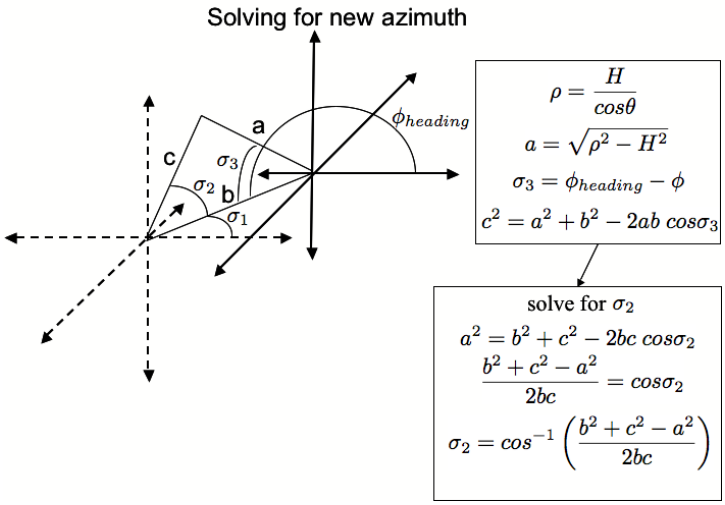

Figure C.2: Geometry and process used to solve for first half of new azimuth.

The final step is to solve for σ_2, shown in Figure C.3.

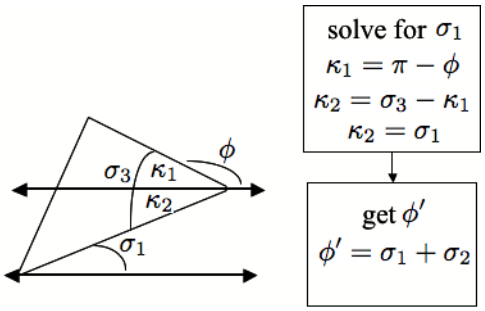

Figure C.3: Geometry and process used to solve for the final new azimuth.

Finally the new zenith can be easily be found by collapsing the triangular pyramid into a two dimensional triangle. Figure C.4 shows this process and the resultant zenith in terms of known values.

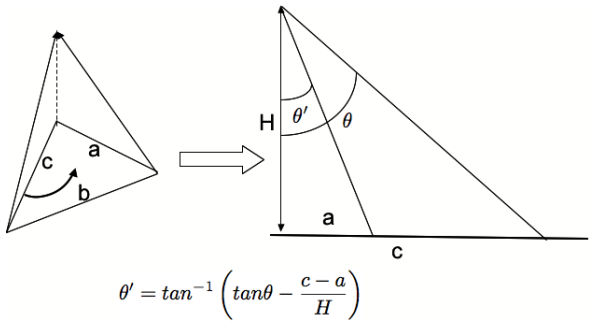

Figure C.4: Geometry and process used to solve for the final new zenith.

Appendix D

Spectral Calibration: WASP LT

D.1 Equipment Setup

This calibration uses a monochrometer, a collimator, and WASP LT. The purpose of this calibration is to determine the spectral response for each of the five multispectral camera's present. In this case table D.1 shows the filters present for each camera. However, the calibration procedure will work for any filter configuration.

Table D.1: Filter Setup

Camera	Filter
1	Dichroic Red
2	Dichroic Green
3	Dichroic Blue
4	695 Band Pass
5	715 Long Pass

Figure D.1 shows the position of each camera, assuming that you are looking at the front of the system.

The equipment set up is such that the monochrometer provides the input into the collimator. The collimator is used to provide input into each of the five cameras at once. In this way, the wavelength scan needs to be done only once. Figure D.2 shows a diagram of the setup.

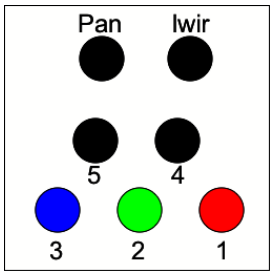

Figure D.1: Front view of WASP LT

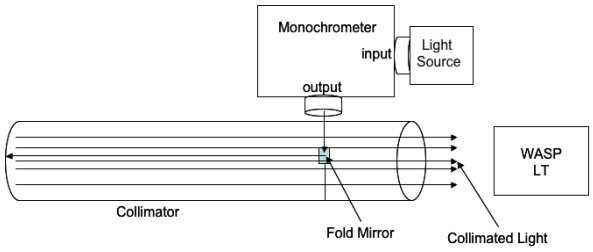

Figure D.2: Equipment setup used for calibration.

When aligning the front of wasp LT to point at the collimator, it is important to note that the fold mirror will cast a shadow. It is therefore important to make sure that no cameras are behind this shadow.

The following images show the setup in further detail.

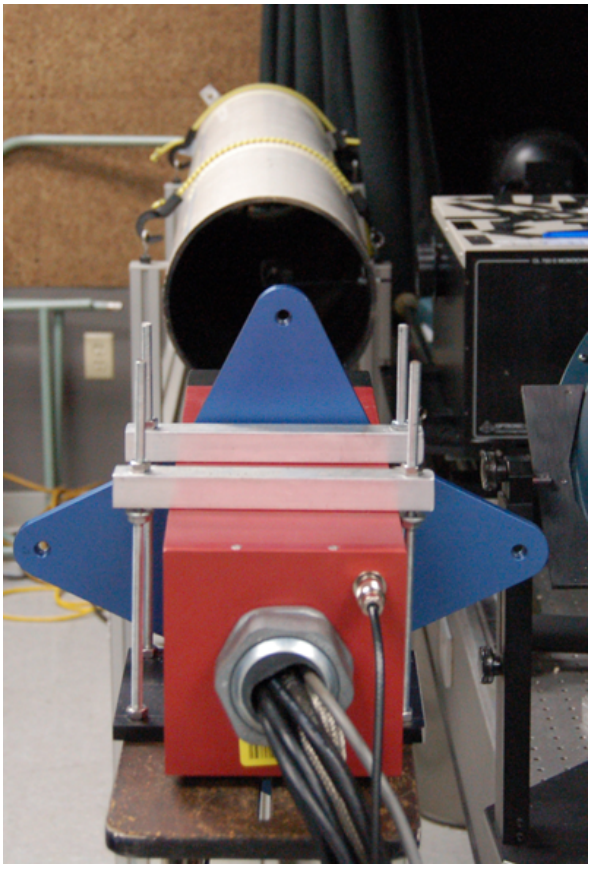

Figure D.3: View of back of WASP LT looking at the collimator.

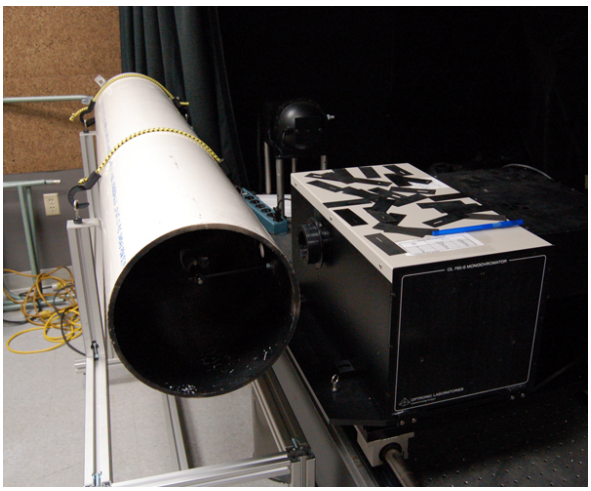

Figure D.4: View of monochrometer input into collimator.

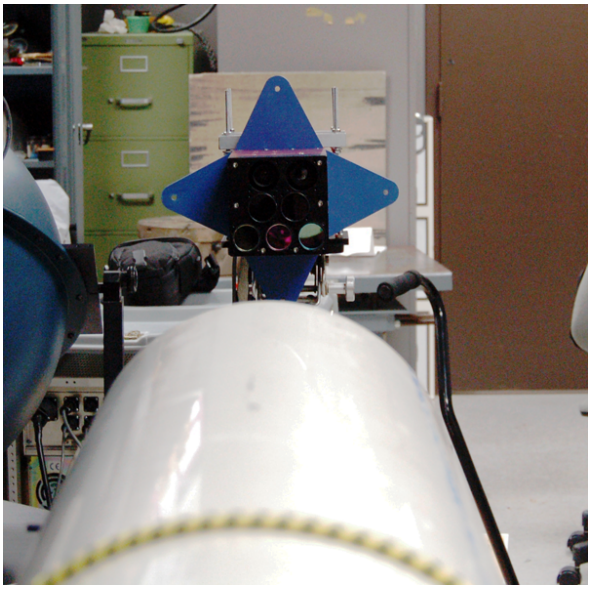

Figure D.5: Collimator output aligned with front of WASP LT.

D.2 Equipment Settings

The monochometer was set with the chopper wheel off. Filter two with a cut in wavelength of 345nm and filter three with a cut in wavelength of 602nm were used to block higher order light from the grating. Slits were inserted into the entrance and exit of the monochrometer to restrict the bandpass to 1nm (in this case with a slit width of 0.25 mm). Wasp LT was set such that no saturation occurred at wavelengths with peak energy and transmission. These locations were estimated by using the predicted response of the filter set. The fine and coarse gain was changed to a value of 80 for the filter set described above. The monochrometer was set to a wavelength, then 4 images were captured using the WASP LT software. This was repeated for each wavelength.

D.3 Results

The collimated light is focused onto each CCD array and imaged in theory as a point source. The measured radiation however has a point spread across several pixels. The maximum value was found for each camera and then averaged over the four images taken for each wavelength. The spectral curves were then peak normalized for each camera to produce the spectral response of the system. Figures D.6 - D.10 show the calculated spectral response.

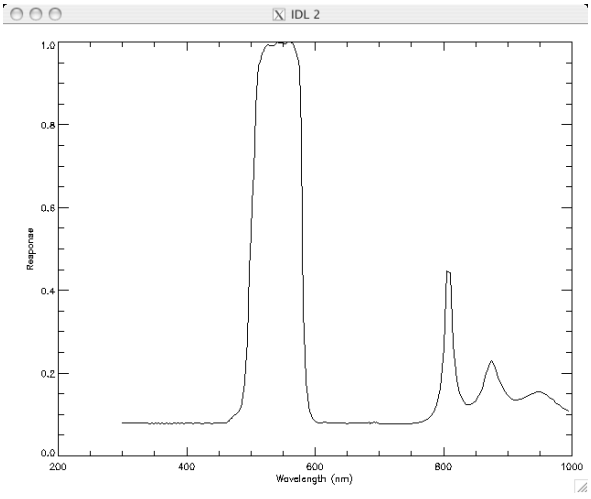

Figure D.6: Camera1 response.

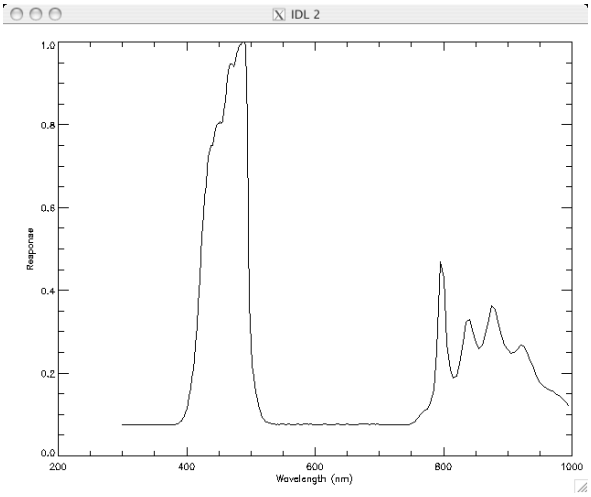

Figure D.7: Camera 2 response.

It should be noted that the dichroic filter set manufacture assumed that an IR blocking film would be applied to the system. This is not the case, which leads to the response seen in the IR for camera's one through three. In order to obtain a more typical system spectral response for use with this thesis, these artifacts were removed. Figure D.11 shows the spectral response of the system after processing.

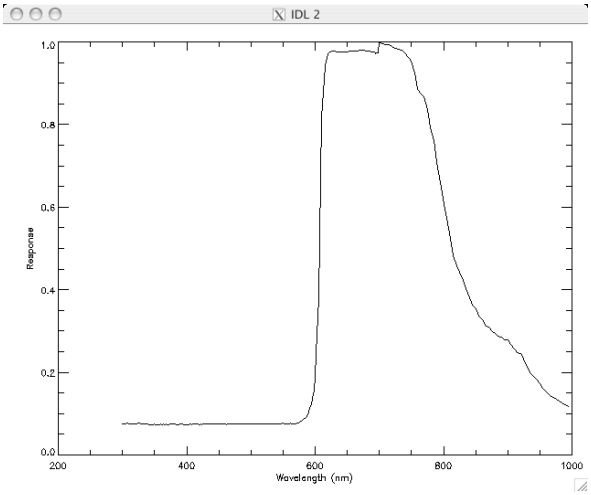

Figure D.8: Camera 3 response.

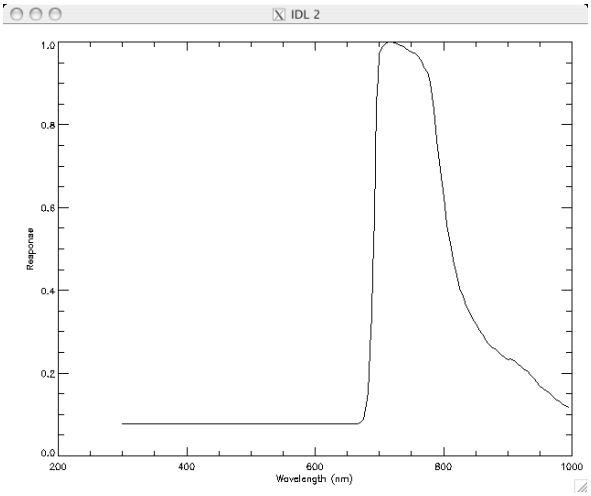

Figure D.9: Camera 4 response.

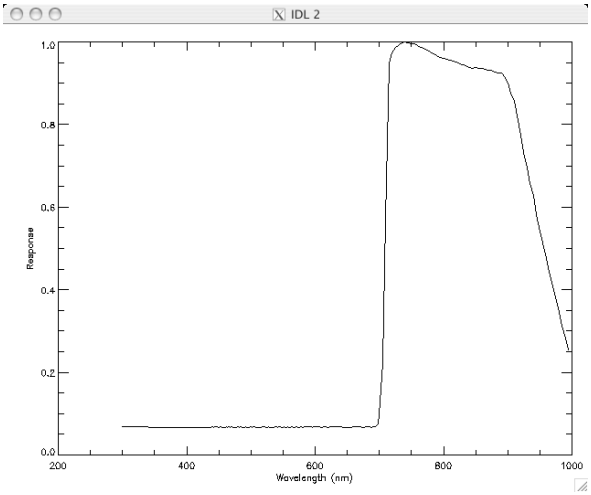

Figure D.10: Camera 5 response.

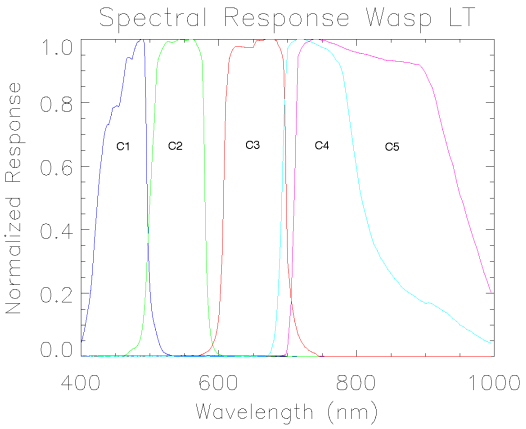

Figure D.11: System response after removing long wave response. Note that camera one and camera three were swapped in order.

Bibliography

K. Anderson, E. J. Milton, and E. M. Rollin. Sources of uncertainty in vicarious calibration. In *Geoscience and Remote Sensing Symposium*, volume IEEE, 2003. 1, 3.3.1

R. W. Basedow, D. C. Carmer, and M. E. Anderson. Hydice system: implementation and performance. In *Imaging Spectrometry*, volume 2480, pages 258–267, 1995. 4.1, 4.2

E. Ben-Dor, B. Kindel, and A. Goetz. Quality assessment of several methods to recover surface reflectance using synthetic imaging spectroscopy data. *Remote Sensing of Environment*, 90(3):389–404, 2004. 2.1.3

A. Berk, L. Bernstein, G. Anderson, P. Acharya, D. Robertson, J. Chetwynd, and S. Adler-Golden. Modtran cloud and multiple scattering upgrades with application to aviris. *Remote Sensing of Environment*, 65(3):367–375, 1998a. 2.1.2

A. Berk, L. S. Bernstein, G. P. Anderson, P. K. Acharya, D. C. Robertson, J. H. Chetwynd, and S. M. Adler-Golden. Modtran cloud and multiple scattering upgrades with application to aviris. *Remote Sensing of Environment*, 65(3):367–375, 1998b. (document), 2.7, 2.17

A. Berk, G. P. Anderson, P. K. Acharya, L. S. Bernstein, L. Muratov, J. Lee, M. J. Fox, S. M. Adler-Golden, J. H. Chetwynd, M. L. Hoke, R. B. Lockwood, T. W. Cooley, and J. A. Gardner. Modtran5 a reformulated atmospheric band model with auxiliary species and practical multiple scattering options. In *Proceedings of SPIE*, volume 5655, pages 88–95, 2005. 2.3

C. J. Bruegge, M. C. Helmlinger, J. E. Conel, B. J. Gaitley, and W. A. Abdou. Parabola iii: a sphere-scanning radiometer for field determination of surface anisotropic reflectance functions. *Remote Sensing Reviews*, 2000. (document), 3.35

R. N. Clark, G. A. Swayze, and K. E. Livo. Surface reflectance calibration of terrestrial imaging spectroscopy data. In *AVIRIS Workshop Proceedings*. USGS Spectroscopy Lab, 2002. URL `ftp://popo.jpl.nasa.gov/pub/docs/workshops/02_docs/2002_Clark_web.pdf`. 1, 2.1.3

K. A. Delin and S. P. Jackson. The sensor web: A new instrument concept. In *Symposium on Integrated Optics*, pages 20–26. SPIE, 2001. 2.3

O. Dubovik, A. Smirnov, B. N. Holben, M. D. King, Y. Kaufman, T. F. Eck, and I. Slutsker. Accuracy assessments of aerosol optical properties retrieved from aeronet sun and sky-radiance measurements. *JOURNAL OF GEOPHYSICAL RESEARCH*, 105(8):9791–9806, 2000. 2.2.3

M. J. Duggin and T. Cunia. Ground reflectance measurement techniques: a comparison. *Applied Optics*, 22(23):3771–3777, 1983. 2.2.2, 2.2.2

J. Dwyer, F. Kruse, and L. A.B. Effects of empirical versus model-based reflectance calibration on automated analysis of imaging spectrometer data. *Photogrammetric Engineering and Remote Sensing*, 61(10):1247–1254, 1995. 2.1.3

R. R. Fairbanks. *A Characterization of the Impact of Clouds on Remotely Sensed Water Quality.* PhD thesis, Rochester Institue of Technology, 1999. 3.3.1

B.-C. Gao, H. K.B., and A. Goetz. Derivation of scaled surface reflectances from aviris data. *Remote Sensing of Environment*, 44:165–178, 1993. 2.1.2

A. Goodenough. personal correspondence, 2007. 6.2

T. Herbert. Area projections of fish-eye photographic lenses. *Agricultural and forest meteorology.*, 39:215–223, 1987. 4.4.1

HydroRad Multi-Channel HyperSpectral Radiometer HydroRad Multi-Channel HyperSpectral Radiometer HydroRad Multi-Channel HyperSpectral Radiometer - Calibration Theory. HOBI Labs, 8987 E. Tanque Ver de 309-366, Tucson AZ 85749-9399, September 2002. 2.2.1

A. Imaging and G. L. version 3.12. Atmospheric correction now. Technical report, Boulder, CO, 2001. 2.1.2

E. Karpouzli and T. Malthus. The empirical line method for the atmospheric correction of ikonos imagery. *International Journal of Remote Sensing*, 24(5):1143–1150, 2003. 2.1.1

J. Kerekes. Error analysis of spectral reflectance derived from imaging spectrometer data. In *Geoscience and Remote Sensing Symposium Proceedings*, volume 5, pages 2697–2701. IEEE International, 1998. 2.1.3

F. Kruse. Comparison of atrem, acorn, and flaash atmospheric corrections using low-altitude aviris data of boulder, colorado. In *13th JPL Airborne Geoscience Workshop*, Pasadena, CA, 2004. Jet Propulsion Laboratory. 2.1.2

A. Lazarevich, M. Thomas, C. Philbrick, and R. Joseph. Survey of atmospheric remote sensing techniques leveraging information in passive ir spectral radiance measurements. In I. 04, editor, *Geoscience and Remote Sensing Symposium*, volume 7, pages 4769–4772, 2004. 2.2.3

D. L. Light. The national aerial photography program as a digital ortho image map base for geographic information systems. *Remote Sensing and GIS for Site Characterization: Applications and Standards*, pages 154–159, 1996. B.2

M. W. Matthew, S. M. Adler-Golden, A. Berk, G. Felde, G. Anderson, D. Gorodetzky, S.Paswaters, and M.Shippert. Atmospheric correction of spectral imagery: Evaluation of the flaash algorithm with aviris data. In *Proceedings of the 31st Applied Imagery Pattern Recognition Workshop*, pages 157–163, 2002. 2.1.2

S. S. McArdle, J. R. Miller, and J. R. Freemantle. Airborne image acquisition under cloud: preliminary comparisons with clear-sky scene radiance. In *Proceedings of the 15th Canadian Symposium on Remote Sensing*, 1992. 2.3

M. Moran, R. Bryant, K. Thome, W. Ni, Y. Nouvellon, J. Qi, T. Clarke, Y. Nouvellon, and M. Gonzalez-Dugo. A refined empirical line approach for reflectance factor retrieval from landsat-5 tm and landsat-7 etm. *Remote Sensing of Environment*, 78, 2001. 2.1.1

MTL. Atmospheric compensation investigation: Arm site. Technical report, Lockheed-Martin Missiles and Space Company, August 1997. (document), 4.1, 4.2.1

N. O'Neill, A. Royer, and M. Nguyen. Canadian advanced modified 5s. In CARTEL-1996-0202, editor, *Internal Report*. Centre d'applications et de recherches en te-le-de-tection, 1996. 2.1.2

A. Plana-Fattori, M. Legrand, D. Tanré, C. Devaux, A. Vermeulen, and P. Dubuisson. Estimating the atmospheric water vapor content from sun photometer measurements. *Journal of Applied Meteorology*, 37(8):790–804, 1998. 2.2.3

R. Price, C. D. Anger, and S. Mah. Preliminary evaluation of casi preprocessing techniques. In *Proceedings of the 17th Canadian Symposium on Remote Sensing*, pages 694–697. Canadian Remote Sensing Society and Canadian Aeronautics and Space Institute, 1995. 2.1.1

Z. Qu, B. C. Kindel, and A. F. H. Goetz. The high accuracy atmospheric correction for hyperspectral data (hatch) model. *IEEE TRANSACTIONS ON GEOSCIENCE AND REMOTE SENSING*, 41(6):1223–1231, 2003. 2.1.2, 2.2.3

L. C. Sanders. *An Atmospheric Correction Algorithm for Hyperspectral Imagery*. PhD thesis, Rochester Institue of Technology, 1999. 4.2.2

B. Schmid, C. Matzler, A. Heimo, and N. Kampfer. Retrieval of optical depth and particle size distribution of tropospheric and stratospheric aerosols by means of sun photometry. *IEEE TRANSACTIONS ON GEOSCIENCE AND REMOTE SENSING*, 35(1), 1997. 2.2.3

J. Schott. *Remote Sensing*. Oxford University Press, 1997. (document), 2.1, 2.1, 2.2, 2.3, 2.4, 2.1.1, 2.6, 4.4.1

J. Shanks and B. Shetler. Confronting clouds: detection, remediation and simulation approaches for hyperspectral remote sensing systems. In *29th Applied Imagery Pattern Recognition Workshop*, pages 25–31. IEEE, 2000. 3.3.1

G. M. SMITH and E. J. MILTON. The use of the empirical line method to calibrate remotely sensed data to reflectance. *International Journal of Remote Sensing*, 20 (13):2653–2662, 1999. 2.1.1

L. Smith. *Visible, Near Infrared, and Short Wave Infrared Spectra Collection Protocol*. Digital Imaging and Remote Sensing Laboratory, Chester F. Carlson Center for Imaging Science, Rochester Institute of Technology, 54 Lomb Memorial Drive, Rochester NY 14623-5604, 12-2-2002 edition, 2004. 2.2.2

K. Staenz, J. Secker, B. Gao, C. DAvis, and C. Nadeau. Radiative transfer codes applied to hyperspectral data for the retrieval of surface reflectance. *ISPRS Journal of Photogrammetry and Remote Sensing*, 57(3):194–203, 2002. 2.1.2

P. M. Teillet, R. P. Gauthiera, G. Fedosejevsa, M. Maloleya, A. Chichagova, and G. Ainsleya. A soil moisture monitoring sensorweb demonstration in the context of integrated earth sensing. In W. L. Barnes, editor, *Earth Observing Systems VIII*, volume 5151. SPIE, 2003. 2.3

E. F. Vermote. Second simulation of the satellite signal in the solar spectrum. *Geoscience and Remote Sensing, IEEE*, 35:675–686, 1997. 2.1.2

P. R. Wolf and B. A. Dewitt. *Elements of Photogrammetry*. McGraw Hill, 3rd edition, 2000. A, B.1.1